

ABSTRACT

CHANDRA, SOUVIK. Modeling, Analysis and Control of Oscillations in Wind-integrated Power Systems. (Under the direction of Aranya Chakraborty.)

In this dissertation work, we assess the impacts of high wind penetration on the operational aspects of conventional power system and propose methods for planning and control to ensure a secure operation. Analytical models of the wind-integrated power system are derived where wind turbine is connected to the power grid asynchronously via doubly fed induction generators (DFIG). Particularly we focus on the equilibrium and the electromechanical oscillation spectrum of the power system. Our study illustrates that the wind power locations affect the oscillation spectrum particularly the inter-area or slow oscillation of the power system. We design damping controllers on the wind generator and associated storage to minimize the undesired influence of wind on the oscillations enabling an efficient operation of the power system. Further analysis shows that the wind power alters the equilibrium characteristics in a power system and give rise to slow and poorly damped inter-area oscillatory modes under certain scenarios, by significantly affecting the bus voltages of the power system. We also propose a numerical homotopy based method which is capable of identifying multiple equilibrium and the power flow solution boundary of the wind-integrated power system.

First, in Chapter 2, we analytically show the impact of wind power injection on the spectral response of a large radial power system, represented as a continuum model. The inter-area oscillation spectrum of the power system is found to be significantly affected by the location of the wind injection in the power system. Accordingly in Chapter 3, we design a linear controller for the wind generator to shape inter-area oscillation spectrum in a desired pattern. Particularly it is shown that the performance of the wind farm controller in shaping the inter-area oscillation spectrum can be considerably improved by a coordinated control action with a battery energy system (BES).

Next in Chapter 4, a lumped component model of a wind-integrated power system is

derived consisting of synchronous generators, wind turbines interfaced with a DFIG, loads and transmission lines. Considering a power system with multiple coherent areas of operation, we analytically show how the slow or inter-area oscillatory modes get affected by increasing wind penetration. Simulation studies suggest that depending on the relative locations of the synchronous generators, the wind generator and the loads, there might be scenarios in which the inter-area oscillatory mode gets slower with higher wind injection ultimately leading to instability.

In Chapter 5, we apply a homotopy based numerical continuation algorithm to compute multiple real equilibrium and equilibrium boundaries in a wind-integrated power system to ensure its stable operation. In multiple wind injection scenario these boundaries become heavily dependent on the relative wind penetration levels. Traditional continuity based iterative methods are unsuitable to find multiple solutions and hence fail to identify these boundaries without a prior knowledge of the system and a good initial guess. However the proposed method is independent of initial guess and guarantees to find the solution boundary.

© Copyright 2015 by Souvik Chandra

All Rights Reserved

Modeling, Analysis and Control of Oscillations in Wind-integrated
Power Systems

by
Souvik Chandra

A dissertation submitted to the Graduate Faculty of
North Carolina State University
in partial fulfillment of the
requirements for the Degree of
Doctor of Philosophy

Electrical and Computer Engineering

Raleigh, North Carolina

2015

APPROVED BY:

Iqbal Husain

Mo-Yuen Chow

Fen Wu

Aranya Chakrabortty
Chair of Advisory Committee

DEDICATION

To my parents.

BIOGRAPHY

Souvik Chandra was born on 24th of May, 1987 in Kolkata, West Bengal, India. He did his schooling first with Nava Nalanda High School and later on with Jodhpur Park Boys School. He was honored with National Merit Scholarship for his high school results in May 2005 by the Government of India. He went to Jadavpur University, Kolkata to pursue Bachelors of Electrical Engineering degree which he successfully completed with Honors in 2009. He received Masters in Control Systems Engineering from Indian Institute of Technology(IIT) Kharagpur in 2011. Thereafter, he joined the Department of Electrical and Computer Engineering at North Carolina State University s in a Ph.D. program to work on Power and Control. Souvik will be joining Schwietzer Engineering Lab, Pullman, WA in a full-time position as a Power Engineer from October, 2015.

ACKNOWLEDGEMENTS

I would like to thank my advisor, Dr Aranya Chakraborty , for his extensive help throughout the duration of my PhD research career here at NC State. Without his help, technical advice, and mentoring, this wouldn't have been possible. The experience of working with him has been great, particularly the one-to-one conversations that we have had over the past few years were very productive. I would like to thank him for the immense faith that he has shown in my abilities and for grooming me for my future technical endeavors.

I would also like to thank all the other members in my thesis committee, namely, Professors Iqbal Husain, Mo-Yuen Chow and Fen Wu, for carefully reviewing my work and providing me with valuable feedback to improve my work. I am indebted to my collaborators Dr Dennice Gayme from Johns Hopkins University and Dr Dhagash Mehta from University of Notre Dame who have always been very generous to review my work and helping me with ideas. Also I would like to extend my sincere thanks to all the other Professors in the the FREEDM Systems Center for giving me an exposure to state-of-art research topics and training environment. Not only the Professors, I should thank all the staff as well, especially Mrs Keren Autry, for their immense help in administrative matters and making my life easy.

I would like to express my sincere gratitude to all my teachers who have influenced me tremendously to take up research as my career path. I still remember the roles of a few right from my school days like Mrs Sharmistha Chowdhury, Mr Shubhash Pramanik, Mr Kaushik Roy, Mr Ajay Dhar and Mr Shibaji Chakraborty who have inspired me to think independently and have that constant thirst to learn something new. In my undergraduate days in Jadavpur University, I was deeply motivated by attending the classes of many professors particularly Dr Amitava Chatterjee, Prof. Tapan Kumar Ghosal and Prof. Sivaji Chakravorti. Particularly I am indebted to Prof. Ghosal as he inspired me to go for higher education and eventually to research. I am obligated to mention here the roles of Prof. Siddhartha Mukhopadhyay and Prof. Prasanta Kumar Das as well from IIT Kharagpur who were my masters thesis advisors

and deeply encouraged my academic endeavors. On a whole I was blessed with great teachers throughout my academic career who helped me to keep ablaze my constant zeal to learn and reinvent myself.

My graduate life at Raleigh would have been much dull if I had not met all those wonderful friends both in my neighborhood and in the FREEDM lab. I shared my stay here with my roommate Prithwish Bhaumik who has been a great companion and supported me in my every endeavor. I enjoyed the company of many of my neighbors in our Raleigh Community like Ayan Dasgupta, Sayantan Banerjee, Rudrodip Majumdar, Rajarshi Dasbhowmik, Priyam Das, Raj Bhakta, Shuva Gupta, Lopamudra Kundu and many others. I appreciated the company of my lab mates as well during my duration at the FREEDM systems center with whom I had constant interactions on technical issues and shared a strong bonding of friendship. I would like to mention Sayan Acharya, Ritwik Chattopadhyay, Samir Hazra, Ankan De, Sachin Madhoosodan, Awneesh Tripathi, Ali Safayet, Govind Chavan, Byron Beddingfield, Behzad Nabavi, Thomas Nudell, Almuatazbellah Boker, Urvir Singh, Sumit Dutta, Tanvir Khan, Nan Xue, Abhishek Jain, Matthew Weiss, Jianhua Zhang, Faeza Hafiz and many others.

I would like to thank my family and relatives who have always supported me and encouraged me through out my life. I am blessed to have my awesome parents Mr Susanta Chandra and Mrs Swapna Chandra whose immense efforts have enabled me to stand where I am today. I am highly indebted to them for the culture and the environment in which they have brought me up for which I could become a balanced individual in my life. Lastly, I would like to express my thanks to the person who has given me company and encouraged me in my work the most in the last four years. She is my girlfriend Sangeeta Nundy, also a PhD scholar herself. Without her companionship, love and care it would have been difficult for me to have such a great life. I hereby dedicate this work to Sangeeta and my parents.

TABLE OF CONTENTS

| | |
|---|-------------|
| List of Tables | viii |
| List of Figures | ix |
| Chapter 1 Introduction | 1 |
| 1.1 Background | 1 |
| 1.1.1 Types of Wind Integration Technologies | 2 |
| 1.1.2 Small Disturbance Rotor Angle Stability Dynamics | 4 |
| 1.1.3 Transient Voltage Stability | 6 |
| 1.2 Contributions | 7 |
| 1.3 Organization | 7 |
| Chapter 2 Spectral Response of a Wind-injected Power System Model | 9 |
| 2.1 Continuum Representation of a Radial Power System with a Point Wind Injection | 10 |
| 2.2 Wind Farm Model | 13 |
| 2.3 Computation of the Spectral Response of the Wind-injected Power System | 14 |
| 2.4 Simulation Results | 15 |
| 2.4.1 Spectral Response of the Wind Farm | 16 |
| 2.4.2 Spectral response of the Power Flow in the Grid | 16 |
| 2.5 Conclusions | 17 |
| Chapter 3 Damping of Inter-area Oscillations in Power Systems: A Frequency Domain Approach | 19 |
| 3.1 Centralized Control Design for Spectral Matching | 20 |
| 3.1.1 Wind Farm Model and Controller Design | 20 |
| 3.1.2 BES Model and Controller Design | 24 |
| 3.1.3 Spectral Analysis | 27 |
| 3.1.4 Simulation Results | 30 |
| 3.2 Disaggregation of Control from Equivalent Turbine to Multiple Turbines | 31 |
| 3.2.1 Centralized Design | 32 |
| 3.2.2 Decentralized Design | 33 |
| 3.2.3 Simulation Results | 34 |
| 3.3 Conclusions | 37 |
| Chapter 4 Time Scale Modeling of Power Systems with Wind Injections | 38 |
| 4.1 Wind Integration Modeling | 40 |
| 4.1.1 Synchronous Generator Model | 40 |
| 4.1.2 Wind Power Plant Model | 42 |
| 4.1.3 Wind Integrated Power System Model | 46 |
| 4.2 Time-scale Modeling | 48 |
| 4.2.1 Power System Time-constants | 49 |
| 4.2.2 Time-scale Separation | 51 |

| | | |
|---|--|-----------|
| 4.2.3 | The Effect of Wind Injection on Time-scales | 53 |
| 4.3 | Results | 55 |
| 4.3.1 | 2-area 8-bus Power System | 56 |
| 4.3.2 | 5-area 68-bus Power System | 58 |
| 4.4 | Conclusions | 61 |
| Chapter 5 Equilibria Analysis in Wind-integrated Power Systems | | 63 |
| 5.1 | Dynamic Model of Power System | 64 |
| 5.1.1 | Synchronous Generator Model | 64 |
| 5.1.2 | WPP Model | 66 |
| 5.1.3 | Dynamic Load Model | 70 |
| 5.1.4 | Power Flow Model | 70 |
| 5.2 | Equilibrium Analysis | 71 |
| 5.3 | Parameter Homotopy Continuation Algorithm | 73 |
| 5.4 | Results | 76 |
| 5.4.1 | Discussion: On the Network Topology and Upper Bound on the Number of Equilibria | 78 |
| 5.5 | Background for Power Flow Solution Boundary | 79 |
| 5.6 | Examples | 82 |
| 5.6.1 | 3-bus System | 82 |
| 5.6.2 | 10-bus system | 85 |
| 5.7 | Conclusions | 86 |
| Chapter 6 Conclusions and Future Works | | 88 |
| References | | 91 |
| Appendix | | 98 |
| Appendix A | Simulation Parameters | 99 |
| A.1 | Model Parameters for Two-area Kundur System | 99 |
| A.2 | Wind Plant Parameters | 99 |
| A.3 | Model Parameters for 10-bus 2-wind Generator Power System | 100 |

LIST OF TABLES

| | | |
|-----------|--|----|
| Table 2.1 | List of principle symbols in Continuum model of the Power System | 11 |
| Table 3.1 | List of principle symbols in BES model | 26 |
| Table 3.2 | Optimal controller parameters sets | 30 |
| Table 3.3 | Optimal controller parameters sets | 36 |
| Table 4.1 | Matrix norms and slow eigenvalues for the 8-bus 4-machine 2-area power system. | 57 |
| Table 4.2 | Fast eigenvalues for the 8-bus 4-machine 2-area power system in different scenarios. | 58 |
| Table 4.3 | Matrix norms and slow eigenvalues for the 68-bus 16-machine 5-area power system. | 59 |
| Table 5.1 | Types of feasible equilibrium for various wind speeds (v_r^e) and wind bus voltage levels $ V_{w6}^e $ | 76 |
| Table 5.2 | Dominant pair of Eigen values for different stable equilibria | 77 |

LIST OF FIGURES

| | | |
|------------|---|----|
| Figure 2.1 | A radial power system of generators subject to wind injection at a distance α along the transfer path. | 12 |
| Figure 2.2 | Frequency and time domain response of the power output from the linearized wind farm model in (2.23) | 17 |
| Figure 2.3 | Spectral response of power flow of a wind-integrated power system for different wind farm power injection locations α | 18 |
| Figure 3.1 | Steady-state speed versus power characteristics of a 1 MW wind turbine. The maximum power curve, shown in red, depicts the operating points for each wind speed. | 21 |
| Figure 3.2 | Two-loop control scheme for wind turbine in which the inner loop controls generator speed set points shown in Figure 3.1 while the outer loop is the proposed power controller for shaping the inter-area oscillation spectrum of the grid. | 22 |
| Figure 3.3 | Battery Energy System (BES). | 23 |
| Figure 3.4 | Spectral response comparison | 31 |
| Figure 3.5 | Schematic for the disaggregated wind farm control, where each turbine is controlled individually, and the total power output of the farm is aggregated and injected to the grid at the point of common coupling. | 32 |
| Figure 3.6 | Comparison of spectral matching between the aggregate versus disaggregated wind farm model | 34 |
| Figure 3.7 | Arrangement of turbines in the wind farm. | 36 |
| Figure 3.8 | Open-loop versus closed-loop $\delta(t)$ at $u = 0.25$ with slow mode components | 37 |
| Figure 4.1 | Wind turbine interfaced to the grid via a DFIG | 41 |
| Figure 4.2 | Decoupled active and reactive power control of a DFIG integrating a wind generator via the rotor-side controller | 43 |
| Figure 4.3 | Kundur 8-bus, 4-machine, 2-area power system with wind injection at bus 5 | 55 |
| Figure 4.4 | Kundur 8-bus, 4-machine, 2-area power system with wind injection at bus 7 | 56 |
| Figure 4.5 | 68-bus, 16-machine, 5-area power system: Scenarios with wind injection at bus 66 and at bus 38 | 62 |
| Figure 5.1 | Dynamic model of a Wind integrated power system | 65 |
| Figure 5.2 | Schematic representation of the WPP and the power system | 66 |
| Figure 5.3 | 3-bus power system with two parameters | 81 |
| Figure 5.4 | Power flow solution boundary tracking with various initial points | 83 |
| Figure 5.5 | 10-bus power system with 2 WPP | 84 |
| Figure 5.6 | Number of real solutions of the power flow in the 10-bus power system | 86 |

Chapter 1

Introduction

1.1 Background

Research on wind power integration has witnessed a tremendous boost over the past few decades due to a rapid increase in worldwide installations of wind farms. As reported by the World Wind Energy Association, the globally installed capacity of wind power has grown annually at an average rate of 20% over the last four years (2011-2015) [1]. Thus wind has emerged as a leading source of renewable energy with nearly 428 GW of installed capacity as of June 2015 [1]. The United States has also seen a huge growth in the total installed capacity of wind power, which is currently equal about 67,870 MW [1, 79]. This expansion is being expedited by government mandates and renewable energy goals, such as US Department of Energy's goal of 20% wind by 2030 [10, 75]. Wind power which is often identified worldwide as an inexpensive yet environmentally safe source of energy is only going to grow at a better pace in the next decade. Due to evolution of technology, the size of the individual wind turbines has also grown to above 5-MW capacity, while in the past wind turbines were only rated in tens of kilowatts [89]. As the wind integration technology matures and wind power penetration levels increase, interconnecting a large-scale wind power plant into the conventional power system will have a major impact on the stability and reliability of the power system which needs to be studied in details.

This has led to an enormous amount of research on various topics related to power system planning and operations with high wind penetration, which includes reliability analysis [75], security [78], wind-centric electricity markets [69], and demand response [9]. A significant amount of work has also been carried out on component-level modeling and control of wind turbines with relevant power electronic interfaces [21, 79, 98]. A few works have focused on operational concerns of the power system as well, such as frequency regulation and load following [19, 38] or mitigating the risks associated with variability and uncertainty in wind power production using operating reserves [51], storage [8] or demand-side management [90]. However, only a modest amount of research has been directed towards gaining a theoretical understanding of how wind power generation affects the dynamic behavior of power systems that are dispersed over large geographical areas. The majority of the work on this topic has focused on component-level analysis of the impacts of integrating doubly-fed induction generators (DFIG) in the grid [83, 91] using simulation-based case studies [25, 70, 95] that doesn't provide much theoretical insights. Also a general framework for analysis and control of system-level dynamic power system model in presence of substantial wind penetration is missing. Thus the primary focus of this dissertation work is to derive theoretical models for wind-integrated power system in order to investigate the impact of penetration levels on the dynamic power system model, particularly on equilibrium and small disturbance rotor-angle oscillation dynamics. As a background review, we discuss the various wind integration technologies, the concepts of small disturbance rotor angle dynamics, equilibria analysis and transient voltage stability of power system.

1.1.1 Types of Wind Integration Technologies

Wind power is currently integrated with the existing power systems by different types of technologies which are reviewed in this subsection [89]. Typically a wind power plant consists of a large number of wind turbines connected to a point of common electrical coupling in the grid also known as the wind bus. Individual technologies of the turbines determine the cost, intricacy, size and efficiency of the extracted power. Mechanical parts of a wind turbine

uses a blade and hub rotor assembly to obtain wind power and transfer it to a generator at a higher speed through a geared shaft. Since the wind speed varies, the generator speed also needs to vary for which the most popular form of wind integration is through asynchronously means via induction generators. Primarily the classification of the wind turbines is based on the speed of the generator, fixed speed (type-I) or variable speed type (type II-IV) and the related technologies [79, 89]. The details of these technologies for the wind turbines are given as below

Type I These wind turbines are of fixed-speed type and are used primarily in small utility-scale applications. They have a fixed turbine rotor speed even even the wind speed varies. They are thus interfaced with squirrel-cage induction machines, with the stator directly connected to the grid and the rotor short-circuited. Even though the technology is fairly robust, cheap and simple, lack of efficiency and inability to compensate reactive power to the grid are some of its major disadvantages.

Type II These wind turbines are of variable-speed type which can operate at a given range of rotor speeds as the wind speed changes to ensure efficiency. These turbines often are provided with blade and pitch control which improves efficiency as compared to fixed speed types. Here the variable speed of the machine is maintained via the dynamic rotor resistance control where the resistance in the rotor circuit of the machine is allowed to change for a certain range of operating slip speeds.

Type III This type of wind turbines are most widely used for large wind installations where a Doubly-fed induction generator (DFIG) is used to interface the turbine with the grid. In a DFIG the stator is directly connected to the grid while a back-to-back AC/DC/AC converter drives the rotor circuit. One can easily control the rotor currents here for a decoupled active and reactive power output which ensures maximum power point tracking and reactive power compensation. Also since the converter is only controlling the power in the rotor circuit, it can be rated in slip power which is usually a small fraction of the generator's total power output. However the rating of the converter can constrain the

reactive power capability of the generator. In our work we focus on this type of wind generators and will derive the detailed dynamic model of this type of wind generators in 3.

Type IV These wind turbines use full converters where the wind turbine is connected only via the back-to-back AC/DC/AC converter to the grid. These turbines may employ synchronous generators, induction generators or permanent magnet machines which offer full independent real and reactive power control.

Next we review the rotor angle dynamics of conventional power systems.

1.1.2 Small Disturbance Rotor Angle Stability Dynamics

Rotor angle stability is a type of power system stability which ensures that the synchronous generators of an interconnected power system remain in synchronism when subjected to a disturbance [44]. The equilibrium between electromagnetic torque and mechanical torque of the synchronous machines restore this type of stability of the system. If the system is disturbed from the equilibrium by a perturbation it results in acceleration or deceleration of the rotors of the machines with respect to each other. A small-disturbance (or small-signal) rotor angle stability is concerned with the insufficient damping of these electromagnetic oscillations of the power system under small disturbances. Such oscillations can be local between generators operating in geographically close generation area known as local or intra-area oscillations. Or else these oscillations can be global between groups of machines in different generation areas also known as inter-area oscillations. The inter-area oscillations in a power system follow from the inherent clustering or grouping patterns in the distribution of generators, transmission lines, and loads. Qualitatively speaking, generators in a given area are strongly connected to each other via a dense network of short tie-lines with small reactances, and thereby form a coherent oscillation group, while these groups themselves are connected to each other via a sparse network of long tie-lines with large reactances. The work in [18] shows that such difference in the magnitudes of intra-area versus inter-area reactances can lead to a two-time-scale behavior

in the dynamic response of the phase angles and frequencies. The fast time-scale arises from the relative motions of the local generators inside an area, which synchronize quickly due to their strong interconnections reaching a so called quasi-steady state. The states from the different areas, thereafter, synchronize with each other over a slower time-scale, giving rise to inter-area oscillations. A constructive analysis of this behavior is also common in the literature. For example, to obtain an analytical expression for the fast and slow oscillation dynamics, one may define the slow or aggregate variable for the k^{th} area to be the so-called center of inertia angle for that area, namely

$$y_k \triangleq \frac{\sum_{i=1}^{n_k} M_i^k \delta_i^k}{\sum_{i=1}^{n_k} M_i^k}, \quad k = 1, 2, \dots, r \quad (1.1)$$

where δ_i^k and M_i^k are, respectively, the i^{th} machine angle and inertia in the k^{th} area, n_k is the total number of machines in the k^{th} area, and r is the total number of areas. Similarly, the fast variable for the k^{th} area can be defined as

$$z_{k,i} \triangleq \delta_i^k - \delta_1^k, \quad i = 1, 2, \dots, n_k, \quad k = 1, 2, \dots, r. \quad (1.2)$$

The time-scale separation between the fast and slow oscillations can then be expressed explicitly in the singular perturbed form

$$\frac{dy}{dt_s} = A_{11}y + A_{12}z, \quad \epsilon \frac{dz}{dt_s} = A_{21}y + A_{22}z \quad (1.3)$$

where $\epsilon \ll 1$ is a small parameter, and the exact expressions for the four state matrices can be found in [18]. Assuming $\epsilon \approx 0$, the effective swing dynamics for the inter-area oscillations can then be written as:

$$\frac{dy}{dt_s} = (A_{11} - A_{12} A_{22}^{-1} A_{21})y. \quad (1.4)$$

It must be noted that the matrix $(A_{11} - A_{12} A_{22}^{-1} A_{21})$ is not necessarily block-diagonal, and hence the inter-area oscillation modes are not necessarily decoupled. The impact of increased

levels of wind penetration on these oscillations have also been the subject of a number of recent studies [26, 91, 95] which shows some results based on simulation case studies. But in this work we look to theoretically capture the effect of wind penetration on the oscillatory modes from the analytical model of the wind-integrated power system. We also validate the findings from the theoretical model with relevant case studies using standard IEEE models.

1.1.3 Transient Voltage Stability

Voltage stability is related to the ability of the power system to maintain voltages at all of its buses to some steady value following a disturbance at a given initial condition [44]. Small-signal or transient voltage stability is related to maintenance of steady voltages under small disturbance [24, 44]. Wind penetration has a significant impact on the equilibrium characteristics of a power system which is closely related to small-signal transient voltage stability. It has been well established in literature that wind generators interfaced with doubly-fed induction generators can be particularly beneficial during short term voltage instability owing to their reactive power capability as compared to older fixed speed induction generators [81, 97]. However how the amount of penetration and location of the wind injection affects the equilibrium characteristics is missing in literature. We tried to address this issue by showing how in a multiple wind-injection scenario the power system equilibrium is parameterized by the wind variables. Thereafter we use a parameter homotopy based computational method to identify all the equilibria of the power system. Next we use the same procedure to identify the relative penetration levels in a multiple-wind scenario where the power flow solution boundary occurs, the knowledge of which is crucial to maintain voltage security from a planning perspective. The traditional methods for solving these problems [35] depends upon initial guess and local approximations. However the proposed method is independent of initial guess and guarantees to find all solution boundaries in a given parameter space.

The various contributions of the work and the organization of the dissertation are shown as below.

1.2 Contributions

1. Coordinated controller design for wind farms and battery energy systems for inter-area oscillation damping in power systems via spectral matching.
2. Derivation of the wind-integrated power system model where wind turbines are interfaced to the grid via a DFIG.
3. Time-scale modeling of wind-integrated power systems and analysis of the effect of increasing wind penetration on the inter-area modes.
4. Equilibria analysis of wind-integrated power systems via numerical homotopy method and determination power flow boundary or transient voltage stability limit.

1.3 Organization

In Chapter 2, of this thesis, we derive an approximate continuum model of a large radial power system network with wind injection at a point location. We show analytically that the spectral response of this system is a function of the location of the wind injection. Particularly our simulation results based on a two-area power system model inspired by the Pacific AC Inter-tie demonstrate that the inter-area oscillation spectrum of the power system is highly dependent on the location of wind injection.

In Chapter 3, we design controls on the wind generator to shape inter-area oscillation spectrum of the wind-integrated power system in a desired pattern. The placement of a wind farm in a large power system is driven by many factors such as geographic, environmental, economic etc. If the wind farm is located at an unfavorable location leading to a lightly damped oscillatory mode, it is important that a controller on the wind farm can actually damp these modes. It is also shown in this work that the performance of the wind farm controller can be boosted by a coordinated control action with a battery energy system (BES) to shape the inter-area oscillation spectrum of the radial power system. The approach is independent of the

locations of the wind farm and the BES, and can be implemented in a decentralized fashion.

In Chapter 4, we derive a pertinent mathematical model for the wind-integrated power system consisting of synchronous generators, loads and a wind plant driven by a DFIG. We aggregate this system into multiple coherent areas, and apply a linear transformation to represent the model in terms of slow and fast states. Using this transformed system we show that the ratio of the time constant associated with the swing states to that of the wind plant can be used to characterize conditions under which the slow time-scale of the power system changes with increasing wind penetration. We further demonstrate that these modal responses depend on the relative locations of the synchronous generators, the loads and the wind generator through simulation examples in a two-area 8-bus power system and a five-area 68-bus power system.

Chapter 5 applies a homotopy based numerical continuation algorithm which is capable of exploring the power flow equilibrium and find voltage stability limit when affected by multiple wind injections. The equilibrium of conventional power systems is getting transformed due to the impact of large-scale integration of renewable energy resources like wind. Typically, in a multiple wind-injection scenario the stable equilibrium boundaries is parameterized by the penetration levels of wind. Thus identification of the relative penetration levels where the solution boundary occur is crucial to maintain voltage security from a planning perspective. The traditional load flow techniques which are based upon an initial guess followed by iterative methods are inadequate of locating all the boundaries based on different penetration levels. The proposed method however guarantees to find all solution boundaries within a given parameter space independent of any initial guess. We illustrate the proposed method through simulations on standard power system models.

Chapter 2

Spectral Response of a Wind-injected Power System Model

This chapter studies the oscillation analysis problem of a large, geographically distributed power system with wind penetration. Our system of study is a radial power transfer path, which is modeled as a continuum system leading to a hyperbolic wave equation for the phase angle defined across the path. The primary reason for studying the continuum model is to evaluate the impact of the spatial location of a wind farm on the grid dynamics, a completely new perspective. Such models have been used extensively in the past to study inter-area oscillations in the Western Electricity Coordinating Council (WECC) [20], and more recently for monitoring nationwide frequency oscillations using FNET [49]. The continuum model is considered to be integrated with a wind farm whose power is modeled as the output of its dynamic model acting as point-source forcings to the wave equation at specified electrical distances along the transfer path, $\alpha \in [0, 1]$. A Fourier analysis of the forced wave equation demonstrates that its oscillation modes are highly dependent on the power injection locations of the wind farm. This observation implies that there are siting locations for these external wind resources that can produce an unfavorable spectral response for the power flow. We illustrate our results using simulations based on a PDE based model inspired by US west coast transfer paths such as the Pacific AC

Inter-tie.

2.1 Continuum Representation of a Radial Power System with a Point Wind Injection

Consider a string of n generators distributed along a normalized spatial dimension $u \in [0, 1]$. At each bus i , we define the set $\tilde{E}_i := \{E_i, \delta_i\}$, where δ_i is the rotor phase angle and E_i is the voltage magnitude in figure 2.1. The line reactance and distance between generators i and $i + 1$ are respectively denoted x_i and ΔL . The dynamics of the i^{th} generator is given by the electro-mechanical swing equation as shown below,

$$\left(\frac{2H_i}{\Omega_s}\right) \ddot{\delta}_i + \zeta \dot{\delta}_i = P_i \quad \forall i = 1, 2 \dots n \quad (2.1)$$

where $\Omega_s = 120\pi = 377$ rad/s is the electrical frequency (assuming a 60 Hz base), P_i is the net active power flowing out of the i^{th} machine ($P_0 = 0$) and ζ is the damping coefficient. The real power flow from node i to $i + 1$ over a purely reactive line is given by,

$$P_{i,i+1} = \frac{E_i E_{i+1} \sin(\delta_i - \delta_{i+1})}{x_i}. \quad (2.2)$$

We simplify (2.2) by considering a linear power flow approximation and constant voltages. Thus, we assume small angle differences (i.e. the sine function can be approximated by a linear difference) and constant voltage, which without loss of generality means we can set $E_i = 1$ (p.u.). The expression for net active power flowing out of the i^{th} machine then becomes

$$P_i = P_{i-1,i} - P_{i,i+1} = \frac{1}{x_{i-1}}(\delta_{i-1} - \delta_i) - \frac{1}{x_i}(\delta_i - \delta_{i+1}). \quad (2.3)$$

Substituting (2.3) in (2.1), dividing by ΔL and taking the limit as $\Delta L \rightarrow 0$ results in the

| | |
|----------------|--|
| δ_i | Rotor angle of the i^{th} generator in figure 2.1 |
| H_i | Inertia of the i^{th} generator in figure 2.1 |
| ξ_i | Damping of the i^{th} generator in figure 2.1 |
| E_i | Internal voltage of the i^{th} generator in in figure 2.1 |
| P_i | Power output of the i^{th} generator in figure 2.1 |
| $P_{i,i+1}$ | Power flow from the i^{th} to the $(i+1)^{th}$ generator in figure 2.1 |
| $\delta(u, t)$ | Aggregate rotor angle at location u and time t in (2.4) |
| ν | Propagation velocity of the wave equation (2.4) |
| γ_I | Impedance density of the wave equation (2.4) |
| $P_g(t)$ | Wind farm power output |

Table 2.1: List of principle symbols in Continuum model of the Power System

following damped hyperbolic wave equation in terms of the aggregate generator angle $\delta(u, t)$

$$\frac{\partial^2 \delta(u, t)}{\partial t^2} + \xi \frac{\partial \delta(u, t)}{\partial t} = \nu^2 \frac{\partial^2 \delta(u, t)}{\partial u^2}. \quad (2.4)$$

The wave speed is defined as

$$\nu = \sqrt{\frac{377}{2H_T\gamma_I}}. \quad (2.5)$$

In (2.4) and (2.5), ξ , H_T , and γ_I respectively denote the damping, inertia, and reactance densities over the string of generators, which are derived in [20, 27]. In the continuum these densities take the form

$$H_T = \frac{1}{L} \int_0^L dH(u) = \frac{H(L)}{L}, \quad \gamma_I = \frac{x(L)}{L}, \quad \eta = \frac{\zeta(L)}{L}. \quad (2.6)$$

For n discrete generators one can approximate $H(L) = \sum_{i=1}^n H_i$, $x(L) = \sum_{i=1}^n x_i$, and $\zeta(L) = \sum_{i=1}^n \zeta_i$. The corresponding continuum expression for the power flow associated with (2.4) is

$$P(u, t) = -\frac{1}{\gamma_I} \frac{\partial \delta(u, t)}{\partial u}. \quad (2.7)$$

A wind farm can be added to this power system by considering it as point source forcing along the transfer path, as shown in Figure 2.1. We model wind farm as a point source located at a spatial location of α from one end of the path, injecting power $P_g(t)$ into the system. Therefore

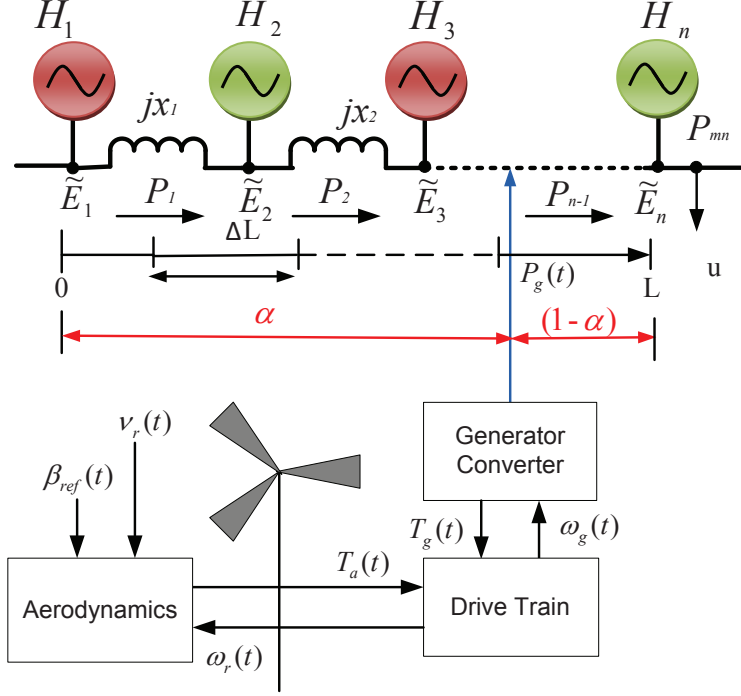


Figure 2.1: A radial power system of generators subject to wind injection at a distance α along the transfer path.

(2.4) can be written as

$$\frac{\partial^2 \delta}{\partial t^2} + \xi \frac{\partial \delta}{\partial t} - \nu^2 \frac{\partial^2 \delta}{\partial u^2} = P_g(t) \hat{\delta}(u - \alpha) \quad (2.8)$$

where $\hat{\delta}(u - \alpha)$ is the dirac-delta function, used to represent a spatial point source at $u = \alpha$.

We assume that the power flow at the boundaries are constant over time implying that $\delta(u, t)$ is a standing wave with zero slope at the boundaries [20]. The change in the power at the two ends of this tie-line can be used to define the following boundary conditions for (2.8),

$$\left[\frac{\partial \delta}{\partial u} \right]_{u=0} = \left[\frac{\partial \delta}{\partial u} \right]_{u=L} = 0. \quad (2.9)$$

The input to (2.8) is the output $P_g(t)$ of a dynamic model of a wind farm, which is described in the next section. We show the derivation of an analytical expression for the spectral response of the power system described by (2.8)-(2.9) in subsequent sections.

2.2 Wind Farm Model

In this section we derive an aggregate model for a wind farm based on a single *equivalent* wind turbine. Later we will generalize this assumption to include multiple wind turbines whose individual power outputs are added at a point of common coupling, and injected to the grid. We consider the nonlinear wind turbine model consisting of a two-mass drive train, induction generator and aerodynamic torque as presented in [92]. The drive train is modeled as two connected shafts operating at high and low speeds with respective inertias J_r and J_g , and friction coefficients B_r and B_g . The transmission gear connecting the shafts has a gear ratio of N_g , and a torsion stiffness and damping of K_{dt} and B_{dt} , respectively. The model is represented in state space in terms of its 4 states namely turbine rotor speed $\omega_r(t)$, the generator torsion angle $\theta(t)$, generator speed $\omega_g(t)$ and torque $T_g(t)$ as,

$$J_r \dot{\omega}_r(t) = \frac{B_{dt}}{N_g} \omega_g(t) - K_{dt} \theta(t) - (B_{dt} + B_r) \omega_r(t) + T_a(t) \quad (2.10a)$$

$$J_g \dot{\omega}_g(t) = \frac{B_{dt}}{N_g} \omega_r(t) + \frac{K_{dt}}{N_g} \theta(t) - \left(\frac{B_{dt}}{N_g^2} + B_g \right) \omega_g(t) - T_g(t) \quad (2.10b)$$

$$\dot{\theta}(t) = \omega_r(t) - \frac{1}{N_g} \omega_g(t) \quad (2.10c)$$

$$\dot{T}_g(t) = -\frac{1}{\tau_g} T_g(t) + \frac{1}{\tau_g} T_{g,ref}(t). \quad (2.10d)$$

where, $T_a(t)$ is the aerodynamic torque, and $T_{g,ref}$ is a reference generator torque. The aerodynamic torque $T_a(t)$ is

$$T_a(t) = \frac{\rho A_s v_r^3(t) C_p(t)}{2 \omega_r(t)} \quad (2.11)$$

where ρ is air density, A_s is the total swept area of the turbine blade, $C_p(t)$ is the power coefficient, and $v(t)$ is the wind speed. The dynamics of (2.10d) are orders of magnitude faster than (2.10a)-(2.10c). We, therefore, assume $T_g(t)$ to be a constant that we denote $T_{g,ref}$. The output power generation of the open-loop turbine model is given by

$$P_g(t) = \eta_g \omega_g(t) T_g(t), \quad (2.12)$$

where η_g is the generator efficiency. $P_g(t)$ defines the forcing term in (2.8). We linearize the model (2.10)-(2.11) about an operating point $(\omega_{g,0}, \omega_{r,0}, \theta_0, T_g)$ and obtain a frequency response for the linearized power flow. The frequency response of the linearized power output of the wind farm is used to compute the frequency response of the power system described in (2.8)-(2.9).

2.3 Computation of the Spectral Response of the Wind-injected Power System

We next derive an expression for the spectral response of (2.8) in terms of the the wind farm transfer function associated with $P_g(t)$. We begin by expressing $\delta(u, t)$ and $W(u, t)$ in terms of Fourier series expansion as shown below [27],

$$\delta(u, t) = \frac{1}{2}A_0 + \sum_{n=1}^{\infty} [A_n(t) \cos(k_n u) + B_n(t) \sin(k_n u)] \quad (2.13a)$$

$$W(u, t) = \frac{1}{2}F_0 + \sum_{n=1}^{\infty} [F_n(t) \cos(k_n u) + G_n(t) \sin(k_n u)] \quad (2.13b)$$

where k_n is the wave number of each mode λ_n . We assume that the power flow at the boundaries are constant over time implying that $\delta(u, t)$ is a standing wave with zero slope at the boundaries and power flow given as

$$p(0, t) = p(1, t) = 0. \quad (2.14)$$

Using (2.14) it is easy to show that $B_n(t) = G_n(t) = 0$. Then substituting (2.13a) and (2.13b) into (2.8) yields

$$\frac{d^2 A_n(t)}{dt^2} + \eta \frac{dA_n(t)}{dt} - \nu^2 k_n^2 A_n(t) = F_n(t) \quad (2.15)$$

where the Fourier coefficient $F_n(t)$ follows from

$$F_n(t) = 2 \int_0^1 \cos(k_n u) W(u, t) du. \quad (2.16)$$

where

$$W(u, t) = P_g(t)\hat{\delta}(u - \alpha). \quad (2.17)$$

Substituting (2.17) in (2.16) and solving we get

$$F_n(t) = 2P_g(t) \cos(k_n \alpha). \quad (2.18)$$

Then the frequency response of $A_n(t)$ from (2.15) depends on the location α and is given by

$$A_n(\alpha, j\omega) = \frac{2M_n(\omega) [\cos(\theta_n) + j \sin(\theta_n)]}{\sqrt{(k_n^2 \nu^2 - \omega^2)^2 + (\xi\omega)^2}} \quad (2.19)$$

where

$$M_n(\omega) = |F_n(j\omega, \alpha)|, \quad (2.20)$$

and θ_n is the phase of A_n , which is

$$\theta_n = \angle F_n(j\omega, \alpha) - \tan^{-1} \left(\frac{\xi\omega}{k_n^2 \nu^2 - \omega^2} \right). \quad (2.21)$$

The net spectral response of the power flow, given by (2.8) at a certain location u is given by,

$$S_P(\omega, \alpha) = \frac{1}{\gamma_I^2} \sum_{n=1}^{\infty} |A_n(\alpha, j\omega)|^2 \sin^2(k_n u) \quad (2.22)$$

2.4 Simulation Results

In this section we study the spectral response of the power flow in the wind integrated power system derived in (2.22) which has two discrete parts, the frequency response of the wind farm power output $P_g(t)$ shown in Section 2.2 and the frequency response of the grid power flow shown in Section 2.3. These are described as follows

2.4.1 Spectral Response of the Wind Farm

We first obtain a linearized model of the wind farm described by (2.10)-(2.11) and (2.12) about an operating point $(\omega_{g,0}, \omega_{r,0}, \theta_0, T_g)$ and represent the system in terms of a transfer function. The transfer function of the wind farm is calculated based on the parameters of the wind farm, given in [92], shown as: $J_r = 55 \times 10^6 \text{ kgm}^2$, $J_g = 390 \text{ kgm}^2$, $B_r = 27.8 \times 10^3 \text{ Nm}/(\text{rads}/\text{s})$, $B_g = 3.034 \text{ Nm}/(\text{rads}/\text{s})$, $B_{dt} = 945 \text{ kNm}/(\text{rads}/\text{s})$, $K_{dt} = 2.7 \times 10^9 \text{ Nm}/\text{rad}$, $N_g = 95$, $\tau_g = 10 \text{ ms}$, $A_s = 10387 \text{ m}^2$, $\rho = 1.225 \text{ kg}/\text{m}^3$, $T_{g,ref} = 2500 \text{ Nm}$, $\eta_g = 0.92$ and an input $T_a(t) = 1.6$. With these parameters and assumption of $T_g(t) = \tilde{T}_{g,ref} = 2500 \text{ Nm}$ for all time t , the transfer function of the wind farm power output is given as,

$$G_w(s) = \frac{6.786s + 1.939e004}{s^3 + 0.294s^2 + 816.2s + 0.7696}. \quad (2.23)$$

The Bode Magnitude response for the transfer function is shown as Figure 2.2a while Figure 2.2b shows the step response of the transfer function $G_w(s)$ of the wind power output. The spectral response of the wind power output is used to compute the power flow spectrum of the entire power system as shown next.

2.4.2 Spectral response of the Power Flow in the Grid

We compute the spectral response of the power flow in the wind integrated power system derived in (2.22) using the following parameters $\gamma^I = 3.13 \times 10^{-3} \text{ rad}/\text{MW}$, $\xi = 0.4 / \text{sec}$, $\nu = 0.4 \text{ rad}/\text{sec}$ and $u = 0.25$ as in [20]. Figure 2.3 shows the spectrum of power flow of a wind-integrated power system with power injection from a single wind farm at location α as shown in in Figure 2.1. The figure illustrates that as wind farm site is varied from $\alpha = 0$ to 0.5 the spectrum shows notable changes in both its period and the frequencies corresponding to the associated peaks and troughs. Note, that system is symmetric so only results for $\alpha \in [0, 0.5]$ are reported. The variation in frequency response with wind injection location clearly reveals that for certain locations of the wind power, the spectral response of the grid may show poorly damped modes

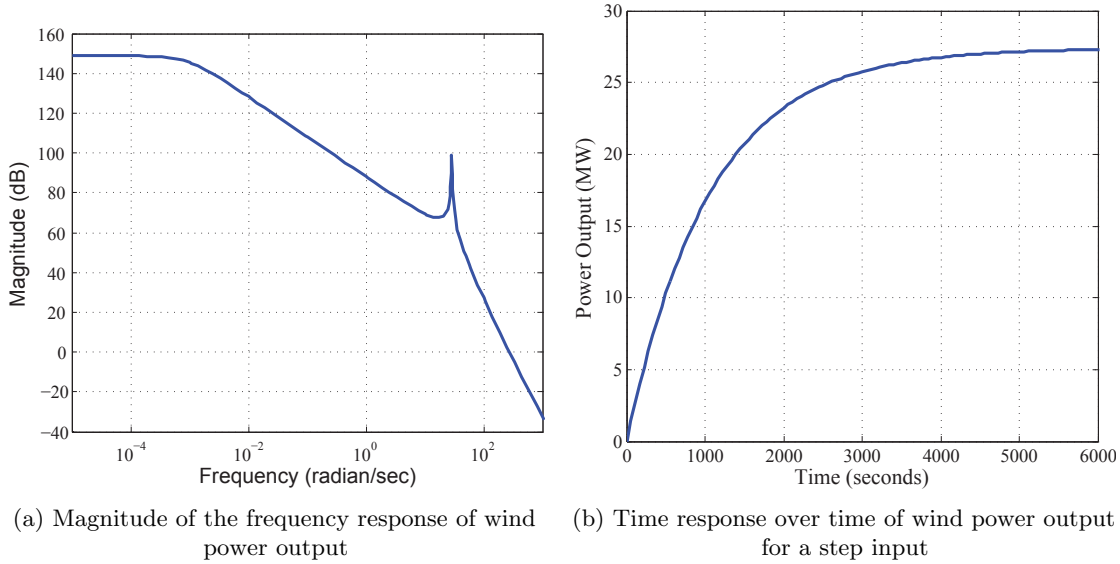


Figure 2.2: Frequency and time domain response of the power output from the linearized wind farm model in (2.23)

or sharp peaks in the spectral response. In the next section we look to design the frequency spectrum of the power flow of the grid like a desired response with a wind farm at any arbitrary location using a wind power controller [28].

2.5 Conclusions

This chapter presents a method to compute the spectral response of power flow in a wind integrated power system. The study further demonstrates in theory and in simulation that the spatial location of a wind farm installed in a large distributed-parameter power system significantly affects its inter-area oscillations. The results indicate that siting a wind power plant in a good location can provide effective damping to a given set of modes. So if due to some limitations a wind farm is sited in an unfavorable location, additional damping may be required for modes with low damping. Next we will like to design closed-loop wind farm controllers which might be able to shape the inter-area spectrum of power flow for arbitrary wind farm locations.

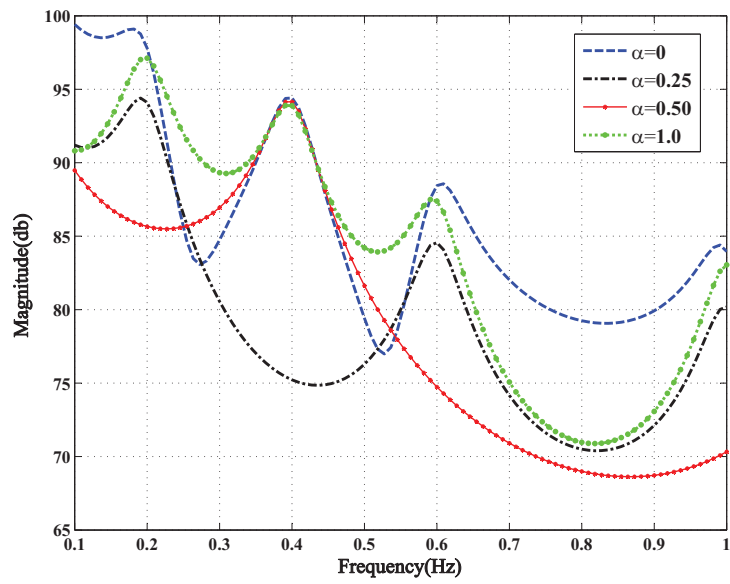


Figure 2.3: Spectral response of power flow of a wind-integrated power system for different wind farm power injection locations α .

Chapter 3

Damping of Inter-area Oscillations in Power Systems: A Frequency Domain Approach

In Chapter 2 we have shown results based on a continuum model of a radial power system, which demonstrate that the inter-area oscillation spectrum of the wind-integrated power system is strongly influenced by the wind farm injection location α [27]. But the location of a wind installation in a geographically diverse power system may be limited by several issues like geographical, economic, political etc. In a situation where the wind farm location is not ideal, it may give rise to poorly damped inter-area oscillatory modes in the power system, detrimental for its normal operation. In this scenario, we aim to design closed loop controllers for the wind farm which can allow us to shape the inter-area oscillation spectrum of the power flow in a desired pattern. We assume that given a frequency range of interest, a particular wind power injection point α^* produces the so-called optimal (most desirable) frequency response without any controller. However if the situation is such that a wind farm could not be installed at this α^* , a closed loop controller of the wind farm power output at location α shapes the oscillation spectrum to match the desired response (i.e., the response associated with α^*) [28]. The primary

drawback of this approach is that this matching can only be guaranteed over narrow frequency bands necessitating frequent switching of controllers from one band to another.

We provide a means to circumvent this problem by designing co-dependent controllers for the wind farm power output and a controlled Battery Energy System (BES) by which we achieve a better match of the spectral response of the system to the so-called optimal response [11,14]. Usually many wind installations have a storage associated with it on the same bus to improve their reliability. We look to exploit the available power electronic controllers of the BES for our control design. The design is posed as a parametric optimization problem that minimizes the error between the two spectral functions over a finite range of frequencies. We introduce a realistic two-loop control strategy for the wind speed and power control. This two-loop control system is based on a maximum power-point tracking wind turbine controller, and is, therefore, a more realistic design for real-time implementation [11]. Secondly we develop dis-aggregation methods for implementing controllers at each individual wind turbine instead of using a hypothetical equivalent turbine to represent the wind farm. We illustrate the typical closed-loop dynamic performance trade-offs when aggregate control systems get distributed among individual turbines [11]. Our results take into account the typical power output patterns of the different rows of a wind farm, and, thereby, capture the variations in wind speed due to wake effects.

3.1 Centralized Control Design for Spectral Matching

3.1.1 Wind Farm Model and Controller Design

In this section we use the aggregate model for the wind farm based on a single *equivalent* wind turbine shown in section 2.2. We next linearize the model (2.10)-(2.11) about an operating point $(\omega_{g,0}, \omega_{r,0}, \theta_0, T_{g,ref})$. The operating point is obtained from the power-speed characteristics of the wind turbine illustrated in Figure 3.1, where the maximum power curve indicates the amount of turbine power that can be harnessed for different wind speeds. The states of the

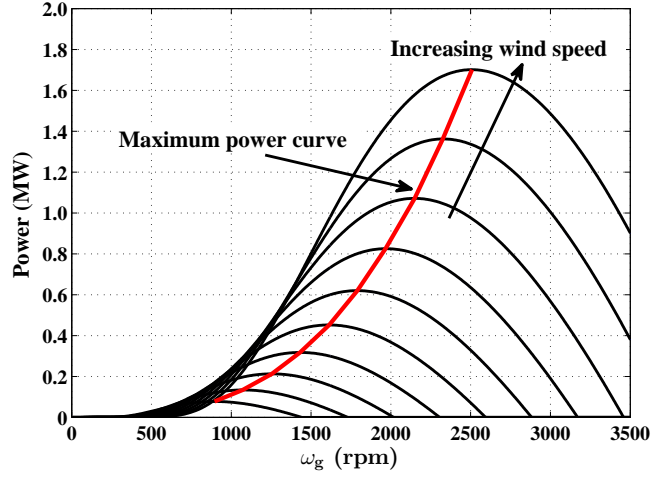


Figure 3.1: Steady-state speed versus power characteristics of a 1 MW wind turbine. The maximum power curve, shown in red, depicts the operating points for each wind speed.

linearized system are then the small-signal changes from the equilibrium that we denote as $\xi = [\Delta\omega_g, \Delta\omega_r, \Delta\theta]^T$. We next define the corresponding inputs as $\phi = [\Delta v_r, \Delta T_g]^T$ to obtain

$$\dot{\xi} = A\xi + B\phi \quad (3.1)$$

where,

$$A = \begin{bmatrix} -\frac{(B_{dt}+B_r)}{J_r} - \frac{\rho A_s v_{r,0}^3 C_p}{2\omega_{r,0}^2 J_g} & \frac{B_{dt}}{N_g J_r} & -\frac{K_{dt}}{J_r} \\ \frac{B_{dt}}{N_g J_g} & -\frac{1}{J_g} \left(\frac{B_{dt}}{N_g^2} + B_g \right) & \frac{K_{dt}}{N_g J_g} \\ 1 & -\frac{1}{N_g} & 0 \end{bmatrix}$$

$$B = \begin{bmatrix} \frac{3\rho A_s v_{r,0}^2 C_p}{2\omega_{r,0} J_g} & 0 \\ 0 & \frac{-1}{J_g} \\ 0 & 0 \end{bmatrix}.$$

The linearized output equation (2.12) is

$$\Delta P_g(t) = \eta_g \omega_{g0} \Delta T_g + \eta_g \Delta \omega_g T_{g,ref}. \quad (3.2)$$

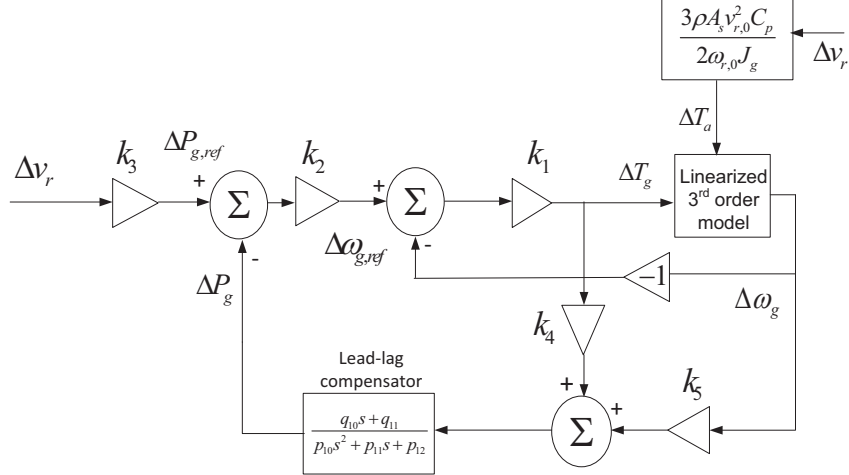


Figure 3.2: Two-loop control scheme for wind turbine in which the inner loop controls generator speed set points shown in Figure 3.1 while the outer loop is the proposed power controller for shaping the inter-area oscillation spectrum of the grid.

Defining the two outputs $y = [\Delta P_g, \Delta \omega_g]^T$, the output equation is given by

$$y = C\xi + D\phi \quad (3.3)$$

$$\text{where } C = \begin{bmatrix} 0 & k_5 & 0 \\ 0 & 1 & 0 \end{bmatrix}, \quad D = \begin{bmatrix} 0 & k_4 \\ 0 & 0 \end{bmatrix},$$

$k_4 := \eta_g \omega_{g,0}$ and $k_5 := \eta_g T_{g,ref}$.

Following standard practice, we assume that the steady-state power output of the turbine is controlled to achieve its maximum power for a given wind speed v_r (as shown in Figure 3.1) using a maximum power-point tracking (MPPT) algorithm, e.g. as in [21]. The power output controller that we are going to design in this work will be implemented on top of this MPPT. The control scheme is shown in Figure 3.2, where the constants k_1 , k_2 and k_3 are defined as follows. When the wind speed changes by a small amount Δv_r from the equilibrium speed, the slope k_3 of the power versus wind speed characteristics at the point of linearization generates a new reference $\Delta P_{g,ref}$ for the power output of the turbine. The slope k_2 of the

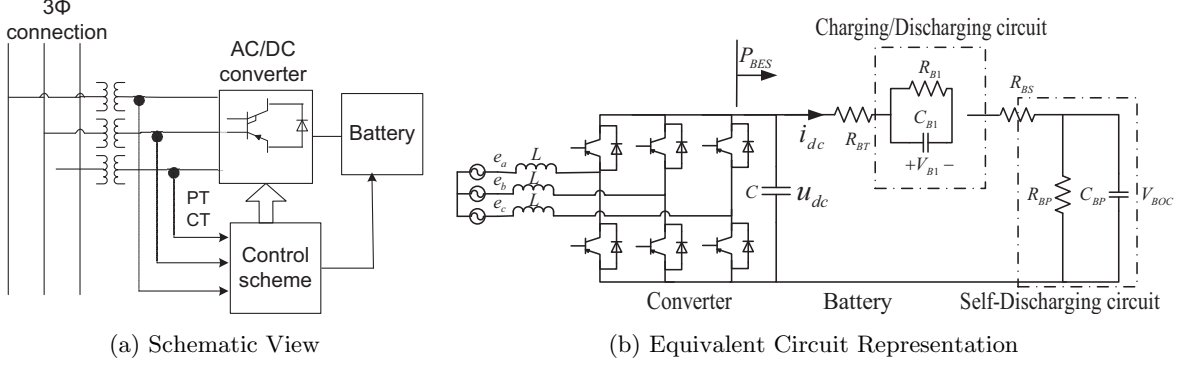


Figure 3.3: Battery Energy System (BES).

power versus generator speed characteristics, in turn, generates a new reference $\Delta\omega_{g,ref}$ for the generator speed. The product of this speed reference and the slope k_1 of the speed versus torque characteristics is then imparted as the new generator torque, as indicated in Figure 3.1. We first design a unity-gain feedback to regulate $\Delta\omega_g$ to its reference. This loop is referred to as the inner loop, which typically has a bandwidth higher than 10 Hz. The outer loop consists of feeding back both the generator torque and the generator speed, after proper scaling, to control the transient response of the generator output power $\Delta P_g(t)$ using a linear feedback controller. In general, there is no restriction on the choice of the outer-loop controller as long as it guarantees closed-loop stability and transient performance. For simplicity, we select a second-order lead-type controller of the form

$$G_i(s) = \frac{q_{10}s + q_{11}}{p_{10}s^2 + p_{11}s + p_{12}} \quad (3.4)$$

and define the set of controller parameters $\mathcal{S}_1 := \{q_{10}, q_{11}, p_{10}, p_{11}, p_{12}\}$. In the following subsections we show the BES model and the formulation of the control design problem in terms of optimizing \mathcal{S}_1 to obtain a desired $P_g(t)$ in (2.17) corresponding to a desired frequency response for the power flow (2.7).

3.1.2 BES Model and Controller Design

Here we present the dynamic model of the BES, and derive an expression for its output power $P_{BES}(t)$, which is going to supplement $P_g(t)$. As shown in Figure 3.3a, the BES model has 4 parts: a three-phase transformer, a pulse-width modulation (PWM) based AC-DC converter, a battery model, and a controller [50]. The transformer is used to step down the grid voltage to the battery level. The battery model usually consists of a set of batteries connected in series or parallel. For our study, however, we will consider an ideal transformer with a single equivalent battery model. The circuit diagram of the BES is given in Figure 3.3b. The necessary circuit analysis and subsequent linearization of the system considered here are described as follows. Table 3.1 provides a list symbols used in the following discussion.

The average model of the three-phase PWM converter shown in Figure 3.3b, assuming a $dq0$ reference frame [16], can be expressed as

$$L \frac{d}{dt} \begin{bmatrix} i_d \\ i_q \\ i_0 \end{bmatrix} = \begin{bmatrix} d_d \\ d_q \\ d_0 \end{bmatrix} u_{dc} + \begin{bmatrix} 0 & \omega & 0 \\ -\omega & 0 & 0 \\ 0 & 0 & 0 \end{bmatrix} \begin{bmatrix} i_d \\ i_q \\ i_0 \end{bmatrix} - \begin{bmatrix} e_d \\ e_q \\ e_0 - \sqrt{3}u_n \end{bmatrix} \quad (3.5a)$$

$$C \frac{du_{dc}}{dt} = i_{dc} - \begin{bmatrix} d_d & d_q & d_0 \end{bmatrix} \begin{bmatrix} i_d \\ i_q \\ i_0 \end{bmatrix} \quad (3.5b)$$

In this nonlinear converter model the control inputs are the three duty cycles d_d, d_q and d_0 . However, for simplicity, here we limit our control design to only a single-input converter model. For this we consider the small-signal changes of the three duty cycles to be the same, i.e. $\Delta d_d = \Delta d_q = \Delta d_0 := \Delta d$, and use Δd as the effective control input. Note that the equilibrium values of d_d, d_q and d_0 may be different. The linearized converter model with Δd as the control

input can be written as

$$M_1 \frac{d}{dt} \begin{bmatrix} \Delta i_d \\ \Delta i_q \\ \Delta i_0 \\ \Delta u_{dc} \end{bmatrix} = M_2 \begin{bmatrix} \Delta i_d \\ \Delta i_q \\ \Delta i_0 \\ \Delta u_{dc} \end{bmatrix} + M_3 \Delta d + \begin{bmatrix} 0 \\ 0 \\ 0 \\ 1 \end{bmatrix} \Delta i_{dc} \quad (3.6)$$

where,

$$M_1 := \text{diag}(L, L, L, C)$$

$$M_2 := \begin{bmatrix} 0 & \omega & 0 & d_{d*} \\ -\omega & 0 & 0 & d_{q*} \\ 0 & 0 & 0 & d_{0*} \\ d_{d*} & d_{q*} & d_{0*} & 0 \end{bmatrix}, \quad M_3 := \begin{bmatrix} u_{dc*} \\ u_{dc*} \\ u_{dc*} \\ -(i_{d*} + i_{q*} + i_{0*}) \end{bmatrix}.$$

The subscript ‘*’ denotes the point of linearization. Furthermore, assuming that the converter circuit dynamics is significantly faster than the battery dynamics, or in other words L and C in (3.5a)-(3.5b) are negligibly small, we obtain the following algebraic relationship between the states $[\Delta i_d, \Delta i_q, \Delta i_0, \Delta u_{dc}]$ and the control input Δd :

$$\begin{bmatrix} \Delta i_d \\ \Delta i_q \\ \Delta i_0 \\ \Delta u_{dc} \end{bmatrix} = -M_2^{-1} M_3 \Delta d - M_2^{-1} \begin{bmatrix} 0 \\ 0 \\ 0 \\ 1 \end{bmatrix} \Delta i_{dc} \quad (3.7)$$

Simplifying (3.7), we obtain

$$\Delta u_{dc}(t) = \frac{u_{dc*}}{d_{0*}} \Delta d(t). \quad (3.8)$$

Analyzing the battery circuit, on the other hand, we get

$$\Delta u_{dc}(s) = \Delta i_{dc}(s) (R_{BS} + R_{BT} + r_1 + r_2), \quad (3.9)$$

| | |
|-----------------------|--|
| L and C | Filter inductance and dc-link capacitance |
| e_d, e_q and e_0 | $dq0$ components of the transformer secondary voltage |
| i_d, i_q and i_0 | $dq0$ components of the current at the transformer secondary |
| d_d, d_q and d_0 | $dq0$ components of the duty cycle |
| u_{dc} and i_{dc} | Terminal voltage and current of the equivalent battery |
| ω | Synchronous frequency of the grid |
| u_n | Neutral point voltage |
| R_{BT} | Equivalent resistance of parallel/series connection of batteries |
| R_{BS} | Series resistance of the battery |
| P_{BES} | Active power of the BES |
| V_{B1} | Battery overvoltage |
| R_{B1} and C_{B1} | Charging circuit resistance and capacitance (Figure 3.3b) |
| R_{BP} and C_{BP} | Battery self-discharge resistance and capacity (Figure 3.3b) |

Table 3.1: List of principle symbols in BES model

where $r_1 := \frac{R_{B1}}{1+sR_{B1}C_{B1}}$ and $r_2 := \frac{R_{BP}}{1+sR_{BP}C_{BP}}$, R_{BT} is the equivalent resistance of a parallel/series connection of batteries, and R_{BS} is the internal resistance of the battery. The parallel circuit of R_{BP} and C_{BP} is used to represent the self discharge of the battery while the charging or discharging circuit corresponds to a parallel combination of R_{B1} and C_{B1} . The small-signal expression of the active power fed to the system is then given by

$$\Delta P_{BES} = u_{dc0} \Delta i_{dc} + i_{dc0} \Delta u_{dc}. \quad (3.10)$$

Substituting (3.8) and (3.9) in (3.10), we obtain a transfer function of the system as

$$\Delta P_{BES}(s) = \left(\frac{u_{dc0}}{F(s)} + i_{dc0} \right) \frac{u_{dc0}}{d_{00}} \Delta d(s) \quad (3.11)$$

where,

$$F(s) := \frac{R_{BP} + R_{B1} + sR_{BP}R_{B1}(C_{BP} + C_{B1})}{(1 + sR_{BP}C_{BP})(1 + sR_{B1}C_{B1})} + R_{BS} + R_{BT}.$$

This power $\Delta P_{BES}(s)$ defined in (3.10) is controlled using a second-order lead controller of the

form

$$G_{c_{BES}}(s) = \frac{q_{20}s + q_{21}}{p_{20}s^2 + p_{21}s + p_{22}} \quad (3.12)$$

with parameters $\mathcal{S}_2 = \{q_{20}, q_{21}, p_{20}, p_{21}, p_{22}\}$. A unit step response of the closed-loop BES model is denoted as $P_{BES}(t)$ which is injected in the power system.

3.1.3 Spectral Analysis

A wind farm and a battery energy system (BES) described in subsections 3.1.2 and 3.1.2 respectively, are incorporated in the power system into (2.4). We consider the wind farm power injection $P_g(t)$ and the BES as drawing power $P_{BES}(t)$ as a point source forcing at location α from one end of the transfer path. This leads to the forced wave equation

$$\frac{\partial^2 \delta}{\partial t^2} + \xi \frac{\partial \delta}{\partial t} - \nu^2 \frac{\partial^2 \delta}{\partial u^2} = W(u, t), \quad (3.13)$$

where

$$W(u, t) = (P_g(t) - P_{BES}(t))\hat{\delta}(u - \alpha) \quad (3.14)$$

is the net power injected into the system. We use the dirac-delta function $\hat{\delta}(u - \alpha)$ to represent the spatial point source at $u = \alpha$. In equation (3.14) we use the convention that $P_{BES} \geq 0$ represents charging (i.e. the BES is a power sink) and $P_{BES} < 0$ is discharging (i.e. the PES is a power source). We next derive the expressions for the spectral response of (3.13) in terms of the the closed-loop transfer functions associated with $\Delta P_g(t)$ and $\Delta P_{BES}(t)$ by applying Fourier series as shown in section 2.3. We begin by expressing $\delta(u, t)$ and $W(u, t)$ in terms of Fourier series

$$\delta(u, t) = \frac{1}{2}A_0 + \sum_{n=1}^{\infty} [A_n(t) \cos(k_n u) + B_n(t) \sin(k_n u)] \quad (3.15a)$$

$$W(u, t) = \frac{1}{2}F_0 + \sum_{n=1}^{\infty} [F_n(t) \cos(k_n u) + G_n(t) \sin(k_n u)] \quad (3.15b)$$

where k_n is the wave number of each mode λ_n . We assume that the power flow at the two boundaries are zero, i.e.,

$$p(0, t) = p(1, t) = 0 \quad (3.16)$$

implying that $\delta(u, t)$ is a standing wave with zero slope at the boundaries. Using (2.14) it is easy to show that $B_n(t) = G_n(t) = 0$. Then substituting (3.15a) and (3.15b) into (3.13) yields

$$\frac{d^2 A_n(t)}{dt^2} + \eta \frac{dA_n(t)}{dt} + \nu^2 k_n^2 A_n(t) = F_n(t) \quad (3.17)$$

where the Fourier coefficient $F_n(t)$ follows from (3.14) as

$$F_n(t) = 2(P_g(t) - P_{BES}(t)) \cos(k_n \alpha). \quad (3.18)$$

The frequency response of (3.18) can be written as

$$F_n(j\omega, \mathcal{S}_1, \mathcal{S}_2, \alpha) = 2 [P_g(j\omega, \mathcal{S}_1) - P_{BES}(j\omega, \mathcal{S}_2)] \cos(k_n \alpha). \quad (3.19)$$

The corresponding power flow equation is given by

$$p(u, \alpha, t) = \frac{1}{\gamma_I} \sum_{n=1}^{\infty} k_n A_n(\alpha, t) \sin(k_n u). \quad (3.20)$$

Taking the Fourier transform of (3.20), we get

$$\mathcal{P}(u, \alpha, \omega) = \frac{1}{\gamma_I} \sum_{n=1}^{\infty} k_n A_n(\alpha, \omega) \sin(k_n u), \quad (3.21)$$

where

$$A_n(\alpha, \omega) = \frac{|F_n(j\omega, \mathcal{S}_1, \mathcal{S}_2, \alpha)|}{[(k_n^2 \nu^2 - \omega^2)^2 + \eta^2 \omega^2]^{1/2}} (\cos \theta_n + j \sin \theta_n)$$

with $\theta_n = \angle F_n(j\omega, \mathcal{S}_1, \mathcal{S}_2, \alpha) - \tan^{-1} \left(\frac{\xi\omega}{k_n^2 \nu^2 - \omega^2} \right)$. The net spectral response of the system (2.8) at a certain location u with the wind farm and BES at α can finally be written as,

$$S_{P_{cl}}(u, \omega, \mathcal{S}_1, \mathcal{S}_2, \alpha) = |\mathcal{P}(u, \alpha, \omega, \mathcal{S}_1, \mathcal{S}_2)|^2. \quad (3.22)$$

From now onwards, we will drop u from the arguments of $S_{P_{CL}}(\cdot)$ for brevity, knowing that the frequency response is always computed at a fixed spatial location.

The control problem formulated is to design the parameter sets \mathcal{S}_1 and \mathcal{S}_2 such that $S_{P_{cl}}(\omega, \mathcal{S}_1, \mathcal{S}_2, \alpha)$ at any fixed u matches a desired spectral response over a given frequency range. In general, this desired spectral response can be chosen arbitrarily depending on the control objective. The formulation of the design pursued in this chapter is as follows. We first consider the open-loop frequency response $S_P(\omega, \alpha)$ of the wind-integrated power system without the controllers \mathcal{S}_1 and \mathcal{S}_2 , i.e. ($\mathcal{S}_1 = 0, \mathcal{S}_2 = 0$ in (2.22)). Next, we identify the location α_2 for which the frequency response over $\omega \in [\omega_1, \omega_2]$ has the most favorable damping. Ideally, in that case, one would place a wind farm and BES at α_2 , but that may not be always possible due to various geographic, economic and political constraints. Then, one way to solve the problem would be to treat the spectrum at $u = \alpha_2$ as a reference, install the wind farm at a viable location $u = \alpha_1$, and design the controllers \mathcal{S}_1 and \mathcal{S}_2 such that the spectrum $S_{P_{cl}}(\omega, \mathcal{S}_1, \mathcal{S}_2, \alpha_1)$ closely matches the reference spectrum over $\omega \in [\omega_1, \omega_2]$. The controller design can then be written as the following optimization problem:

$$\min_{\mathcal{S}_1, \mathcal{S}_2} \int_{\omega_1}^{\omega_2} [\log(S_{P_{cl}}(\omega, \alpha_1, \mathcal{S}_1, \mathcal{S}_2)) - \log(S_P(\omega, \alpha_2))]^2 d\omega. \quad (3.23)$$

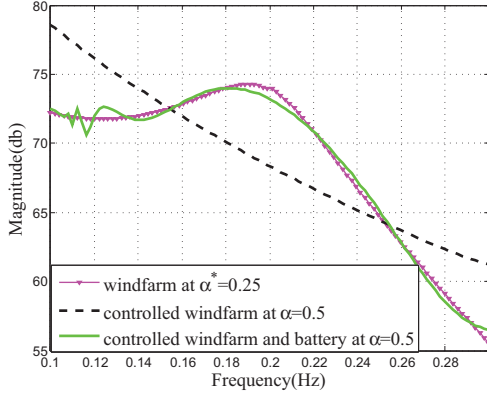
The controllers must also guarantee closed-loop stability of the wind turbine and the BES. Next we show simulation results which demonstrate the spectral matching of the of the power system oscillations with the controller.

| Frequency range | \mathcal{S}_1 | \mathcal{S}_2 |
|-----------------|---------------------------------|---------------------------------|
| 0.1 to 0.3 Hz | [1.604 1.210 0.909 1.392 0.835] | [2.354 0.893 1.521 0.059 0.612] |
| 0.3 to 0.5 Hz | [1.438 0.785 0.718 1.055 0.313] | [1.495 1.786 1.844 0.038 1.571] |
| 0.5 to 0.7 Hz | [0.836 1.020 0.698 0.917 2.398] | [2.455 2.355 0.575 0.976 0.340] |
| 0.7 to 0.9 Hz | [1.185 0.951 0.383 0.584 1.317] | [0.967 0.192 1.766 1.235 0.808] |

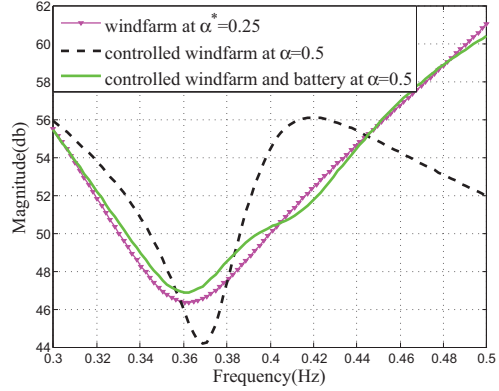
Table 3.2: Optimal controller parameters sets

3.1.4 Simulation Results

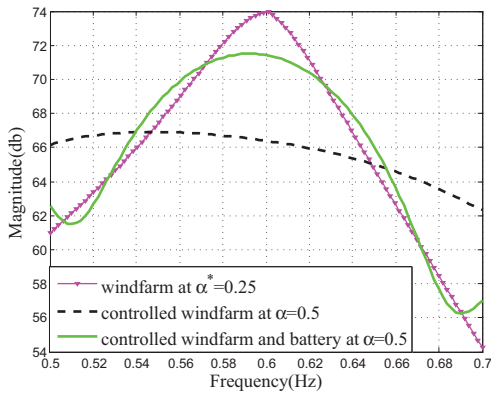
We consider a case where both the wind farm and the BES are located at $\alpha = 0.5$, while the system planner desires the controlled spectral response of the grid to match the response of the system corresponding to $\alpha^* = 0.25$. Following [50] we assume $\beta_R = 85^\circ$, the transformer secondary voltage as 5 KV, $R_{BT} = 0.0167 \Omega$, $R_{BS} = 0.013 \Omega$, $X_{C0} = 0.0274 \Omega$, $R_{B1} = 0.001 \Omega$, $C_{B1} = 1 \text{ F}$, $R_{BP} = 10 \text{ k}\Omega$, and $C_{BP} = 52600 \text{ F}$. We then design controllers of the form (3.4) and (3.12) for the wind farm and BES systems using the procedure described in the subsection 3.1.3. Figure 3.4 compares the net spectral response this controlled system to the desired response over four different frequency ranges. Figure 3.4a illustrates the results when the optimization algorithm (3.23) is run with $\omega_1 = 0.2\pi \text{ rad/s}$, $\omega_2 = 0.4\pi \text{ rad/s}$. The corresponding controller parameters are $\mathcal{S}_1 = [0 \ 0.067 \ 1.894 \ 1.732 \ 3.276]$ and $\mathcal{S}_2 = [0 \ 0.143 \ 1.366 \ 1.176 \ 4.038]$. This particular controller does not work well beyond $\omega_2 = 0.4\pi \text{ rad/s}$. Therefore, we design a new controller for that parameter range. Figures 3.4b-3.4d shows the results of three controller parameter optimizations for the respective frequency ranges $f \in [0.3, 0.5] \text{ Hz}$, $f \in [0.5, 0.7] \text{ Hz}$ and $f \in [0.7, 0.9] \text{ Hz}$. The controller parameters obtained for all of the frequency ranges shown in Figures 3.4 are given in Table 3.2. Although none of these controllers can match the desired response over the entire inter-area oscillation spectrum, the results show that the addition of the BES greatly improves the matching of the frequency response over the case with only a wind power controller. The fact that different controllers are required to affect the response over different frequency ranges suggests that a gain scheduling approach may yield better matching over larger frequency band. In the next section we describe the strategy for



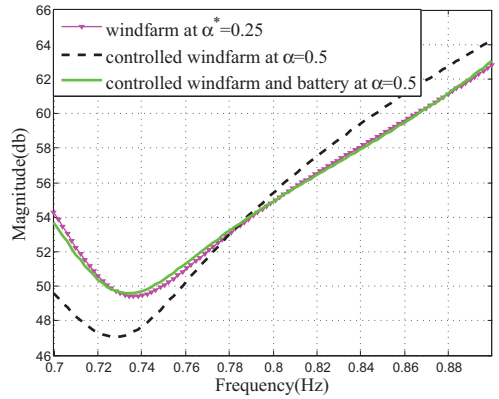
(a) Comparison in the range of 0.1 to 0.3 Hz



(b) Comparison in the range of 0.3 to 0.5 Hz



(c) Comparison in the range of 0.5 to 0.7 Hz



(d) Comparison in the range of 0.7 to 0.9 Hz

Figure 3.4: Spectral response comparison

solving this optimization problem, and generalize the *equivalent* turbine model to account for a decentralized system with controllers at each individual turbine.

3.2 Disaggregation of Control from Equivalent Turbine to Multiple Turbines

In section 3.1 we assumed that the wind farm consists of a single aggregate turbine with an induction generator. In reality, however, there are multiple wind turbines in a wind farm, and therefore, the control design needs to be implemented at each individual turbine, as shown in

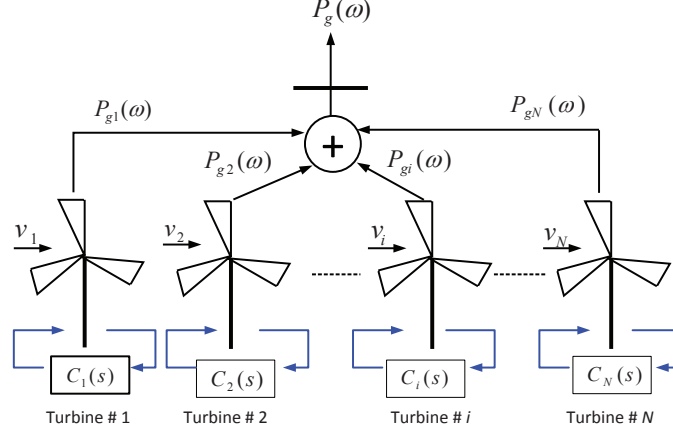


Figure 3.5: Schematic for the disaggregated wind farm control, where each turbine is controlled individually, and the total power output of the farm is aggregated and injected to the grid at the point of common coupling.

Figure 3.5. This can be done in either of the following two ways.

3.2.1 Centralized Design

Let the total number of turbines in the farm be N . Let the controller for the i^{th} turbine be

$$G_i(s) = \frac{q_{i0}s + q_{i1}}{p_{i0}s^2 + p_{i1}s + p_{i2}} \quad (3.24)$$

with its parameters denoted by the set $\mathcal{S}_{1i} = \{q_{i0}, q_{i1}, p_{i0}, p_{i1}, p_{i2}\}$, where $i = 1, \dots, N$. The parameters of all N turbines can then be designed in a batch fashion to solve a modified optimization problem

$$\min_{\mathcal{S}_{1i}, \mathcal{S}_2} \int_{\omega_1}^{\omega_2} [\log(S_{P_{cl}}(\omega, \alpha, \mathcal{S}_{11}, \dots, \mathcal{S}_{1N}, \mathcal{S}_2)) - \log(S_P(\omega, \alpha^*))]^2 d\omega, \quad i = 1, \dots, N. \quad (3.25)$$

However, there are two shortcomings of this approach. First, the computation time to solve the optimization problem scales with N , and, therefore, the solution may take a very long time to converge. Another disadvantage of this approach is that it does not account for the fact that the power output from the first row of turbines is generally much higher than that of

the subsequent rows. For example, the second and subsequent rows typically produce about 60% of the power generated by the first row [87]. The centralized optimization (3.25) searches for the optimal controller parameters to minimize the integral error between the frequency spectra of the wind-integrated power system, and, therefore, will not necessarily guarantee this distribution of row-wise power outputs. Additional constraints may be placed on the search of \mathcal{S}_{1i} and \mathcal{S}_2 to satisfy this criteria, but that will increase the computational time. To overcome these shortcomings we next describe an alternative approach.

3.2.2 Decentralized Design

This design consists of two steps. First, solve the optimization problem (3.23) assuming a single aggregate wind turbine with an aggregate controller \mathcal{S}_1 . Then, compute the closed-loop frequency response $P_g(\omega)$ of the total power injected by the wind farm to the grid over the desired frequency range $\omega \in [\omega_1, \omega_2]$. Next, consider that the i^{th} row of the wind farm has N_i turbines, each of them being driven by the same wind speed $v_{r,i}$. The speed from one row to another will, however, vary because of wake effects. Let p_i be the fraction of power expected to be generated by the i^{th} row. The controller design problem can then be stated for each individual turbine as

$$\min_{\mathcal{S}_j} \int_{\omega_1}^{\omega_2} \left[\log(P_{g,j}(\omega, \mathcal{S}_j)) - \log\left(\frac{p_i}{N_i} P_g(\omega)\right) \right]^2 d\omega. \quad (3.26)$$

where, j refers to a turbine index in the i^{th} row ($i = 1, \dots, N$), and $P_{g,j}(\omega_j, \mathcal{S}_j)$ is the closed-loop frequency response of the magnitude of the output power produced by the j^{th} turbine. Since every turbine in the i^{th} row tracks the same reference $\frac{p_i}{N_i} P_g(\omega)$, (3.26) can be solved for one turbine in each row. This decentralized approach not only saves computation time (since we now solve N parallel optimization problems with 5 decision variables rather than 1 optimization with $5N$ variables), but is also consistent with the power output pattern seen across the rows in a typical wind farm.

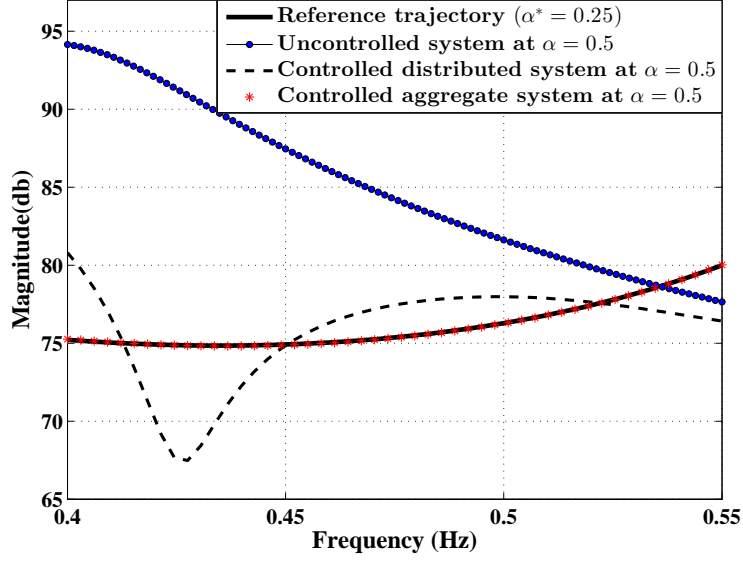


Figure 3.6: Comparison of spectral matching between the aggregate versus disaggregated wind farm model

3.2.3 Simulation Results

Here we illustrate the control designs proposed in subsections 3.2.1 and 3.2.2 for a wind and BES integrated power system using parameters mentioned previously. The power and the energy ratings of the battery are 1 MW and 40 MWh.

Figure 2.3 shows the spectra the wind-integrated power systems with no BES for four different values of α . This figure illustrates that as the wind power injection site is varied from $\alpha = 0$ to 1 the spectrum shows notable changes in both its period and the frequencies corresponding to the associated peaks and troughs. The variation in frequency response with wind injection location may make the damping at a particular wind injection site more desirable than others. For example, the spectrum for $\alpha = 0.5$ shows a peak at 0.4 Hz, while that for $\alpha = 0.25$ shows a trough that extends over 0.35 to 0.45 Hz. Since our goal is to damp the interarea modes, we select the spectrum associated with $\alpha = 0.25$ as the reference trajectory (which we denote as α^*), and design a controller for a wind farm located at $\alpha = 0.5$.

Controllers \mathcal{S}_1 and \mathcal{S}_2 for the wind farm and BES system are designed using the procedure described in section 3.2.1 for the frequency range [0.4, 0.55] Hz. The controller parameters are

obtained as,

$$\mathcal{S}_1 = \{0.6075, 0.8794, 1.2754, 1.6246, 1.3712\} \quad (3.27)$$

$$\mathcal{S}_2 = \{0.1207, 1.9472, 1.6284, 1.3772, 0.0062\} \quad (3.28)$$

Figure 3.6 shows that the closed-loop frequency response tracks the reference closely in the frequency range of interest. To test the efficiency of our control scheme for other frequency ranges, we also designed the controllers for those ranges assuming an aggregate wind turbine model. The spectral matching for each of these frequency ranges are found to be similar to that shown in Figure 3.6.

Next, we pursue the decentralized control approach described in section 3.2.2, and design individual wind farm controllers using (3.26). We consider a wind farm with 4 rows, each containing 5 turbines, as shown in Figure 3.7. The power production percentages for each row are assumed to be $p_1 = 36\%$, $p_2 = 22\%$, and $p_3 = p_4 = 21\%$. Turbines 3, 8, 13, and 18 are chosen as the representatives for their respective rows as they are centrally located, and, therefore, would have the least edge effects. The optimization problem (3.26) is solved for each of these four turbines, and the corresponding parameters for the controllers \mathcal{S}_{11} , \mathcal{S}_{12} , \mathcal{S}_{13} , and \mathcal{S}_{14} are listed in Table 3.3. Every other turbine in the i^{th} row is then controlled using \mathcal{S}_{1i} , $i = 1, 2, 3, 4$. Figure 3.6 shows that the closed-loop frequency response of the grid power flow resulting from controlling the 20-turbine wind farm and the BES at $\alpha = 0.5$ matches the reference fairly well over $[0.45, 0.5]$ Hz, but has a greater mismatch over $[0.4, 0.45]$ Hz. This can be explained by noting that the parameter optimization problem (3.26) minimizes the integral of the error function over the frequency range $[0.4, 0.55]$ rather than a point-to-point matching. For example, as can be seen in Figure 3.6, the undershoot in the range $f \in (0.42, 0.45]$ Hz is partially compensated by the overshoot when $f \in [0.45, 0.52]$ Hz and $f < 0.42$ Hz. A higher order controller or gain-scheduling may further improve the matching.

To validate our results in the time-domain, we construct $\delta(u, t) = \sum_{n=1}^{16} A_n(t) \cos(k_n u)$ at

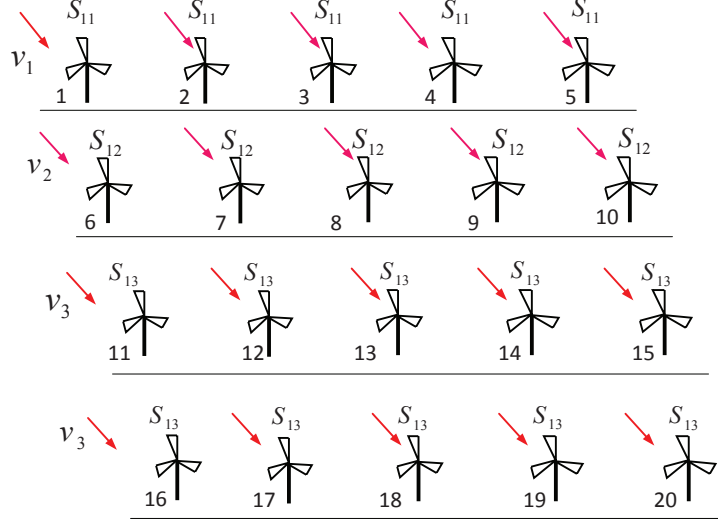


Figure 3.7: Arrangement of turbines in the wind farm.

| Row no. | Controller Parameters |
|---------|--|
| 1 | $\mathcal{S}_{11} = [0.042 \ 0.3016 \ 2.93e4 \ 6566 \ 4.77e6]$ |
| 2 | $\mathcal{S}_{16} = [8e-5 \ 0 \ 87.90 \ 53.14 \ 1128.0366]$ |
| 3, 4 | $\mathcal{S}_{1,11} = [0.0234 \ 8.6e-3 \ 236.23 \ 3005.76 \ 1.05e5]$ |

Table 3.3: Optimal controller parameters sets

$u = 0.25$ using the solution of (2.15) in both open-loop (with no wind farm or BES controller) and in closed-loop (when both wind farm and BES controller are implemented). The respective plots are shown in blue in the top and bottom panels of Figure 3.8. The open-loop response, when passed through a spectral analyzer, shows a dominant slow frequency of 0.9 Hz with a poor damping factor of 0.009. The closed-loop response, on the other hand, shows a dominant slow frequency of 0.86 Hz with a significantly higher damping factor of 0.04, indicating the effectiveness of the control. The impulse responses of the slow mode are shown in red in the respective panels in Figure 3.8.

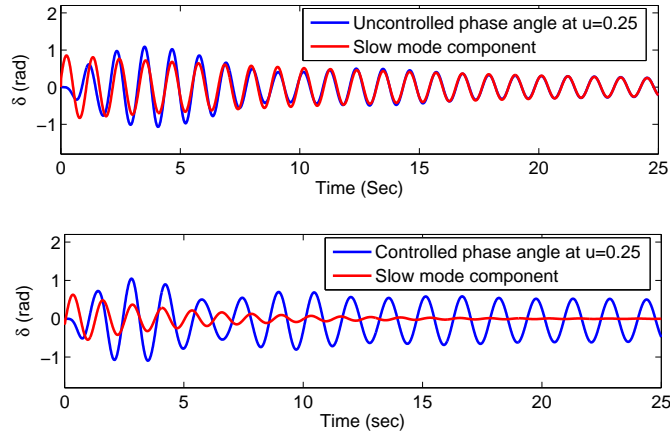


Figure 3.8: Open-loop versus closed-loop $\delta(t)$ at $u = 0.25$ with slow mode components

3.3 Conclusions

This Chapter demonstrates how closed-loop control of wind power generation and BES power consumption can be used for damping selected oscillation modes of a power system. We designed coordinated controllers for the wind farm and the BES, and showed how the controller parameters can be optimized to guarantee nearly perfect matching of the grid spectral response to a desired response. We also presented methods by which an aggregate control design can be distributed to individual turbines in a manner that captures important physical characteristics of the farm. In the next chapter we evaluate the impact of wind penetration on more detailed models of the power system described by ordinary differential equations (ODE) and their time scale separation.

Chapter 4

Time Scale Modeling of Power Systems with Wind Injections

Over the past few decades the operating characteristics of the North American power grid have changed substantially due to increasing penetration of renewable energy resources such as wind. These changes have led to a significant amount of research investigating the challenges associated with large-scale integration of wind energy [8, 9, 51]. The impact of increased levels of wind penetration on grid stability and dynamics [77], and in particular on inter-area oscillations, have also been the subject of a number of recent studies [25, 83, 91, 95]. Methods have been proposed to control these effects by regulating the wind farm power output [11, 79], and by controlling doubly fed induction generators (DFIGs) to increase oscillation damping [70, 95]. However, a detailed, rigorous analytical framework for evaluating the impact of wind penetration on power system oscillations has yet to be developed. Specifically, there is very limited understanding of how wind injection may affect the time-scale separation or *coherency* properties of conventional grid models [17].

Coherency arises from the partitioning of a power network into discrete generation areas, where each area consists of a group of strongly connected generators that synchronize over a fast time-scale and, thereafter, act as a single entity. The aggregates themselves are weakly connected

to each other, and synchronize over a slower time-scale. Using singular perturbation (SP) theory, [17] derived an analytical model describing such *fast* and *slow* motions for synchronous generators which depend on the relative norms of the network admittance matrices containing external and internal interconnections among generators. The approach in [17,18] was complimented by several related papers such as [29, 84, 99] through various model reduction techniques. Aggregation and coherency are still two of the most fundamental tools that are used to reduce the computational complexity of solving thousands of nonlinear equations in power system stability programs [82], and find wide applications to both small-signal and transient stability assessment [94].

In this Chapter we study how the conventional coherency model of a power system changes due to the addition of wind power. We first derive a mathematical model for the dynamics of a power network consisting of synchronous generators, loads, transmission lines and wind generator. The wind generator is modeled as a group of identical wind turbines electrically connected to the power grid at a point of common coupling via controlled DFIGs. We then aggregate the system into multiple coherent areas, and apply a linear transformation to represent the model in terms of slow and fast states. Using this transformed system we analytically show that the slow oscillatory modes of the power system can be affected by the wind plant depending on the wind penetration level and other power system parameters. Preliminary results on this topic have been recently reported in our conference paper [13]. Here we extend those results to include an explicit model showing the impact of wind penetration on the slow oscillatory modes of the power system [13]. Additionally in this chapter we develop detailed case studies illustrating the conditions when increasing wind penetration alter the slow oscillatory modes of the power system. In particular we explore case studies with different locations of the wind plant in the two-area, four-machine Kundur power system and the five-area, sixteen-machine interconnected power system of the New England (NETS) and New York power systems (NYPS).

The remainder of this work is organized as follows. Section 4.1 derives a small-signal model of the wind-integrated power system. Section 4.2 describes the time-scale separation of the wind-integrated power system. Section 4.3 presents simulation results. Concluding remarks are

provided in section 4.4.

4.1 Wind Integration Modeling

We consider a power system with the set of buses $\mathcal{N} = \{1, \dots, N\}$ and n generators where $n \leq N$. These generators consist of a set $\mathcal{G} = \{1, \dots, n-1\}$ of synchronous generators and one wind power plant. Without loss of generality we can reorder the buses so that the i^{th} synchronous generator is always connected to the i^{th} bus and the wind generator is connected to the n^{th} bus. To understand the coherency properties for this system, we first derive its small-signal electro-mechanical dynamic model considering both swing dynamics of the synchronous machines and the dynamics of the wind power plant.

4.1.1 Synchronous Generator Model

We model the dynamics of each generator $i \in \mathcal{G}$ based on [43] as,

$$\dot{\delta}_i = \omega_i \quad (4.1a)$$

$$m_i \dot{\omega}_i = P_{mi} - \frac{E_i}{x_{di}} (V_{iRe} \sin \delta_i - V_{iIm} \cos \delta_i). \quad (4.1b)$$

Here δ_i , ω_i , m_i , E_i , x'_{di} and P_{mi} are respectively the phase angle, machine speed, inertia, internal machine voltage, direct-axis salient reactance and the mechanical power input to generator $i \in \mathcal{G}$, and $V_i = V_{iRe} + jV_{iIm}$ is the voltage at bus $i \in \mathcal{G}$. Linearizing (4.1) about an operating point $(\delta_i^0, \omega_i^0, V_{iRe}^0, V_{iIm}^0, P_{mi}^0)$ for every $i \in \mathcal{G}$, the overall small-signal model can be written as

$$\Delta \dot{\delta} = I \Delta \omega \quad (4.2a)$$

$$M \Delta \dot{\omega} = k_{11} \Delta \delta + k_{12} \Delta V + \Delta P_m \quad (4.2b)$$

where Δ indicates a small change of a variable. M is a diagonal matrix of the inertias $m_i \forall i \in \mathcal{G}$, I is the identity matrix, $\Delta \delta := [\Delta \delta_1, \dots, \Delta \delta_n]^T$, $\Delta \omega := [\Delta \omega_1, \dots, \Delta \omega_n]^T$, $\Delta P_m :=$

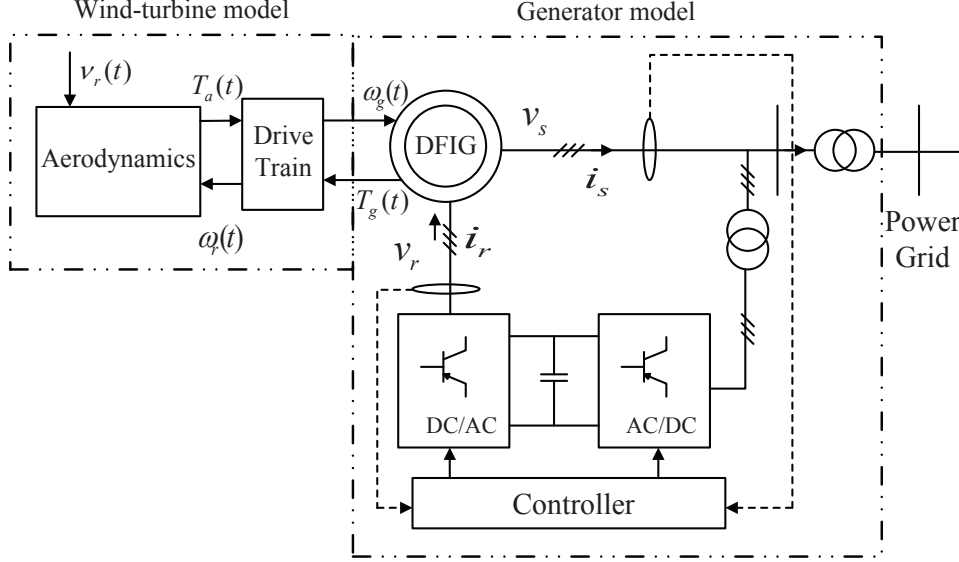


Figure 4.1: Wind turbine interfaced to the grid via a DFIG

$[\Delta P_{m1}, \dots, \Delta P_{mn}]^T$, and $\Delta V := [\Delta V_{1Re}, \dots, \Delta V_{nRe}, \Delta V_{1Im}, \dots, \Delta V_{nIm}]^T$. The active and reactive power outputs of the i^{th} generator are

$$P_{esi} = \frac{E_i}{x_{di}'} (V_{iRe} \sin \delta_i - V_{iIm} \cos \delta_i) \quad (4.3a)$$

$$Q_{esi} = \frac{E_i^2}{x_{di}'} - \frac{E_i}{x_{di}'} (V_{iRe} \cos \delta_i - V_{iIm} \sin \delta_i). \quad (4.3b)$$

The corresponding linearized power outputs can be written as

$$\Delta P_{es} = -k_{11} \Delta \delta - k_{12} \Delta V, \quad (4.4a)$$

$$\Delta Q_{es} = -k_{21} \Delta \delta - k_{22} \Delta V. \quad (4.4b)$$

Here, k_{11} , k_{12} , k_{21} and k_{22} are Jacobian matrices that are functions of the generator parameters and the initial bus voltages.

4.1.2 Wind Power Plant Model

For convenience of analysis, we consider an aggregate wind turbine model to represent the wind power plant. This model is obtained by first deriving the dynamic model of an individual wind generator. As in standard literature we consider each turbine to be identical [?] and therefore employ an aggregate transfer function based on one representative turbine. The power output of the wind power plant is then obtained by summing the power output of the individual turbines.

The individual wind generator model has a mechanical and an electrical subsystem as shown in Figure 4.1. The mechanical subsystem of the turbine consists of a two-shaft drive train connecting its rotor to a DFIG [92]. The rotor and the generator, which have respective inertias J_r and J_g , and friction coefficients B_r and B_g , are connected through a transmission gear with a gear ratio N_g , a torsion stiffness K_{dt} , and damping factor B_{dt} . The turbine model can be expressed in terms of the rotor speed $\omega_r(t)$, the generator speed $\omega_g(t)$ and the generator torsion angle $\theta_T(t)$ as [92],

$$J_r \dot{\omega}_r(t) = \frac{B_{dt}}{N_g} \omega_g(t) - K_{dt} \theta_T(t) - (B_{dt} + B_r) \omega_r(t) + T_a(t) \quad (4.5a)$$

$$J_g \dot{\omega}_g(t) = \frac{B_{dt}}{N_g} \omega_r(t) + \frac{K_{dt}}{N_g} \theta_T(t) - \left(\frac{B_{dt}}{N_g^2} + B_g \right) \omega_g(t) - T_g(t) \quad (4.5b)$$

$$\dot{\theta}_T(t) = \omega_r(t) - \frac{1}{N_g} \omega_g(t), \quad (4.5c)$$

where $T_a(t) = \frac{\rho A_s \nu_r^3(t) C_p(t)}{2 \omega_r(t)}$ is the aerodynamic torque input based on a turbine with swept area A_s , power coefficient $C_p(t)$, air density ρ and a wind speed of $\nu_r(t)$. The power coefficient $C_p(t)$ and the rotor speed $\omega_r(t)$ are obtained from a maximum power point tracking algorithm based on wind speed. $T_g(t)$ is the torque generated by the electrical subsystem, whose description follows. The electrical subsystem is comprised of a DFIG, which is modeled through the dynamics of its stator and rotor variables, expressed in a rotating $d - q$ reference frame as [96]

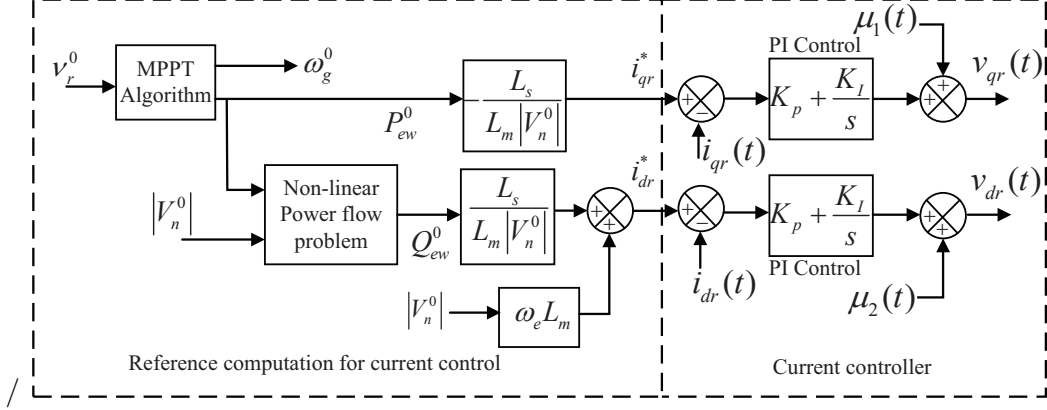


Figure 4.2: Decoupled active and reactive power control of a DFIG integrating a wind generator via the rotor-side controller

$$v_{qs}(t) = (R_s + \mathcal{D}L_s) i_{qs}(t) + \omega_e L_s i_{ds}(t) + \mathcal{D}L_m i_{qr}(t) + \omega_e L_m i_{dr}(t) \quad (4.6a)$$

$$v_{ds}(t) = -\omega_e L_s i_{qs}(t) + (R_s + \mathcal{D}L_s) i_{ds}(t) - \omega_e L_m i_{qr}(t) + \mathcal{D}L_m i_{dr}(t) \quad (4.6b)$$

$$v_{qr}(t) = \mathcal{D}L_m i_{qs}(t) + (\omega_e - \omega_{ge}) L_m i_{ds}(t) + (R_r + \mathcal{D}L_r) i_{qr}(t) + (\omega_e - \omega_{ge}) L_r i_{dr}(t) \quad (4.6c)$$

$$v_{dr}(t) = -(\omega_e - \omega_{ge}) L_m i_{qs}(t) + \mathcal{D}L_m i_{ds}(t) - (\omega_e - \omega_{ge}) L_r i_{qr}(t) + (R_r + \mathcal{D}L_r) i_{dr}(t), \quad (4.6d)$$

where $\omega_{ge} := \frac{p}{2} \omega_g$ is the electrical speed, p is the number of electrical poles of the DFIG, and \mathcal{D} is the differential operator. The subscripts d and q refer to the direct and quadrature axes of the reference frame rotating at constant speed ω_e . Subscripts s and r respectively indicate quantities associated with the stator and rotor circuits. The symbols v , i , and R respectively denote voltage, current, and resistance. L_{ls} , L_{lr} , L_m are respectively the stator and rotor leakage inductances and the magnetizing inductance. The stator and rotor inductance are respectively shown as $L_s = L_{ls} + L_m$ and $L_r = L_{lr} + L_m$. The electromagnetic torque provided to the shaft by the DFIG, which serves as the input in (4.5b) is given by

$$T_g(t) = \frac{p}{2} L_m [i_{qs}(t) i_{dr}(t) - i_{ds}(t) i_{qr}(t)]. \quad (4.7)$$

Both $v_{qr}(t)$ and $v_{dr}(t)$ are controllable quantities and can be designed via state feedback for

ensuring stable operation of the DFIG. We next describe this design briefly.

The active power output of the wind generator P_{ew}^0 , is obtained from the maximum power point tracking and the reactive power in equilibrium denoted as Q_{ew}^0 comes from the power flow solution. The active and reactive power output of a DFIG is a sum of the active and reactive powers of both the stator and the rotor. The ratio of the rotor power to the stator power is equal to the slip of the machine which is usually very small. So in this modeling we neglect the rotor power of the DFIG and consider the active and reactive power output at the wind bus to be equal to that of the stator as shown below,

$$P_{ew}(t) = v_{qs}(t)i_{qs}(t) + v_{ds}(t)i_{ds}(t) \quad (4.8a)$$

$$Q_{ew}(t) = v_{ds}(t)i_{qs}(t) - v_{qs}(t)i_{ds}(t). \quad (4.8b)$$

$P_{ew}(t)$ and $Q_{ew}(t)$ in a DFIG are usually controlled in a decoupled form by the rotor side converter, using $v_{qr}(t)$ and $v_{dr}(t)$ respectively [22] as shown in figure 4.2. Assuming w_e to be the synchronous frequency, d and q axis stator voltages can be shown as,

$$v_{qs}(t) = |V_n(t)| \quad v_{ds} = 0. \quad (4.9)$$

We consider the n^{th} bus to be the wind bus and model it as a PV bus with equilibrium voltage $|V_n^0|$. This allows us to control the active and reactive power output of the stator by i_{qs} and i_{ds} respectively. Assuming the stator flux to develop instantaneously in equilibrium, the q and d axis stator flux relations can be used to derive the following decoupled relations between stator and rotor currents,

$$i_{qr}^0 = -\frac{L_s}{L_m}i_{qs}^0 \quad i_{dr}^0 = -\frac{L_s}{L_m}i_{ds}^0 + \frac{|V_n^0|}{w_e L_m}. \quad (4.10)$$

The details of the design is shown in [22]. Using these relations the following two references can be computed;

$$i_{qr}^* = -\frac{L_s}{L_m} \left(\frac{P_{ew}^0}{|V_n^0|} \right) \quad i_{dr}^* = \frac{L_s}{L_m} \left(\frac{Q_{ew}^0}{|V_n^0|} \right) + \frac{|V_n^0|}{w_e L_m}. \quad (4.11)$$

Finally the design of $v_{qr}(t)$ and $v_{dr}(t)$ follows from (4.11) as,

$$v_{qr}(t) = K_p (i_{qr}^* - i_{qr}(t)) + K_I \int (i_{qr}^* - i_{qr}(t)) dt + \mu_1(t) \quad (4.12a)$$

$$v_{dr}(t) = K_p (i_{dr}^* - i_{dr}(t)) + K_I \int (i_{dr}^* - i_{dr}(t)) dt + \mu_2(t), \quad (4.12b)$$

where K_p and K_I are the respective proportional and integral gains. Equations (4.5)-(4.12) represent the nonlinear state-variable model of any turbine j where $j \in \{1, 2, \dots, \gamma\}$, and γ is the number of turbines. Note that with a slight abuse of notation we have dropped the notation j in (4.5)-(4.12) since we assume every generator to have identical parameters [?]. Since the current control is executed over a much faster time-scale than the states in (4.6) we ignore the controller states and derive the linearized model for the j^{th} wind generator about a constant operating point. $(\omega_{rj}^0, \omega_{gj}^0, \theta_{Tj}^0, i_{qsj}^0, i_{dsj}^0, i_{qrj}^0, i_{drj}^0)$, leading to,

$$\Delta \dot{\mathcal{Z}}_j = A \Delta \mathcal{Z}_j + B_1 |\Delta V_n|, \quad (4.13)$$

where A and B_1 are the state and input matrices. The corresponding state variables are given by,

$$\Delta \mathcal{Z}_j := \left[\Delta \omega_{rj} \quad \Delta \omega_{gj} \quad \Delta \theta_{Tj} \quad \Delta i_{qsj} \quad \Delta i_{ds} \quad \Delta i_{qrj} \quad \Delta i_{drj} \right]^T.$$

A and B_1 in (4.13) are independent of j as we assume each turbine to have an identical model. Defining aggregate state as $\dot{Z} = \frac{1}{\gamma} \sum_{j=1}^{\gamma} \Delta \mathcal{Z}_j$, the state-space model of the wind power plant can be written as,

$$\Delta \dot{Z} = A \Delta Z + B_1 |\Delta V_n|, \quad (4.14)$$

with the corresponding linearized power outputs as

$$\begin{bmatrix} \Delta P_{ew} \\ \Delta Q_{ew} \end{bmatrix} = \begin{bmatrix} C_1 \Delta Z \\ C_2 \Delta Z \end{bmatrix} + \begin{bmatrix} D_1 |\Delta V_n| \\ D_2 |\Delta V_n| \end{bmatrix}, \quad (4.15)$$

where $D_1 := \gamma i_{qs}^0$, $D_2 := -\gamma i_{ds}^0$, $C_1 := \gamma [0 \ 0 \ 0 \ v_{qs}^0 \ 0; \ 0 \ 0]$, and $C_2 := \gamma [0 \ 0 \ 0 \ 0 \ -v_{qs}^0 \ 0 \ 0]$.

Note that the total power output of the plant is the sum of the individual power outputs of the turbines, as a result of which γ appears as a multiplying constant in the output matrices in the RHS of (4.15). We next connect the swing dynamics in (4.2) with the wind power dynamics in (4.5) through the common power flow equations in (4.4) and (4.15).

4.1.3 Wind Integrated Power System Model

The active and reactive power flow balance at any bus $j \in \mathcal{N}$, at any time t can be written as [18]

$$0 = P_{ej} - \operatorname{Re} \left\{ \sum_{k=1, k \neq j}^N V_{jk} (V_j B_{jk})^* \right\} - V_j^2 G_j \quad (4.16a)$$

$$0 = Q_{ej} - \operatorname{Im} \left\{ \sum_{k=1, k \neq j}^N V_{jk} (V_j B_{jk})^* \right\} - V_j^2 B_j. \quad (4.16b)$$

Here, P_{ej} and Q_{ej} respectively denote active and reactive power generation. For each bus $j \in \mathcal{G}$, these terms correspond to contributions from the synchronous generators, while they correspond to the wind power generation when j is the wind bus. For every bus $j \in \mathcal{N}$, G_j and B_j are respectively the load conductance and load susceptance with line charging. We assume the lines to be lossless, and denote the susceptance of the line connecting buses j and k as B_{jk} . The quantity V_{jk} , by definition, is the difference in the voltage phasors between bus j and k , i.e., $V_{jk} := (V_{jRe} - V_{kRe}) + j(V_{jIm} - V_{kIm})$. The linearized power flows corresponding to (4.16) are

$$\begin{aligned} \Delta P_{ej} = & \sum_{k=1, k \neq j}^N \left(\frac{c_1 \Delta V_{jRe} + c_2 \Delta V_{kIm} + c_3 \Delta V_{kRe} + c_4 \Delta V_{jIm}}{(1/B_{jk})} \right) \\ & + 2 (V_{jRe}^0 \Delta V_{jRe} + V_{jIm}^0 \Delta V_{jIm}) G_j \end{aligned} \quad (4.17a)$$

$$\begin{aligned} \Delta Q_{ej} = & \sum_{k=1, k \neq j}^N \left(\frac{c_5 \Delta V_{jRe} + c_6 \Delta V_{kIm} + c_7 \Delta V_{kRe} + c_8 \Delta V_{jIm}}{(1/B_{jk})} \right) \\ & + 2 (V_{jRe}^0 \Delta V_{jRe} + V_{jIm}^0 \Delta V_{jIm}) B_j, \end{aligned} \quad (4.17b)$$

where $c_1 := -V_{k_{Im}}^0$, $c_2 := -V_{j_{Re}}^0$, $c_3 := V_{j_{Im}}^0$, $c_4 := V_{k_{Re}}^0$, $c_5 := (2V_{j_{Re}}^0 - V_{k_{Re}}^0)$, $c_6 := -V_{j_{Im}}^0$, $c_7 := -V_{j_{Re}}^0$ and $c_8 := (2V_{j_{Im}}^0 - V_{k_{Im}}^0)$.

At the synchronous generator buses $j \in \mathcal{G}$, the small-signal power flows obtained from (4.16) are $\Delta P_{ej} = \Delta P_{esj} = k_2 \Delta V$ and $\Delta Q_{ej} = \Delta Q_{esj} = k_4 \Delta V$, where k_2 is a $n \times 2N$ matrix whose elements are given by

$$\begin{aligned} k_2(j, j) &= - \sum_{k=1, k \neq j}^N V_{k_{Im}}^0 B_{jk} + 2V_{j_{Re}}^0 G_j, \\ k_2(j, k) &= V_{j_{Im}}^0 B_{jk}, \quad k_2(j, N+k) = -V_{j_{Re}}^0 B_{jk}, \\ k_2(j, N+j) &= \sum_{k=1, k \neq j}^N V_{k_{Re}}^0 B_{jk} + V_{j_{Im}}^0 G_j. \end{aligned}$$

The matrix k_4 also has dimension $n \times 2N$ with elements

$$\begin{aligned} k_4(j, j) &= \sum_{k=1, k \neq j}^N (2V_{j_{Re}}^0 - V_{k_{Re}}^0) B_{jk} + 2V_{j_{Re}}^0 B_j \\ k_4(j, k) &= -V_{j_{Re}}^0 B_{jk}, \quad k_4(j, N+k) = -V_{j_{Im}}^0 B_{jk}, \\ k_4(j, N+j) &= \sum_{k=1, k \neq j}^N (2V_{j_{Im}}^0 - V_{k_{Im}}^0) B_{jk} + V_{j_{Im}}^0 B_j. \end{aligned}$$

Combining these expressions with (4.4) yields

$$0 = -k_{11} \Delta \delta - (k_2 + k_{12}) \Delta V \quad (4.18a)$$

$$0 = -k_{21} \Delta \delta - (k_4 + k_{22}) \Delta V. \quad (4.18b)$$

The stator of the DFIG is directly connected to the wind generator bus n . The linearized power flow of the wind bus in (4.15) can, hence, be rewritten as

$$0 = C_1 \Delta Z + (D_{1n} + k_5) \Delta V \quad (4.19a)$$

$$0 = C_2 \Delta Z + (D_{2n} + k_6) \Delta V \quad (4.19b)$$

where $D_{1n}\Delta V = D_1 |\Delta V_n|$, $D_{2n}\Delta V = D_2 |\Delta V_n|$, and k_5 and k_6 respectively share the structure of k_2 and k_4 described above. The power flow at buses with no generators are

$$k_7\Delta V = 0 \quad k_8\Delta V = 0 \quad (4.20)$$

where k_7 and k_8 respectively share the structure of k_2 and k_4 . Combining (4.18)-(4.20) the power flow for the overall small-signal model is given by

$$0 = A_1\Delta\delta + A_2\Delta Z + A_4\Delta V \quad (4.21)$$

where $A_1 = [k_{11} \ 0 \ 0 \ k_{21} \ 0 \ 0]^T$, $A_2 = [0 \ C_1 \ 0 \ 0 \ C_2 \ 0]^T$,
 $A_4 = [(k_2 + k_{12}) \ (D_{1n} + k_5) \ k_7 \ (k_4 + k_{22}) \ (D_{2n} + k_6) \ k_8]^T$.

Note that A_4 is a weighted admittance matrix of the network. Finally, we combine (4.2), (4.14) and (4.21) to obtain the following Kron-reduced model of the wind-integrated power system:

$$\begin{bmatrix} M\Delta\ddot{\delta} \\ \Delta\dot{Z} \end{bmatrix} = A_M \begin{bmatrix} \Delta\delta \\ \Delta Z \end{bmatrix} + B_M\Delta P_m \quad (4.22)$$

where $A_M = \begin{bmatrix} A_{M11} & A_{M12} \\ A_{M21} & A_{M22} \end{bmatrix}$, $B_M = \begin{bmatrix} I & 0 \end{bmatrix}$,
 $A_{M11} := (k_{11} - k_{12}A_4^{-1}A_1)$, $A_{M12} := -k_{12}A_4^{-1}A_2$, $A_{M21} := -B_1A_4^{-1}A_1$ and
 $A_{M22} := (A - B_1A_4^{-1}A_2)$.

4.2 Time-scale Modeling

In this section we investigate the time-scale separation properties of the wind-integrated power system model (4.22). We first aggregate the network into a set $\mathcal{R} := \{1, \dots, r\}$ of coherent areas, where $r - 1$ of these areas contain only synchronous generators. The remaining area has a mix of synchronous generators and a wind plant. We denote the parameters associated with

Area α using a superscript α . $\Delta\delta_i^\alpha$ denotes the small-signal phase angle of the i^{th} synchronous generator in Area α . For ease of exposition, we reorder the states so that for each Area $\alpha \in \mathcal{R}$, the $\Delta\delta_i^\alpha$'s appear consecutively in the state vector $\Delta\delta$. Quantities related to the connections between generators inside an area are indicated with the superscript I , while those capturing the connections between different areas are denoted using the superscript E .

4.2.1 Power System Time-constants

As in [17] we assume that the power system model in (4.22) satisfies the following two properties.

1. *Property 1:* For any Area $\alpha \in \mathcal{R}$, the ratio of the maximum susceptance corresponding to its external connections $B_{ij,(max)}^E$ of its generators is lower than the ratio of the minimum susceptance of its internal connections $B_{ij,(min)}^I$. This property is characterized by defining the small parameter $\varepsilon_1 = \frac{B_{ij,(max)}^E}{B_{ij,(min)}^I} > 0$, which will lead to the slower synchronization between generators in different areas.
2. *Property 2:* A given area $\alpha \in \mathcal{R}$ has many more internal connections than external connections. This property can be quantified by a small positive parameter $\varepsilon_2 := \frac{\bar{\kappa}^E}{\bar{\kappa}^I} > 0$, where $\bar{\kappa}^E := \max_{\alpha} \{\kappa^{E,\alpha}\}$, $\bar{\kappa}^I := \min_{\alpha} \{\kappa^{I,\alpha}\}$. Here, the ratios of the number of external and internal connections in Area α to the number of buses in that area are respectively denoted as $\kappa^{E,\alpha}$ and $\kappa^{I,\alpha}$, respectively.

If the bus voltages of the power system network are given, the time-scales of the system can be specified by first partitioning A_4 in (4.21) as

$$A_4 = A_4^I + \varepsilon A_4^E, \quad (4.23)$$

where A_4^I and A_4^E respectively contain the elements of A_4 associated with the internal and external connections, and ε is a dimensionless constant defined as

$$\varepsilon := \varepsilon_1 \varepsilon_2. \quad (4.24)$$

The matrix A_{M11} in (4.22) can also be separated as,

$$A_{M11} = A_{M11}^I + \varepsilon A_{M11}^E, \quad (4.25)$$

where $A_{M11}^I = k_{11} - k_{12}(A_4^I)^{-1}A_1$ and $A_{M11}^E = -k_{12} \left(-(A_4^I)^{-1}A_4^E + \varepsilon \left((A_4^I)^{-1}A_4^E \right)^2 + \dots \right) (A_4^I)^{-1}A_1$. The matrix A_4^I can be further decomposed as $A_4^I = A_4^{I,sg} + A_4^{I,wg0}$, where $A_4^{I,sg}$ models the contribution of the internal connection of the synchronous generators in A_4^I while $A_4^{I,wg0} := [0 \ D_{1n} \ 0 \ 0 \ D_{2n} \ 0]^T$ models the contribution of the wind plant [11]. The norms $\|A_4^{I,sg}\|$ and $\|A_4^{I,wg0}\|$ are, however, generally not of the same order for typical wind penetration limit. To mitigate this effect we introduce the dimensionless scaling factor

$$\varepsilon_w := \frac{|i_{smax}|}{|B_{ij,(min)}^I \bar{K}^I|}, \quad (4.26)$$

where i_{smax} is the maximum stator current of the wind plant. As the number of wind turbines γ is increased, the collective current $|i_{smax}|$ at the point of common coupling of the wind plant increases and so does ε_w . We then write

$$A_4^I = A_4^{I,sg} + \varepsilon_w A_4^{I,wg}, \quad (4.27)$$

where, $A_4^{I,wg} := [0 \ D'_1 \ 0 \ 0 \ D'_2 \ 0]^T$ with $D'_1 := D_{1n}/\varepsilon_w$ and $D'_2 := D_{2n}/\varepsilon_w$. The form of ε_w along with the definitions of D_{1n} and D_{2n} in (4.19a) and (4.19b) respectively ensure that the $\|A_4^{I,sg}\|$ and $\|A_4^{I,wg}\|$ are the same order of magnitude. We will next show that ε and ε_w together model the slow and fast time-scales of (4.22) if properties 1 and 2 hold.

Remark 1 *The construction above can be easily generalized to ℓ wind power plants in ℓ different areas. In that case, one would first construct ℓ constants $\varepsilon_w^1, \varepsilon_w^2, \dots, \varepsilon_w^\ell$ for the individual wind plants following (4.26), and then define the constant ε_w as the maximum of these ℓ constants.*

4.2.2 Time-scale Separation

Following [17] we define the slow variables for the areas $\alpha \in \{1, 2, \dots, r-1\}$ as

$$\delta_{s_{sg}}^\alpha := \sum_{i=1}^{n^\alpha} m_i^\alpha \Delta \delta_i^\alpha / \sum_{i=1}^{n^\alpha} m_i^\alpha \quad (4.28)$$

where n^α is the number of synchronous machines in Area α , and m_i^α is the inertia of the i^{th} generator in that area. The subscript s_{sg} on the LHS of (4.28) denotes the slow variable for any area that contains only synchronous generators. Similarly, the slow variable for Area r is defined only in terms of the angles of the synchronous generators in that area, i.e.,

$$\delta_{s_{wg}}^r := \sum_{i=1}^{n^r-1} m_i^r \Delta \delta_i^r / \sum_{i=1}^{n^r-1} m_i^r \quad (4.29)$$

where n^r is the total number of synchronous and wind generators in Area r . The subscript s_{wg} on the LHS of (4.29) denotes the slow variable for the area with wind power generation. The expressions in (4.28) and (4.29) can be combined as

$$\begin{bmatrix} \delta_{s,sg} \\ \delta_{s,wg} \end{bmatrix} = M_a^{-1} U^T M \Delta \delta \quad (4.30)$$

where $M_a := U^T M U$ is a diagonal matrix of aggregate inertias, and $U := \text{blockdiag}(u^1, u^2, \dots, u^r)$, where each $u^\alpha := \mathbf{1} \in \mathbb{R}^{(n^\alpha) \times 1}$.

Similarly, the fast dynamics of the synchronous generators in Area α [17] are defined as

$$\delta_{f,i-1}^\alpha := \Delta \delta_i^\alpha - \Delta \delta_1^\alpha, \quad i = 2, 3, \dots, n^\alpha - n^{w\alpha}, \quad (4.31)$$

where $n^{w\alpha} = 0$ for $\alpha \in \{1, 2, \dots, r-1\}$, $n^{w\alpha} = 1$ for $\alpha = r$, and $\Delta \delta_1^\alpha$ is the angle of a reference generator. Without loss of generality, we assign the first generator in each area to be the

reference generator. The fast variables can be combined into

$$\delta_f = G\Delta\delta = \text{blockdiag}(G^1, G^2, \dots, G^r) \Delta\delta \quad (4.32)$$

where

$$G^\alpha := \begin{bmatrix} -1 & 1 & 0 & \dots & 0 \\ -1 & 0 & 1 & \dots & 0 \\ \dots & \dots & \dots & \dots & \dots \\ -1 & 0 & 0 & \dots & 1 \end{bmatrix}_{n_\alpha-1 \times n_\alpha} \quad (4.33)$$

Applying the similarity transformation in (4.30) and (4.32), the time-scale separated form of (4.22) is given by

$$\begin{bmatrix} M_{a,sg} \ddot{\delta}_{s,sg} \\ M_{a,wg} \ddot{\delta}_{s,wg} \\ M_d \ddot{\delta}_f \\ \Delta \dot{Z} \end{bmatrix} = \tilde{A} \begin{bmatrix} \delta_{s,sg} \\ \delta_{s,wg} \\ \delta_f \\ \Delta Z \end{bmatrix} + \tilde{B}_M \Delta P_m, \quad (4.34)$$

where $M_{a,sg} \in \mathbb{R}^{(r-1) \times (r-1)}$ is a diagonal matrix of the first $r-1$ diagonal elements of M_a , $M_{a,wg} \in \mathbb{R}$ is the r^{th} diagonal element of M_a , and

$$\tilde{A} := \begin{bmatrix} \varepsilon K_{aa_{sg}} & \varepsilon K_{aa_{swg}} & \varepsilon K_{ad_{sg}} & \varepsilon K_{ab_{sg}} \\ \varepsilon_w K_{aa_{wsg}} & \varepsilon_w K_{aa_{wsg}} & \varepsilon_w K_{ad_{wsg}} & \varepsilon_w K_{ab_{wsg}} \\ \varepsilon K_{da_{sg}} & \varepsilon K_{da_{wsg}} & K_d & K_{db} \\ K_{ba_{sg}} & K_{ba_{wsg}} & K_{bd} & K_{bb} \end{bmatrix}.$$

Algorithm 1 describes the procedure for constructing the matrices \tilde{A} and \tilde{B}_M .

Algorithm 1 Construct \tilde{A} and \tilde{B}_M

Construct $G^+ := G^T(GG^T)^{-1}$, where G is defined in (4.32)

Construct $M_d := (GM^{-1}G^+)^{-1}$, where M is defined in (4.2)

Construct $K_{db} := M_dGM^{-1}A_{M12}$, $K_{bd} := A_{M21}G^+$ and $K_{bb} := A_{M22}$ using A_{M12} , A_{M21} and A_{M22} , defined in (4.22)

Construct $K_d = M_dGM^{-1}A_{M11}^I G^+ + \varepsilon M_dGM^{-1}A_{M11}^E G^+$ using A_{M11}^I , A_{M11}^E as defined in (4.25), and ε defined in (4.24)

Construct the submatrices of \tilde{A} as

$$\begin{aligned} \begin{bmatrix} K_{aa_{sg}} & K_{aa_{swg}} \\ (\varepsilon_w/\varepsilon) K_{aa_{wsg}} & (\varepsilon_w/\varepsilon) K_{aa_{wsg}} \end{bmatrix} &:= U^T A_{M11}^E U, \\ \begin{bmatrix} K_{ad_{sg}} & (\varepsilon_w/\varepsilon) K_{ad_{wsg}} \end{bmatrix}^T &:= U^T A_{M11}^E M^{-1} G^T M_d, \\ \begin{bmatrix} \varepsilon K_{ab_{sg}} & \varepsilon_w K_{ab_{wsg}} \end{bmatrix}^T &:= U^T A_{M12}, \\ \begin{bmatrix} K_{da_{sg}} & (\varepsilon_w/\varepsilon) K_{da_{wsg}} \end{bmatrix} &:= M_d G M^{-1} A_{M11}^E U, \\ \begin{bmatrix} K_{ba_{sg}} & K_{ba_{wsg}} \end{bmatrix} &:= A_{M21} U \end{aligned}$$

using ε_w as defined in (4.26).

Construct \tilde{B}_M from B_M using the similarity transforms (4.30) and (4.32).

4.2.3 The Effect of Wind Injection on Time-scales

In order to understand how the wind power plant affects the time-scales, we further transform (4.34) based on the slowest time-scale. Typically for 15 – 20% wind power penetration, ε_w in (4.26) is smaller than ε in (4.24) because at this level of wind penetration external admittance $B_{ij}^{E,min}$ is larger in magnitude than that of the current i_{smax} injected into the system by the wind plant. This fact leads us to transform (4.34) into the slowest time-scale with the substitution $t_s = \sqrt{\varepsilon_w} t$ and obtain,

$$\begin{bmatrix} M_{a,wg} \ddot{\delta}_{s,wg} \\ \frac{\varepsilon_w}{\varepsilon} M_{a,sg} \ddot{\delta}_{s,sg} \\ \varepsilon_w M_d \ddot{\delta}_f \\ \sqrt{\varepsilon_w} \Delta \dot{Z} \end{bmatrix} = \tilde{A}_1 \begin{bmatrix} \delta_{s,wg} \\ \delta_{s,sg} \\ \delta_f \\ \Delta Z \end{bmatrix} \quad (4.35)$$

$$\text{where } \tilde{A}_1 := \begin{bmatrix} K_{aa_{wg}} & K_{aa_{wsg}} & K_{ad_{wg}} & K_{ab_{wg}} \\ K_{aa_{swg}} & K_{aa_{sg}} & K_{ad_{sg}} & K_{ab_{sg}} \\ \varepsilon K_{da_{wg}} & \varepsilon K_{da_{sg}} & K_d & K_{db} \\ K_{ba_{wg}} & K_{ba_{sg}} & K_{bd} & K_{bb} \end{bmatrix}.$$

Here we have reordered $\delta_{s,wg}$ and $\delta_{s,sg}$ in the state matrix to arrange the states in ascending order of their time-scales. Since the relative norms of the inertia matrices $M_{a,wg}$, $M_{a,sg}$ and M_d are already consistent with the assumption of coherency the time-scale separation of (4.35) is completely characterized by the two constants ε and ε_w , which have typical values of .032 and .003 respectively for a system with 10% wind penetration. Since the time constants for δ_f and Z are smaller than those of $\delta_{s,wg}$ and $\delta_{s,sg}$, their effects decay quickly. We therefore assume that the dynamics of δ_f and Z to be in quasi-steady state, i.e., $\ddot{\delta}_f = \Delta \dot{Z} = 0$, and reduce the model to

$$\begin{bmatrix} M_{a,wg} \ddot{\delta}_{s,wg} \\ \frac{\varepsilon_w}{\varepsilon} M_{a,sg} \ddot{\delta}_{s,sg} \end{bmatrix} = \begin{bmatrix} \tilde{k}_{11} & \tilde{k}_{12} \\ \tilde{k}_{21} & \tilde{k}_{22} \end{bmatrix} \begin{bmatrix} \delta_{s,wg} \\ \delta_{s,sg} \end{bmatrix} \quad (4.36)$$

where,

$$\tilde{k}_{11} = K_{aa_{wg}} - \varepsilon K_{ad_{wg}} (K_d)^{-1} K_{da_{wg}} - K_{ab_{wg}} (K_{bb})^{-1} K_{ba_{wg}},$$

$$\tilde{k}_{12} = K_{aa_{wsg}} - \varepsilon K_{ad_{wg}} (K_d)^{-1} K_{da_{sg}} - K_{ab_{wg}} (K_{bb})^{-1} K_{ba_{sg}},$$

$$\tilde{k}_{21} = K_{aa_{swg}} - \varepsilon K_{ad_{sg}} (K_d)^{-1} K_{da_{wg}} - K_{ab_{sg}} (K_{bb})^{-1} K_{ba_{wg}},$$

$$\tilde{k}_{22} = K_{aa_{sg}} - \varepsilon K_{ad_{sg}} (K_d)^{-1} K_{da_{sg}} - K_{ab_{sg}} (K_{bb})^{-1} K_{ba_{sg}}.$$

Equation (4.34) shows the complete analytical form of the time-scale separation for the dynamics of a wind-integrated power system with wind injection in a single generation area. Equation (4.36) shows how the amount of wind power injection γ , affects the slow time-scale dynamics. Increasing γ by a factor of two or three from its base value will increase ε_w , but the

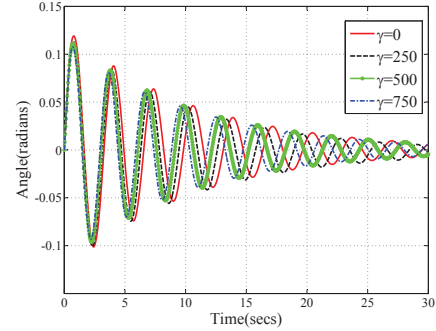
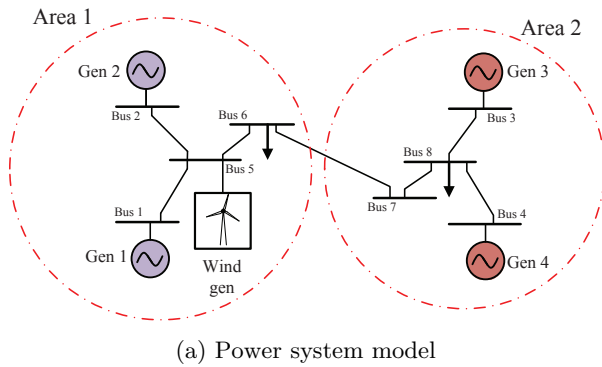


Figure 4.3: Kundur 8-bus, 4-machine, 2-area power system with wind injection at bus 5

ratio $\varepsilon_w/\varepsilon$ will still be significantly less than 1. A factor of 10 increase in γ does lead to a ratio close to one, which corresponds to a situation which is relevant for the current study because it corresponds to more than 90% wind penetration.

The most important implication of (34) is the dependence of the relative norms of the matrices \tilde{k}_{11} , \tilde{k}_{12} , \tilde{k}_{21} and \tilde{k}_{22} on the equilibrium values of the bus voltages. Changes in the locations of the synchronous machines, the wind generator and the loads affect the voltages of the buses and in turn changes the associated matrix norms which is reflected in the slow eigenvalues of the system in (4.36). In the next section we illustrate this behavior through two specific case studies.

4.3 Results

In this section we investigate the time-scale separation properties of the wind integrated power system via two power system models; an 8-bus, 4-machine, 2-area power system [43] and a 68-bus, 16-machine, 5-area power system [88], each integrated with one wind power plant. For each case we explore the effects of placing the wind power plant in different generation areas as the wind penetration level is varied. We vary the wind penetration level by adjusting the parameter γ , which is the number of wind turbines in the wind farm. We use γ to define a penetration level as the total wind power divided by the total load in the power system. For

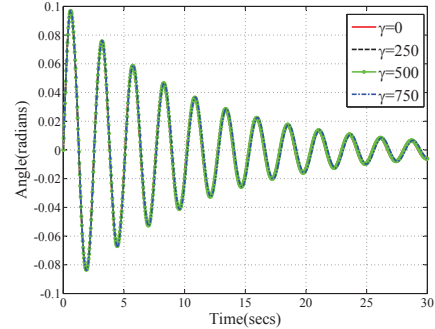
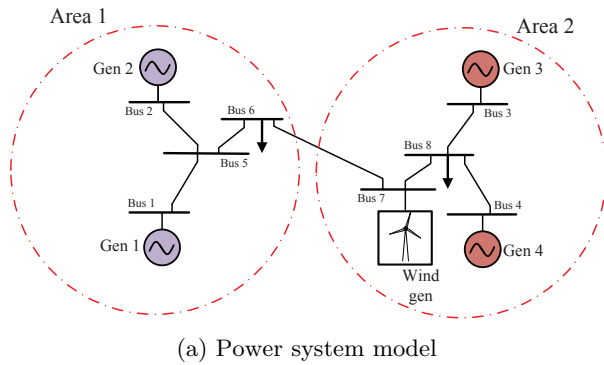


Figure 4.4: Kundur 8-bus, 4-machine, 2-area power system with wind injection at bus 7

each scenario we first solve a power flow program to compute the equilibrium values of the system state, and then compute the corresponding linearized model (4.22). We illustrate the slow time scales in terms of three system properties; (1) the infinity norms of the matrices $A_4^{I,sg}$, $A_4^{I,wg0}$ and A_4^E , which illustrate the ratio between ε and ε_w , (2) the slow eigenvalues of the power system model in (4.22), and (3) the impulse response of the aggregate angle difference between two generation areas as γ is varied, which shows the effect of γ on the slow oscillations. For all our simulations we consider the small-signal perturbation to be an impulse change in the mechanical input to synchronous generator 1, ΔP_{m1} in (4.1b).

4.3.1 2-area 8-bus Power System

We simulate the 8-bus, 4-machine, 2-area power system shown in for two different cases, one with wind injection at bus 5 in area 1 and another with wind injection at bus 7 in area 2 as shown in figures 4.3a and 4.4a respectively. The major load of the system is located at bus 8 in area 2. The parameters of the power system model are given in Appendix A.1 and the wind parameters are given in Appendix A.2. In order to investigate the time-scale separation of the wind-integrated power system in (4.36) over different values of γ we balance the overall generation and power flow in such a way that aggregate inertias of the respective generation areas are comparable. We also choose a synchronous generator close to the wind bus as the

| γ | $\ A_4^{I,sg}\ $ | $\ A_4^{I,wg0}\ $ | $\ A_4^E\ $ | Slow eigenvalue |
|----------|------------------|-------------------|-------------|-------------------|
| 0 | 3341 | 0.00 | 108.73 | $-0.10 \pm j1.90$ |
| 250 | 3362 | 4.79 | 108.93 | $-0.10 \pm j2.00$ |
| 500 | 3381 | 9.49 | 107.85 | $-0.10 \pm j2.10$ |
| 750 | 3411 | 14.08 | 109.05 | $-0.10 \pm j2.13$ |

(a) Wind injection in bus 5

| γ | $\ A_4^{I,sg}\ $ | $\ A_4^{I,wg0}\ $ | $\ A_4^E\ $ | Slow eigenvalue |
|----------|------------------|-------------------|-------------|-------------------|
| 0 | 3882 | 0.00 | 115.87 | $-0.10 \pm j2.47$ |
| 250 | 3892 | 4.87 | 116.24 | $-0.10 \pm j2.47$ |
| 500 | 3901 | 9.77 | 116.57 | $-0.10 \pm j2.46$ |
| 750 | 3910 | 14.72 | 116.64 | $-0.09 \pm j2.45$ |

(b) Wind injection in bus 7

Table 4.1: Matrix norms and slow eigenvalues for the 8-bus 4-machine 2-area power system.

slack generator in order to maintain the bus voltages as close as possible for different values of γ . For the two wind locations, γ is assumed to take values of 0 (the base case), 250, 500 and 750 which respectively correspond to wind penetrations of 0%, 5%, 10% and 15% for the total connected load in the system.

Wind injection at bus 5

In this scenario the wind power plant is connected to bus 5 in area 1 while the major load is connected to bus 8 in area 2, as shown in figure 4.3a. Bus 1 is treated as the slack bus. Table 4.1a shows that $\|A_4^E\|$ is considerably higher than $\|A_4^{I,wg0}\|$, so $\varepsilon_w/\varepsilon \ll 1$. As γ increases the power flow across the inter-area tie-line joining buses 6 and 7 also grows thereby increasing $\|A_4^E\|$. The higher value of the norm is reflected through a slightly higher frequency of the slow oscillatory modes, as seen in the imaginary parts of the slow eigenvalues in Table 4.1a. The impulse response of the aggregate angle difference ($\delta_{s,1} - \delta_{s,2}$) between area 1 and area 2, shown in figure 4.3b also confirms the faster oscillatory mode with increasing γ . Table 4.2 shows the fast eigenvalues of the system model for different γ . The entries indicate that the fast modes are practically unaffected by wind penetration.

Wind injection at bus 7

| γ | Wind at bus 5 | Wind at bus 7 |
|----------|--|--|
| 0 | $-0.21 \pm j8.99$ $-0.21 \pm j8.04$ | $-0.22 \pm j9.01$ $-0.21 \pm j7.58$ |
| 250 | $-0.21 \pm j8.97$ $-0.21 \pm j8.05$ | $-0.21 \pm j9.01$ $-0.22 \pm j7.61$ |
| 500 | $-0.21 \pm j8.96$ $-0.21 \pm j8.06$ | $-0.22 \pm j9.02$ $-0.21 \pm j7.63$ |
| 750 | $-0.22 \pm j8.94$ $-0.21 \pm j8.06$ | $-0.22 \pm j9.02$ $-0.21 \pm j7.68$ |

Table 4.2: Fast eigenvalues for the 8-bus 4-machine 2-area power system in different scenarios.

In this scenario both the wind power plant and the major load is in area 2, as shown in figure 4.4a. Bus 4 is considered to be the slack bus here. In this case $\|A_4^E\|$ also has a higher magnitude than $\|A_4^{I,wg0}\|$ as shown in Table 4.1b. However, in contrast to the previous case with increasing wind penetration the power flow along the inter-area tie line between bus 6 and bus 7 remains relatively unchanged, which is reflected in the relatively constant value of $\|A_4^E\|$. Correspondingly the slow oscillatory modes of the power system remain almost identical as shown in Table 4.1b. The impulse response of the aggregate angle difference $(\delta_{s,1} - \delta_{s,2})$ between area 1 and area 2, also remains relatively unchanged with increasing γ as shown in figure 4.4b. In this case also the change in the fast eigenvalues with increasing γ is minuscule, as shown in table 4.2.

4.3.2 5-area 68-bus Power System

In this subsection we simulate the 68-bus, 16-machine, 5-area power system shown in figure 4.5a. Again we investigate two representational scenarios. In scenario 1, the wind power plant is

| γ | $\ A_4^{I,sg}\ $ | $\ A_4^{I,wg0}\ $ | $\ A_4^E\ $ | Slow eigenvalues |
|----------|------------------|-------------------|-------------|--|
| 0 | 2373 | 0 | 161.56 | $-0.09 \pm j3.46, -0.06 \pm j2.92$ $-0.10 \pm j2.38, -0.08 \pm j1.55$ |
| 250 | 2380 | 5.60 | 163.30 | $-0.09 \pm j3.46, -0.06 \pm j2.92$ $-0.10 \pm j2.38, -0.08 \pm j1.55$ |
| 500 | 2379 | 12.12 | 167.08 | $-0.09 \pm j3.46, -0.06 \pm j2.94$ $-0.10 \pm j2.38, -0.08 \pm j1.54$ |
| 750 | 2341 | 19.06 | 169.08 | $-0.09 \pm j3.46, -0.06 \pm j2.90$ $-0.10 \pm j2.38, -0.08 \pm j1.51$ |

(a) Wind injection in bus 66

| γ | $\ A_4^{I,sg}\ $ | $\ A_4^{I,wg0}\ $ | $\ A_4^E\ $ | Slow eigenvalues |
|----------|------------------|-------------------|-------------|--|
| 0 | 2379 | 0 | 165.63 | $-0.07 \pm j3.17, -0.06 \pm j2.58$ $-0.07 \pm j2.02, -0.07 \pm j1.39$ |
| 250 | 2355 | 5.88 | 166.64 | $-0.07 \pm j3.17, -0.06 \pm j2.46$ $-0.07 \pm j2.02, -0.07 \pm j1.25$ |
| 500 | 2298 | 12.29 | 165.51 | $-0.07 \pm j3.17, -0.06 \pm j2.27$ $-0.07 \pm j2.00, -0.07 \pm j0.92$ |
| 750 | 2186 | 18.68 | 160.99 | $-0.06 \pm j2.08, -0.07 \pm j1.94$ $-0.07 \pm j0.92, \{0.89, -1.01\}$ |

(b) Wind injection in bus 38

Table 4.3: Matrix norms and slow eigenvalues for the 68-bus 16-machine 5-area power system.

located in area 1, where the total connected load is more than the total generation, while in scenario 2 it is located in area 2, where the load is less than generation. Due to the respective proximity of generator 8 and generator 13 to buses 66 and 38, we choose these as the slack generators for the two cases. Table 4.3b shows that the eigenvalues are insensitive to wind penetration in the first case while for the second case the modes get slower with increasing wind penetration ultimately leading to instability. We elaborate the correlation of these observations to the location of the wind bus for each of the scenarios in subsections 4.3.2 and 4.3.2 respectively. The parameters of the power system model are given in [88] while the wind parameters are given in Appendix A.2. For each of the cases, γ is assumed to take values of 0 (the base case), 250, 500 and 750 which respectively correspond to wind penetrations of 0%, 2.5%, 5% and 7.5%

of the total connected load of the system.

Wind injection at bus 66

In this scenario the wind power plant is connected to bus 66 in area 1, as shown in figure 4.5a. For this particular case, $\|A_4^E\|$ increases by a small amount with increasing γ , and hence the slow eigenvalues remain essentially unaffected, as shown in Table 4.3b. The relationship between $\|A_4^E\|$ and γ is complicated by the number of interconnections in this multi-area system. Therefore, it is difficult to determine whether $\|A_4^E\|$ will in general increase or decrease with γ for any generic large power system model such this one. The time response of the aggregate angle difference $(\delta_{s,1} - \delta_{s,2})$, due to an impulse change in the mechanical input of generator 1 is shown in figure 4.5b. As expected based on the eigenvalues, the impulse response is unaffected by changes in γ .

Wind injection at bus 38

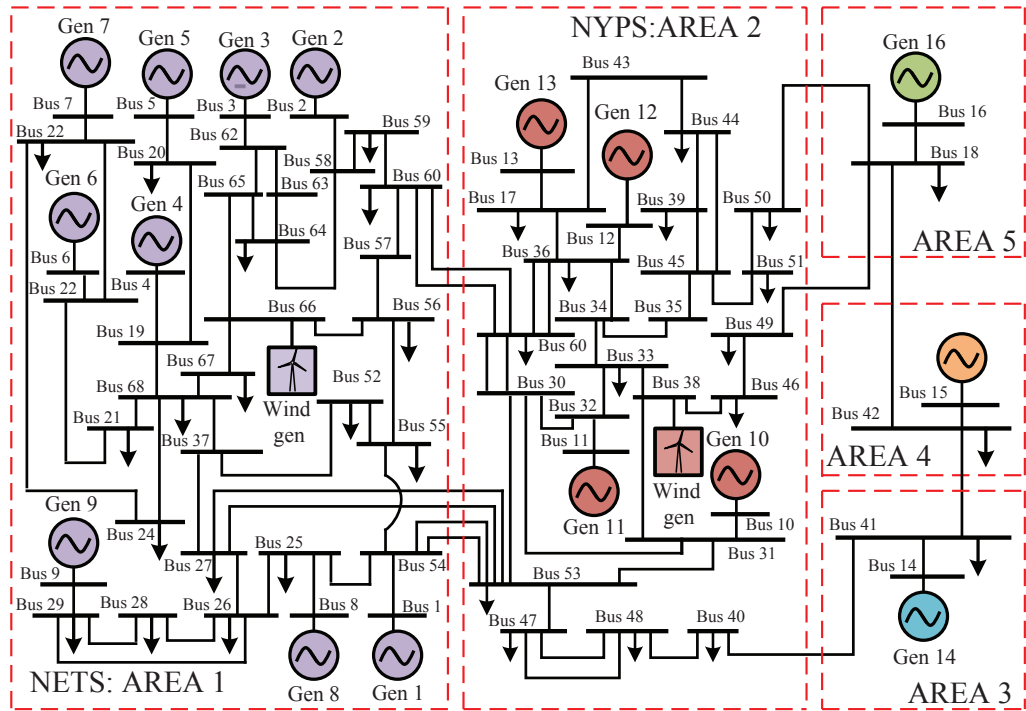
In this scenario the wind power plant is connected to bus 38 in area 2, as shown in figure 4.5a. Here the amount of generation exceeds the connected load of the area. Increasing γ leads to a decrease in $\|A_4^E\|$, as reflected in the slowing down of the slow modes shown in Table IIIb. The time response of the aggregate angle difference $(\delta_{s,1} - \delta_{s,2})$, due to an impulse change in the mechanical input of generator 1 is shown in figure 4.5c. The responses get slower with increasing γ . For $\gamma > 500$, the system becomes unstable, as shown by the positive real eigenvalue in Table 4.3b.

The results suggest that distinct separation of time-scales in a wind power system not only depends on the level of wind injection γ , as quantified by ε_w , but also on the equilibrium angles of the power system, which in turn depend on the system topology and location of the wind plant. The amount of wind penetration and the relative location of the wind plant with respect to conventional generators and loads can change $\|A_4^E\|$ significantly. If $\|A_4^E\|$ is reduced due to increasing γ , the inter-area or slow mode becomes slower. Correspondingly, the aggregate

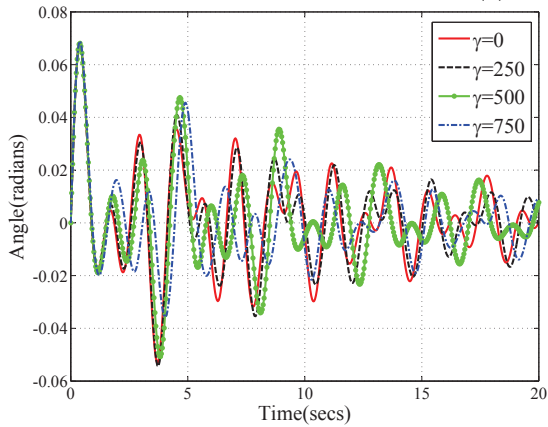
inter-area angle differences also show a slow response for an impulse input. If $\|A_4^E\|$ is below a critically small value it can cause the system to become unstable.

4.4 Conclusions

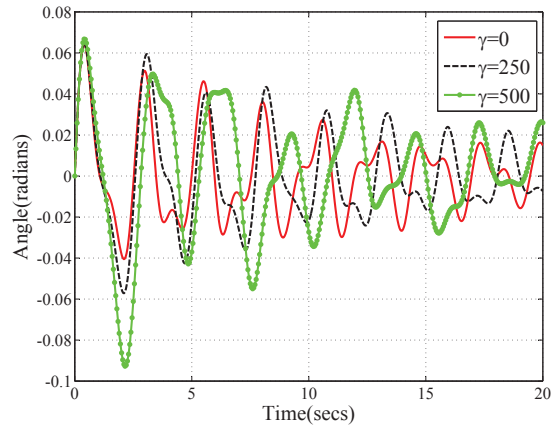
This chapter extended the concept of time-scale separation of coherent power systems to systems with wind penetration. We showed the dependence of the slow time-scales associated with the power system dynamics on the level of wind penetration in a single generation area. The resulting model illustrates that time-scale separation not only depends on the level of wind injection but also on the system topology and location of wind plant. The results further show that increasing wind penetration in certain operating conditions may result in instability. Explicit knowledge of the amount of critical wind penetration that can lead to instability is important for system planning. Our future work will, therefore, focus on finding this critical limit for a general power system model. We will also use the proposed model for designing distributed wide-area oscillation damping controllers.



(a) Power system model



(b) Aggregate angle between area 1 and area 2 with wind at bus 66



(c) Aggregate angle between area 1 and area 2 with wind at bus 38

Figure 4.5: 68-bus, 16-machine, 5-area power system: Scenarios with wind injection at bus 66 and at bus 38

Chapter 5

Equilibria Analysis in Wind-integrated Power Systems

In this Chapter we explore the impact of wind penetration on the equilibrium of a wind integrated power system. In modern power system several dynamic elements like renewables, storage or new loads like plug-in electric vehicles are accompanied by their individual controllers for following local control objectives such as following a power output reference, controlling bus voltage, maximizing efficiency, etc. Accordingly, the properties of the power system equilibrium or the power flow solutions become increasingly dependent on the mutual interaction of various parameters of these elements. The traditional load flow studies based on iterative methods are inadequate to compute the equilibrium over a parameter space particularly when multiple equilibria may exist for certain operating conditions. Knowledge of all the feasible equilibria and their stability properties can be a valuable information to the system operator for planning power dispatch and take control decisions. Particularly we show in the later half of this chapter as to how the proposed method can be helpful in detecting power flow solution boundary which is a measure of the transient voltage stability limit. However, there is still a dearth of insight on how the parameters of the different elements may mutually interact to alter the equilibrium property. So in this Chapter we investigate the the effect of increasing wind penetration on

power system equilibrium first and try to find all real equilibrium for different penetration levels. Thereafter we also figure out power flow solution boundary or voltage security limit in a multiple wind injection scenario. We use a recent parameter homotopy based method, Numerical Polynomial Homotopy Computation (NPHC) [12] which guarantees to find all complex and hence real equilibria over a given parameter space.

5.1 Dynamic Model of Power System

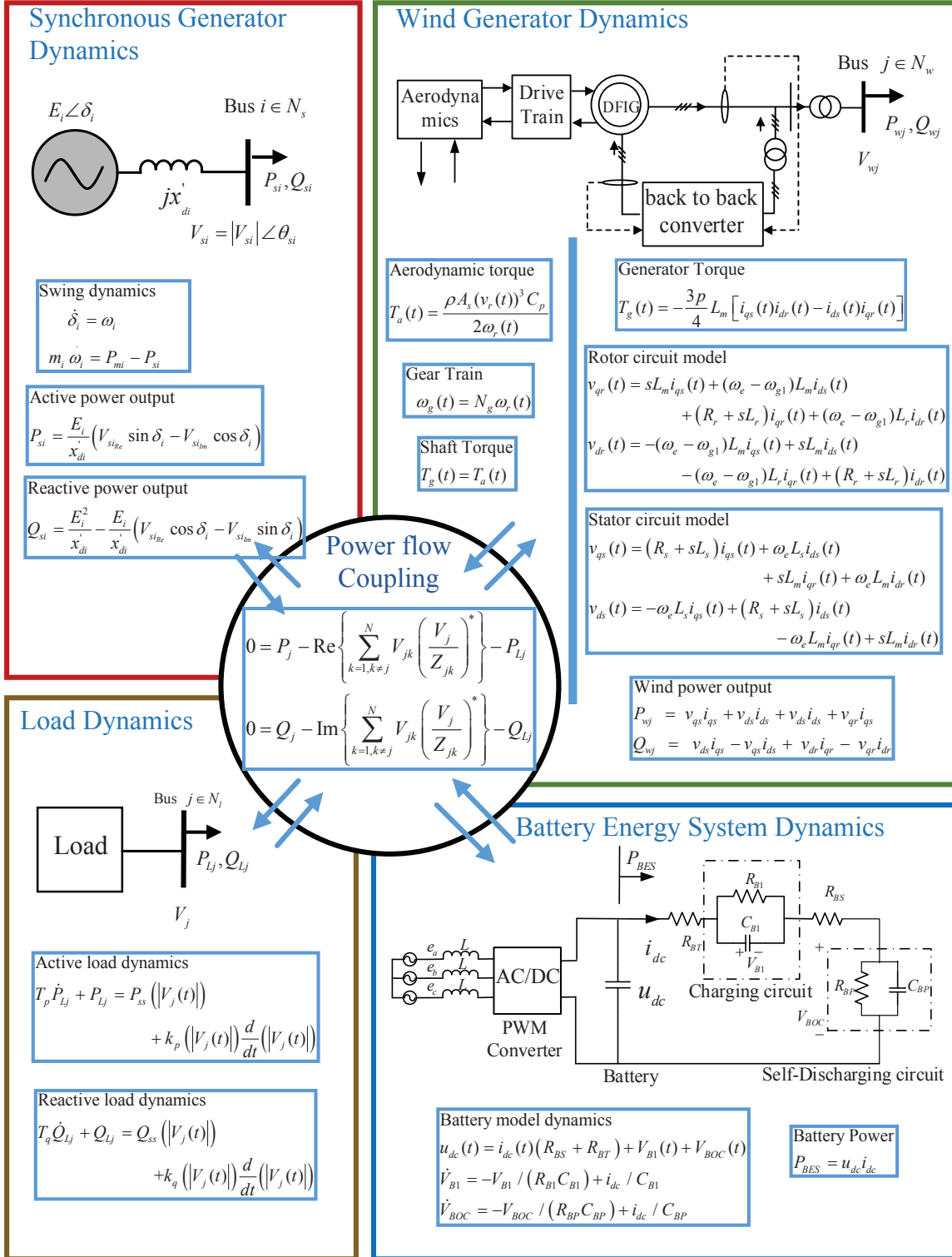
We consider a power system with N buses and n generators. These generators are either synchronous generators belonging to a set $\mathcal{G} =: \{1, \dots, n_s\}$ or a wind power plant (WPP) in set $\mathcal{W} =: \{1, \dots, n_w\}$, where $n_s + n_w = n$. Each WPP consists of a number of wind turbines and a battery energy system all connected to a point of common coupling, a particular bus in the power system. Without loss of generality we can reorder the buses and classify them into 3 sets namely the set of synchronous generator bus $\mathcal{N}_s =: \{1, \dots, n_s\}$, the wind injection bus $\mathcal{N}_w =: \{n_s + 1, \dots, n\}$ and the other load buses $\mathcal{N}_l =: \{n + 1, \dots, N\}$. To obtain the equilibrium for this system, our first task is to derive its dynamic model considering the nonlinear swing dynamics, wind power dynamics, battery model, load dynamics and power flow as shown in figure 5.1. This is presented in the following subsections.

5.1.1 Synchronous Generator Model

We model each generator $i \in \mathcal{G}$ using the swing equations,

$$\dot{\delta}_i = \omega_i \quad m_i \dot{\omega}_i = P_{mi} - P_{si} \quad (5.1)$$

Here δ_i , ω_i , m_i , P_{mi} and P_{si} are respectively the phase angle, rotor speed, inertia, the mechanical power input and the active power output of synchronous generator $i \in \mathcal{G}$. The active and



reactive power output of the synchronous generator $i \in \mathcal{G}$ can be respectively shown as,

$$P_{si} = \frac{E_i}{x'_{di}} (V_{si_{Re}} \sin \delta_i - V_{si_{Im}} \cos \delta_i) \quad (5.2a)$$

$$Q_{si} = \frac{E_i^2}{x'_{di}} - \frac{E_i}{x'_{di}} (V_{si_{Re}} \cos \delta_i - V_{si_{Im}} \sin \delta_i), \quad (5.2b)$$

where, E_i is the internal voltage and x'_{di} is the direct-axis salient reactance of the machine $i \in \mathcal{G}$. $V_{si} = V_{si_{Re}} + jV_{si_{Im}}$ is the voltage at bus $i \in \mathcal{N}_s$. Also $V_{si_{Re}} = |V_{si}| \cos \theta_{si}$ and $V_{si_{Im}} = |V_{si}| \sin \theta_{si}$, θ_{si} being the phase angle of the voltage at bus $i \in \mathcal{N}_s$. The states of the synchronous generator i are coupled with the states of other components of the power system via power flow. The bus voltage V_{si} being the coupling variable as shown in the next subsections.

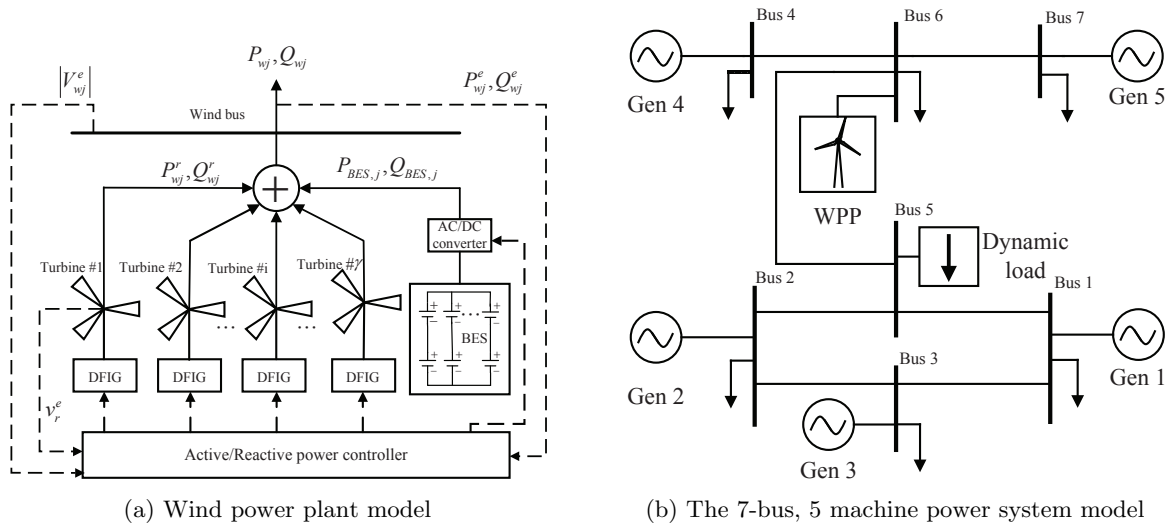


Figure 5.2: Schematic representation of the WPP and the power system

5.1.2 WPP Model

The WPP is modeled as a group of type III wind generators injecting power to the grid via doubly fed induction generators (DFIG) at a point of common coupling, the wind bus $j \in \mathcal{N}_w$.

A BES is also connected to the same bus j , with a controller which tracks an active power reference for the WPP, as the wind speed varies from its rated value. The reactive power output of the WPP is controlled so as to ensure that the wind bus voltage magnitude tracks a reference, as shown in figure 5.2a. The power output of the resulting ‘wind injection’ depends on a constant γ_j which represent the number of wind turbines connected to the wind bus. We consider all wind turbines connected to bus j to be identical, and therefore discuss the turbine and DFIG models for a general turbine ‘ r ’. However for convenience, we skip the subscript r in the following derivations. The model of the wind generator and the BES at bus j are derived next. The wind generator model consists of a mechanical rotor and a DFIG described as follows.

Mechanical Rotor

The mechanical rotor of the wind turbine is connected to the DFIG via a drive train which is modeled as two connected shafts operating at high and low speeds. The aerodynamic torque $T_a(t)$ of the turbine due to wind speed $v_r(t)$ is given as,

$$T_a(t) = \frac{\rho A_s (v_r(t))^3 C_p(\lambda(t), \beta)}{2\omega_r(t)} \quad (5.3)$$

where, A_s is the swept area of the turbine blades, C_p is the power coefficient, $\lambda(t)$ is the blade tip speed ratio, β is the pitch angle, $\omega_r(t)$ is the speed of the turbine rotor, ρ is the air density. The power coefficient C_p is defined as,

$$C_p(\lambda(t), \beta) = 0.22 \left(\frac{116}{\lambda_i(t)} - 0.4\beta - 5 \right) e^{-\frac{12.5}{\lambda_i(t)}} \quad (5.4)$$

where, $\lambda_i(t) = 1/[1/(\lambda(t) + 0.08\beta) - 0.035/(\beta^3 + 1)]$, $\lambda(t) = \omega_r(t)R/v_r(t)$, R being the length of the wind turbine blade. We assume that the turbine is operating above the rated wind speed and the pitch angle $\beta = 0$ at all times. Aerodynamic torque of the rotor is transferred via a shaft as the electromagnetic torque $T_g(t)$ driving the DFIG. Considering the frictional losses on the shaft to be negligible and a gear ratio N_g , the electromagnetic torque and the mechanical

speed of the DFIG are shown as,

$$T_g(t) = T_a(t) \quad \omega_g(t) = N_g \omega_r(t) \quad (5.5)$$

Next we show the dynamic model of the DFIG.

DFIG Model

The DFIG is modeled through the dynamics of its stator and rotor variables, expressed in a rotating $d - q$ reference frame as [96],

$$v_{qs}(t) = (R_s + \mathcal{D}L_s) i_{qs}(t) + \omega_e L_s i_{ds}(t) + \mathcal{D}L_m i_{qr}(t) + \omega_e L_m i_{dr}(t) \quad (5.6a)$$

$$v_{ds}(t) = -\omega_e L_s i_{qs}(t) + (R_s + \mathcal{D}L_s) i_{ds}(t) - \omega_e L_m i_{qr}(t) + \mathcal{D}L_m i_{dr}(t) \quad (5.6b)$$

$$v_{qr}(t) = \mathcal{D}L_m i_{qs}(t) + (\omega_e - \omega_{ge}) L_m i_{ds}(t) + (R_r + \mathcal{D}L_r) i_{qr}(t) + (\omega_e - \omega_{ge}) L_r i_{dr}(t) \quad (5.6c)$$

$$v_{dr}(t) = -(\omega_e - \omega_{ge}) L_m i_{qs}(t) + \mathcal{D}L_m i_{ds}(t) - (\omega_e - \omega_{ge}) L_r i_{qr}(t) + (R_r + \mathcal{D}L_r) i_{dr}(t), \quad (5.6d)$$

where $\omega_{ge} := \frac{p}{2} \omega_g$ is the electrical speed, p is the number of electrical poles of the DFIG, and \mathcal{D} is the time-differential operator. The subscripts d and q refer to the direct and quadrature axes of the reference frame rotating at constant speed ω_e . Subscripts s and r respectively indicate quantities associated with the stator and rotor circuits. The symbols v , i , and R respectively denote voltage, current, and resistance. L_{ls} , L_{lr} , L_m are respectively the stator and rotor leakage inductances, and the magnetizing inductance. The electromagnetic torque T_g is related to the DFIG currents as shown below,

$$T_g(t) = -\frac{3p}{4} L_m [i_{qs}(t) i_{dr}(t) - i_{ds}(t) i_{qr}(t)]. \quad (5.7)$$

The active and reactive power of a DFIG at bus j are,

$$P_{t,j} = v_{qs} i_{qs} + v_{ds} i_{ds} + v_{dr} i_{dr} + v_{qr} i_{qr} \quad (5.8a)$$

$$Q_{t,j} = v_{ds}i_{qs} - v_{qs}i_{ds} + v_{dr}i_{qr} - v_{qr}i_{dr}. \quad (5.8b)$$

However, (5.7) is dependent on (5.6a)-(5.6d) and (5.8a). So while calculating the equilibria, one of the equations of (5.6a)-(5.6d) is ignored to avoid an overdetermined system. The stator of the DFIG is directly connected to the wind injection bus. The q and d directions in our analysis are so chosen that v_{qs} and v_{ds} align with $V_{wi_{Re}}$ and $V_{wi_{Im}}$, the real and imaginary parts of the voltage V_{wi} of bus $i \in \mathcal{N}_w$, respectively. V_{wi} , therefore, serves as the coupling variable for the DFIG states to the rest of the system. We next derive the battery model connected to the point of common coupling in the wind power system.

Battery Energy System Model

Next we derive the dynamic model for the active and reactive power output $P_{BES,j}$ and $Q_{BES,j}$ of the battery connected to bus j . The actual battery model consists of a set of batteries connected in series or parallel, a pulse-width modulation (PWM) based AC-DC converter and a controller [50]. For our study, we will consider a single equivalent battery model with a converter. We assume a rotating $d-q$ reference frame representation of the 3-phase supply to the converter. The average model of the three phase PWM converter in $d-q$ reference frame can be expressed as

$$L \frac{di_d}{dt} = d_d u_{dc} + \omega_e i_q - v_d \quad (5.9a)$$

$$L \frac{di_q}{dt} = d_q u_{dc} - \omega_e i_d - v_q \quad (5.9b)$$

$$C \frac{du_{dc}}{dt} = i_{dc} - d_d i_d - d_q i_q \quad (5.9c)$$

where the variables, v , i and d refer to the terminal voltage, current and duty cycle of the converter. The subscripts d and q refer to the direct and quadrature axes of the reference frame rotating at constant speed ω_e . L and C are filter inductance and dc-link capacitance. u_{dc} and i_{dc} are the battery terminal voltage and current. The active and reactive power output of the

BES are given as,

$$P_{BES} = v_q i_q + v_d i_d, \quad Q_{BES} = v_d i_q - v_q i_d \quad (5.10)$$

where q and d directions are so chosen that v_q and v_d align with $V_{wi_{Re}}$ and $V_{wi_{Im}}$ respectively. The internal battery model does have its own dynamics of charging or discharging and self discharge. But in this work we are only concerned with active and reactive power output of the converter of the BES (5.10). Thus, the net power output of the WPP is shown as,

$$P_{wj} = \gamma_j P_{t,j} + P_{BES,j} \quad Q_{wj} = \gamma_j Q_{t,j} + Q_{BES,j}. \quad (5.11)$$

5.1.3 Dynamic Load Model

The dynamic model for the active and reactive power consumed by the loads connected to bus j are respectively shown as below,

$$T_p \dot{P}_{Lj} + P_{Lj} = P_{ss} (|V_j(t)|)^{\alpha_s} - P_{ss} (|V_j(t)|)^{\alpha_t} \quad (5.12a)$$

$$T_q \dot{Q}_{Lj} + Q_{Lj} = Q_{ss} (|V_j(t)|)^{\alpha_s} - Q_{ss} (|V_j(t)|)^{\alpha_t}. \quad (5.12b)$$

Here, T_p and T_q are the time constants, P_{ss} and Q_{ss} are the rated power consumptions and α_t and α_s are the transient and the steady-state load-voltage dependence of the loads respectively.

5.1.4 Power Flow Model

The dynamics of individual components in the power system are connected by the active and reactive power flow equations [39] between the different buses which are shown as,

$$P_j = \text{Re} \left\{ \sum_{k=1, k \neq j}^N V_{jk} \left(\frac{V_j}{Z_{jk}} \right)^* \right\} + P_{Lj} \quad (5.13a)$$

$$Q_j = \text{Im} \left\{ \sum_{k=1, k \neq j}^N V_{jk} \left(\frac{V_j}{Z_{jk}} \right)^* \right\} + Q_{Lj}. \quad (5.13b)$$

Here P_j and Q_j respectively denote the active and reactive power flow from the generators connected to bus j , P_{Lj} and Q_{Lj} are respectively the active and reactive power consumed by the load together with line charging of bus j . Z_{jk} is the impedance of the lines connecting buses j and k , and $V_{jk} = (V_{jRe} - V_{jRe}) + j(V_{kRe} - V_{kIm})$. For any bus $j \in \mathcal{N}_s$, P_j and Q_j are respectively equal to P_{sj} and Q_{sj} shown in (5.2). For any bus $j \in \mathcal{N}_w$, P_j and Q_j are respectively equal to P_{wj} and Q_{wj} shown in (5.11). If $j \in \mathcal{N}_l$, P_j and Q_j are both equal to 0. The overall model of the wind integrated power system is, thus, comprised of the differential-algebraic equations (5.1)-(5.13). Next, we analyze the equilibria for this model.

5.2 Equilibrium Analysis

Here, we derive the equilibrium or the steady-state values of all the dynamic variables in the power system shown in (5.1)-(5.13). The superscript e for any variable from now onwards will be used to indicate its equilibrium value(s). Steady-state power flow equations are derived for each bus in the power system. One of the synchronous generator bus $i \in \mathcal{N}_s$ is assumed to be the slack bus, for which $|V_{si}^e|$ and θ_{si}^e are respectively equal to 1 and 0. The steady-state active and reactive power flow, P_{si}^e and Q_{si}^e can be obtained by solving,

$$P_{si}^e = \text{Re} \left\{ \sum_{k=1, k \neq i}^N (1 - V_k^e) \left(\frac{1}{Z_{ik}} \right)^* \right\} + P_{Li}^e \quad (5.14a)$$

$$Q_{si}^e = \text{Im} \left\{ \sum_{k=1, k \neq i}^N (1 - V_k^e) \left(\frac{1}{Z_{ik}} \right)^* \right\} + Q_{Li}^e. \quad (5.14b)$$

For all other buses the power flow is specified by,

$$P_j^e = \text{Re} \left\{ \sum_{k=1, k \neq j}^N V_{jk}^e \left(\frac{V_j^e}{Z_{jk}} \right)^* \right\} + P_{Lj}^e \quad (5.15a)$$

$$Q_j^e = \text{Im} \left\{ \sum_{k=1, k \neq j}^N V_{jk}^e \left(\frac{V_j^e}{Z_{jk}} \right)^* \right\} + Q_{Lj}^e. \quad (5.15b)$$

If $j \in \mathcal{N}_s$ such that $j \neq i$, P_j^e , Q_j^e , V_j^e in (5.15) are replaced by P_{sj}^e , Q_{sj}^e , V_{sj}^e . The synchronous generator buses are PV buses and hence θ_{sj}^e and Q_{sj}^e are obtained by solving the equilibrium equations. If $j \in \mathcal{N}_w$, P_j^e , Q_j^e and V_j^e in (5.15) are replaced by P_{wj}^e , Q_{wj}^e and V_{wj}^e . The wind generator buses are solved as PV buses where θ_{wj}^e and Q_{wj}^e are obtained by solving the equilibrium. If $j \in \mathcal{N}_l$, P_j^e , Q_j^e and V_j^e in (5.15) are replaced by 0, 0 and V_{lj}^e . The load buses are solved as PQ buses where θ_{lj}^e and $|V_{lj}^e|$ are obtained by solving the equilibrium equations.

However, the stator voltages of the DFIG v_{qs}^e and v_{ds}^e are respectively equal to V_{wjRe} and V_{wjIm} . So the steady-state equations of the wind generators also need to be solved simultaneously with the power system. The equations related to a single wind turbine are given as,

$$T_g^e = -(3p/4) L_m [i_{qs}^e i_{dr}^e - i_{ds}^e i_{qr}^e] \quad (5.16a)$$

$$v_{qs}^e = R_s i_{qs}^e + \omega_e L_s i_{ds}^e + \omega_e L_m i_{dr}^e \quad (5.16b)$$

$$v_{ds}^e = -\omega_e L_s i_{qs}^e + R_s i_{ds}^e - \omega_e L_m i_{qr}^e \quad (5.16c)$$

$$v_{qr}^e = (\omega_e - \omega_{ge}) L_m i_{ds}^e + R_r i_{qr}^e + (\omega_e - \omega_{ge}) L_r i_{dr}^e \quad (5.16d)$$

$$P_{tj}^e = (v_{qs}^e i_{qs}^e + v_{ds}^e i_{ds}^e + v_{dr}^e i_{dr}^e + v_{qr}^e i_{qr}^e) \quad (5.16e)$$

$$Q_{tj}^e = (v_{ds}^e i_{qs}^e - v_{qs}^e i_{ds}^e + v_{dr}^e i_{qr}^e - v_{qr}^e i_{dr}^e) \quad (5.16f)$$

where the generator torque is equal to the aerodynamic torque, $T_g^e = T_a^e = (\rho A_s (v_r^e)^3 C_p^e) / (2\omega_r^e)$. The equilibrium equations of the BES connected to the wind bus j are shown as,

$$P_{BES,j}^e = v_q^e i_q^e + v_d^e i_d^e \quad Q_{BES,j}^e = (v_d^e i_q^e - v_q^e i_d^e), \quad (5.17)$$

which are coupled to the power system by bus voltages. Equilibrium equations of the WPP at bus j are shown as,

$$P_{wj}^e = \gamma_j P_{t,j}^e + P_{BES,j}^e \quad Q_{wj}^e = \gamma_j Q_{t,j}^e + Q_{BES,j}^e. \quad (5.18)$$

The steady-state load models for any bus $j \in \mathcal{N}$,

$$P_{Lj}^e = P_{ss} (|V_j^e|)^{\alpha_{sj}} \quad Q_{Lj}^e = Q_{ss} (|V_j^e|)^{\alpha_{sj}}. \quad (5.19)$$

The complete equilibria of the wind-integrated power system can be obtained by solving the set of nonlinear algebraic equations shown in (5.14)-(5.19). In this work we assume the wind penetration level γ_j to be constant and equal to 1. Thus these algebraic equations depend upon the wind speed v_r^e , the set point $|V_{wj}^e|$ for controlling the voltage level of the wind bus and the load type specified by α_{sj} . In other words, the equilibrium points of the system are parameterized by v_r^e , $|V_{wj}^e|$ and α_{sj} which we numerically solve in the next section using a homotopy based method.

5.3 Parameter Homotopy Continuation Algorithm

In this section we solve for all real equilibrium of the power system model as shown in (5.14)-(5.19) over a parameter space using NPHC. Polynomial homotopy continuation method has been recently used to solve quite a few problems in particle physics [15, 30, 32--34, 36, 53--56, 58, 59, 62, 63, 65, 67], and statistical physics [41, 57, 60, 61, 66, 76]. More recently, this method has been applied to the areas of power systems, power networks and complex systems [12, 64, 68]. As a preconditioning, we represent the algebraic equations of the power system model shown in (5.14)-(5.19) as multivariate polynomials by expanding the voltage phasor V_j at any bus $j \in \mathcal{N}$ into its real and imaginary parts, such that $V_j = V_{jRe} + I * V_{jIm}$. The resulting system consists of $2N + n - 1$ quadratic equations which will improve the computational effort as shown in the later half of the section. A general set of nonlinear polynomial equations in variable x and parameter λ is shown as,

$$P(x, \lambda) = (p_1(x, \lambda), \dots, p_m(x, \lambda))^T = 0, \quad \forall x \in \mathbb{C}^m, \quad (5.20)$$

where, $x \in \mathbf{R}^{(2N+n-1)}$ and $\lambda \in \mathbf{R}^p$. As a first step, an upper bound of the number of complex isolated solution of (5.20) is determined, based on which a homotopy $H(x, t)$ can be formed as shown below,

$$H(x, t) = \gamma_h(1 - t)Q(x) + t P(x). \quad (5.21)$$

Here $Q(x)$ and $P(x)$ are system of polynomials, γ_h is a is a generic complex number and t is a continuous variable varying from 0 to 1. $Q(x)$, also known as the start system is so chosen that it is easily solvable and the number of solutions of $Q(x) = 0$, is equal to the estimated upper bound. Therefore the solution set of $H(x, t) = 0$ for $0 \leq t \leq 1$ consists of a finite number of smooth paths parameterized by $t \in [0, 1)$. For a generic $\gamma_h \in \mathbb{C}$, it is proven that each of the paths will be well-behaved, i.e., either they will converge to $H(x, 1) = 0$, or will diverge to infinity. Hence, with generic value of γ_h , the NPHC method guarantees to find all isolated complex solutions [73] of $P(x) = 0$. The crux of the algorithm is to track each solution of $H(x, t) = 0$ for $t \in [0, 1)$ using an efficient predictor-corrector method [6] to obtain all complex solutions for $P(x) = 0$.

Now a system of m polynomials can have a maximum of $\prod_{i=1}^m \phi_i$ number of isolated complex solutions, where ϕ_i is the degree of the i^{th} polynomial, as specified by the classical Bézout theorem. This poses an upper bound on the number of solutions to be tracked for NPHC method known as classical Bézout bound (CBB). In the case of wind integrated power flow with $(2N + n - 1)$ algebraic equations, each of order 2, the number of paths to be tracked is $2^{(2N+n-1)}$. This translates to the fact that in case of a power system the number of paths to be tracked grows exponentially with the number of buses. Choice of quadratic power flow equations actually pays off here by allowing a tighter upper bound on the number of complex isolated solutions or the CBB. However this crude upper bound does not capture the specific complex algebraic structure of the systems at hand. Moreover in our work, we need to solve the algebraic equations following from (5.14)-(5.19) over a certain parameter space constituted by the wind parameters. Solving such parametric systems for every parameter-point from scratch using the NPHC method can be computationally very exhaustive. We therefore use a more sophisticated

approach based on the following result, parameter-coefficient homotopy [74](an earlier version of which was called Cheater’s homotopy [47]); For a parameteric system of polynomial equations, the maximum number of isolated complex solutions over all parameter-points is same as that for a generic complex parameter-point. Hence, instead of solving the equations from scratch for each parameter-point, one first solves $P(x, \lambda) = 0$, at a *generic* complex parameter-point $\lambda^* \in \mathbb{C}^m$, using the NPHC method with the help of some crude upper bound on the number of complex solutions such as the CBB. Though such a complex parameter-point is physically not meaningful, solving the system at such a point reduces the computation for all other physically relevant parameter-points. Next, we choose $P(x, \lambda^*) = 0$ as the start system for all other parameter-points $\lambda \in \mathbb{C}^m - \{\lambda^*\}$. Each solution of this start system needs to be tracked with the following homotopy:

$$H(x, \lambda, t) = (1 - t)P(x, \lambda^*) + t P(x, \lambda) = 0. \quad (5.22)$$

from $t = 0$ to $t = 1$. This procedure again guarantees *all* isolated complex solutions at each of the chosen parameter-points, independent of the upper bound chosen to solve the system at the generic point in the first step. In most systems arising from applications, the number of paths to be tracked in the first step (e.g., the CBB) dramatically reduces to a very small integer in the second step. Hence, the procedure is computationally very efficient once the system is solved at a generic complex parameter points as the number of paths to be tracked for any other parameter-point. Moreover, the procedure of solving the system at each parameter-point is independent of solving it at any other parameter-piont and hence completely parallelizable. For our computations, we use a novel computational package called *Paramotopy* [5] which efficiently implements the above mentioned procedure with appropriate parallelization. Once *all* real solutions are predicted at each parameter point one can accurately estimate the power flow solution boundaries where the number of real solutions change, given the parameter space is densely represented. Next, we apply this method to solve the equilibrium of (5.14)-(5.19) over a

| | $v_r^e = 0.9$ | $v_r^e = 1.1$ |
|---------------------|--|------------------------|
| $ V_{w6}^e = 0.96$ | 1 stable equilibrium | 1 unstable equilibrium |
| $ V_{w6}^e = 0.98$ | 3 stable equilibria | 1 stable equilibrium |
| $ V_{w6}^e = 1.00$ | 2 stable equilibria, 1 unstable equilibrium | 1 stable equilibria |

Table 5.1: Types of feasible equilibrium for various wind speeds (v_r^e) and wind bus voltage levels $|V_{w6}^e|$

given parameter space constituted by v_r^e , $|V_{wj}^e|$ and α_{sj} .

5.4 Results

We use the 7-bus, 5-machine power system as shown in figure 5.2b, for the simulation. A WPP is considered to be connected to the power system at bus 6. The parameters of the simulation are given in [12]. From the given parameter values the rated active power output of the WPP is $P_{w6}^e = 0.71$ p.u. when the wind speed is $v_r^e = 1$ p.u., obtained by the maximum power point tracking algorithm [21]. We next vary the wind speed v_r^e from 0.9 to 1.1 p.u. in steps of 0.1 p.u. and let the active power controller of the WPP give the BES a command so as to ensure that the WPP still delivers 0.71 p.u. to the power system. The reactive power controller provides a command to the wind generators and the BES in the ratio of their active power outputs, to maintain $|V_{w6}^e|$ at a constant level. We consider the setpoint value of $|V_{w6}^e|$ as the second parameter of our interest and assume three values for it, 0.96, 0.98 and 1.0 p.u. The load connected at bus 5 is a dynamic load, whose steady-state voltage dependence α_{s5} is treated as the third parameter of our interest taking values of 0 and 2. We formulate our equilibrium analysis problem of solving (5.14)-(5.19) about these parameters and solve it efficiently over the entire parameter space using the homotopy based algorithm of section 5.3, implemented in *Mathematica* and *Bertini* [6]. Key facts on the application of the algorithm are as follows ,

1. λ^* in equation (5.22) is a generic complex vector with three elements which are chosen from uniform distributions such as $\{a + ib : -1 \leq a, b \leq 1\}$ and are normalized to ensure they are inside unit circle.

| | $v_r^e = 0.9$ | $v_r^e = 1.1$ |
|---------------------|--|-------------------|
| $ V_{w6}^e = 0.96$ | $-0.01 \pm 0.69i$ | – |
| $ V_{w6}^e = 0.98$ | $-0.02 \pm 0.69i$ | $-0.01 \pm 0.71i$ |
| | $-0.03 \pm 0.70i$ $-0.03 \pm 0.70i$ | |
| $ V_{w6}^e = 1.00$ | $-0.05 \pm 0.71i$ | $-0.03 \pm 0.72i$ |
| | $-0.05 \pm 0.71i$ | |

Table 5.2: Dominant pair of Eigen values for different stable equilibria

2. The system of equations $P(x, \lambda^*) = 0$ is formed from (5.14)-(5.19), by replacing the parameters with the individual components of λ^* .
3. We start from the solutions of $P(x, \lambda^*) = 0$, and employ a predictor-corrector method to track all solutions paths of (5.22) from $t = 0$ to $t = 1$. These paths culminate into solutions of $P(x, \lambda) = 0$ which includes the solutions of (5.14)-(5.19) over the desired parameter space.
4. Each of the solution paths can be tracked independent of all others, thus enabling parallelization and faster convergence to *all* the desired solutions.

It is observed that since the voltages at different buses in the power system are tightly controlled, α_{s5} does not have a significant effect on the nature or value of the equilibria. But for different combinations of $|V_{w6}^e|$ and v_r^e the number of feasible equilibria and their type varies as depicted in table 5.1. For $|V_{w6}^e| = 0.96$ p.u. and $v_r^e = 1.1$ p.u., the feasible equilibrium is found to be unstable, justifying the use of our approach for computing all equilibria. For the selected combinations we compute the Jacobian matrices of (5.1)-(5.13) numerically and list the dominant eigenvalues of the state matrix in table 5.2. Even among the stable equilibria the damping of the eigenvalues decreases with increasing wind speed thereby indicating the adverse impacts of excessive wind penetration on the small-signal dynamic performance of the power system. This method can be used for planning studies in power system as well as for designing wind and battery controllers to avoid undesired equilibria.

5.4.1 Discussion: On the Network Topology and Upper Bound on the Number of Equilibria

For a system which has only a few complex solutions compared to the classical Bézout bound, the computational effort to track the homotopy paths that would eventually diverge is wasted. Hence, to solve large systems, one needs to exploit the specific structure or the sparsity of systems at hand and coming up with a tighter upper bound. Particularly in case of a power system, the network topology of the buses is usually known. One would wonder if the network topology on the maximum number of connections of a bus in the system to its neighboring buses can be exploited to obtain tighter upper bounds. A lot of effort has been invested to compute tighter upper bounds than the CBB for the power flow systems. A recent review on the existing results is provided in [72]. Briefly, an upper bound, $\binom{2N-2}{N-1}$ for general system of power flow equations with N buses was computed in [3], though it did not still exploit the network topologies. In [31], the number of complex solutions for networks with cliques with exactly one common node was shown to be equal to the product of number of complex solutions for the individual cliques as independent networks. In [72], this result is extended to other related network topologies, though several of the patterns for the particular topologies considered in that work are yet to be understood. Moreover, analogous results for many other types of network topologies are yet to be obtained.

In the current work, studying the number of equilibria of the power flow equations was not our goal, still we point out an interesting observation arising from our study that could help advance the knowledge on the problem of number of equilibria. For the networks we considered in this work, the CBB of the systems is dramatically small compared to the number of complex solutions at a generic complex parameter-point, which is now the new and very tight upper bound on the number of complex isolated solutions. e.g., for the 3 bus case, the CBB was 2^8 whereas the number of complex solutions at a generic point was just 6, which is the same as the above mentioned binomial bound. However, for the 10 bus case, the CBB was 2^{25} , the number of complex solutions is 2^9 , which is quite small compared to the binomial bound

48620. The parameter homotopy method does not directly yield how exactly the structure or the sparsity of the system at hand is exploited to reduce the upper bound. Our observation yields that the tighter most upper bound for the system of power flow equations may be the number of complex solutions at a generic complex parameter-point if the system is considered as a parametric system. The number of complex solutions of a parametric system at a generic point is equal to the so-called Bernstein-Khovanskii-Kushnirenko (BKK) bound [7, 42, 45]. Based on this observation, we make a conjecture that a tight upper bound on the number of complex and real solutions for the power flow equations is the BKK bound or a closely related number to the BKK bound. Discussion of these aspects of the number of complex solutions and upper bound on the number of real solutions is beyond the scope of this work.

5.5 Background for Power Flow Solution Boundary

With substantial growth in renewable energy sources like wind [75], solar [23] etc., one of the most critical challenges of power system operation will be to maintain power system security. Among different security measures, transient voltage stability is a critical one which needs to be preserved almost consistently at all the times. Typically the transient voltage stability limit is characterized by a power flow solution space boundary or a loadability boundary at which the Jacobian matrix of the power flow function is singular [43]. Choice of operating points of the power system away from the loadability boundary makes the system robust and reduces the subsequent risk of disruption of service or blackout. Thus identification of this power flow solution boundary for different penetration levels of the renewable energy resources is a highly relevant problem with respect to modern power system planning. Several works have been proposed in literature which addresses the problem of finding the power flow solution boundary [37, 85] by applying continuity method. In [35] Hiskens et al. proposes a technique based on predictor-corrector method to identify the power flow solution boundary on a given multi-dimensional parameter space of the power system. The technique consists of two steps. Initially the solution space boundaries are represented as a solution of the set of equations as

shown below,

$$f(x, \lambda) = 0 \tag{5.23a}$$

$$g(x, \lambda, v) = f_x(x, \lambda)v = 0 \tag{5.23b}$$

$$h(v) = v^T v = 1 \tag{5.23c}$$

where $x \in \mathbf{R}^n$ is a vector of unknown power flow states and $\lambda \in \mathbf{R}^p$ is a set of parameters which can vary according to specific conditions. The power flow function $f : \mathbf{R}^{n \times p} \rightarrow \mathbf{R}^p$ is parameterized by λ and has a Jacobian matrix f_x with respect to x . $v \in \mathbf{R}^n$ is a right eigenvector corresponding to a singular eigenvalue of f_x . In the first step one of the parameters say λ_1 is varied while all others are kept at constant. Correspondingly, (5.23) becomes a set of $2n + 1$ equations with $2n + 1$ unknowns which can be solved via computational methods like Newton-Raphson with an initial guess. The first step will provide an initial point on the solution space boundary. Once an initial point is identified a gradient based predictor-corrector tracking is implemented using the Jacobian as shown below,

$$J = \begin{bmatrix} \frac{\partial f}{\partial x} & \frac{\partial f}{\partial \lambda} & 0 \\ \frac{\partial g}{\partial x} & \frac{\partial g}{\partial \lambda} & \frac{\partial g}{\partial v} \\ 0 & 0 & \frac{\partial h}{\partial v} \end{bmatrix} \tag{5.24}$$

However the drawback of this approach [35] is that it does not guarantee to find all the solution space boundaries over a given parameter space. All solution space boundaries can only be identified if at least one initial point is chosen uniquely for each of the boundaries which are disjoint from each other. Such gradient based methods are also heavily dependent on the structure of the solution space and may yield only one boundary as shown in an example in section 5.6.1. Second part of the tracking method depends on local approximations of the solution space boundary which holds only if the boundary is smooth. However there are some literature [40, 80] which suggests that the solution boundary is non-smooth due to inequality

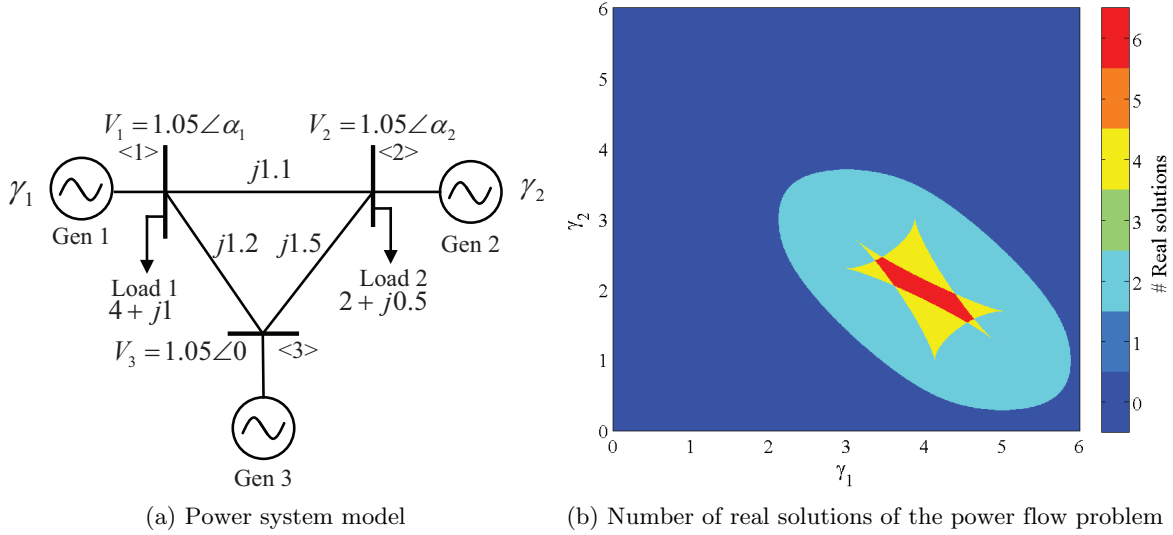


Figure 5.3: 3-bus power system with two parameters

constraints in the power flow problem occurring due to generator over-excitation limits or the reactive power limits etc. These boundaries are thus difficult to be tracked by the continuity methods. In order to resolve this issue and to guarantee all the solution boundaries, in this work we adopt a different method as compared to the continuity based tracking. At the power flow solution boundary the number of real solutions of the power flow problem changes, also denoted as bifurcation points. Thus given a parameter space if all the isolated real solutions are computed at different parameter points, one can find the boundaries where the number of real solution changes. We employ a homotopy based continuation method to find *all* complex and hence real solutions of the power system in the given parameter space. There have been a few works in literature which employ homotopy continuation methods [2, 43, 48, 52, 71, 86] to solve power flow equations. However, these homotopy constructions either do not guarantee to obtain all the equilibria of the given system or scale badly with increasing number of buses. Only recently all solutions of power flow equations have been obtained for IEEE standard systems up to 14 bus [64] using the numerical polynomial homotopy continuation (NPHC) method [46, 93]. In [12], all equilibria of a wind integrated power system, parameterized by wind variables, are obtained via NPHC method which we apply in this work to identify the power flow solution boundaries.

The method requires the solution of power flow equations at a generic complex parameter point so as to obtain all the complex solutions, the number of which is upper bounded by the Classical Bézout Bound. Usually the Bézout Bound grows exponentially with the number of variables and so is the complexity of solving the start problem [12]. But once the start solution is solved, the solutions for the same power flow equations can be tracked via a predictor corrector method to real parameter values. In the second stage our method is really efficient as we have to track much lesser number of parameter points as compared to the Bézout Bound shown in section 5.3. However still our method guarantees to obtain all complex solutions and hence real solutions at every point on the parameter space. Hence one can detect the power flow solution space boundaries by noting the change in number of real solutions over the parameter space without any initial guess or a priori information about the solution space. Though the start solution is complex, but it is needed to be solved only once. Once the solution for the start problem is finalized the computational complexity is much reduced even for higher resolution of points over the parameter space. In a higher dimensional parameter space as observed in the multiple wind penetration scenario this method is particularly effective to identify all the solution space boundaries.

5.6 Examples

5.6.1 3-bus System

First we explore the the solution space boundary for a 3 bus power system as shown in figure 5.3a, which is a modification of an example in [35] with added loads. The active power input in bus 1 and 2 are the varying parameters and are defined as γ_1 and γ_2 respectively. Bus 3 is assumed to be the swing bus whose voltage equals $1\angle 0$. The unknown state variables of the power flow problem which constitute the vector x in (5.23) are the active and reactive power input in bus 3, the reactive powers and angles of bus 1 and 2. However as shown in section 5.3 we represent the angles in rectangular form to limit the order of the algebraic equations to 2. Thus we have the sine

and cosine of the angle of bus 1 and bus 2 as the unknown variables. The problem now evolves into computation of the unknown vector $x = \left[P_3 \ Q_3 \ Q_1 \ Q_2 \ \sin \delta_1 \ \cos \delta_1 \ \sin \delta_2 \ \cos \delta_2 \right]^T$ over a set of parameter values γ_1 and γ_2 by solving the nonlinear power flow equations. As mentioned earlier in section 5.3, we solve the system of equations $f(x, \lambda^*) = 0$ at a generic complex parameter point λ^* of γ_1 and γ_2 . The generic complex vector has two elements which are chosen from uniform distributions such as $\{a + ib : -1 \leq a, b \leq 1\}$ and are normalized to ensure they are inside unit circle. For the start problem $f(x, \lambda^*) = 0$, we followed the CBB and searched for $2^8 = 256$ paths to obtain all the isolated complex solutions that are theoretically possible. However the start problem in this case yielded only 6 solutions. Correspondingly in the next half of the algorithm, following *Cheater's homotopy* we only had to track 6 paths for each parameter point starting from the start solution which reduces computational task significantly. Once all the complex solutions have been obtained the real solutions are identified by doing numerical check. As seen in figure 5.3b the number of real solutions vary from 0 to 6 for the power flow problem. The boundaries can be identified by the change in the number of real solutions where the jacobian of power flow equilibrium becomes singular. In the work by Hiskens

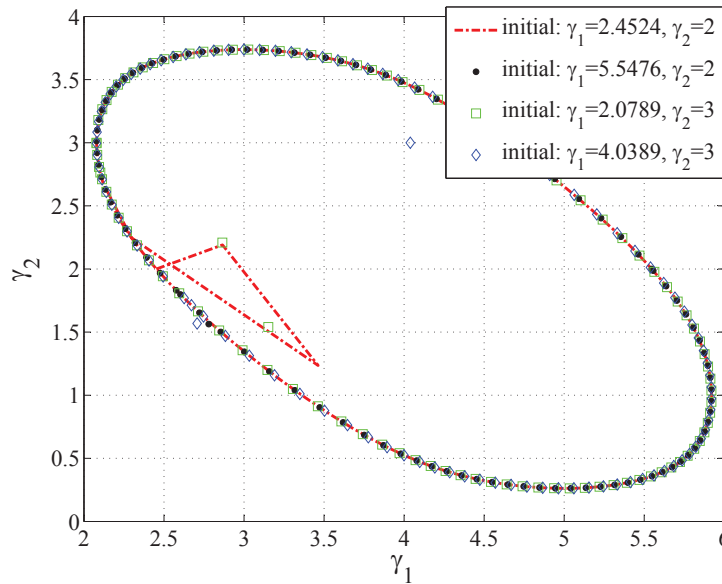


Figure 5.4: Power flow solution boundary tracking with various initial points

et al. [35], the power flow solution boundary is tracked by a gradient based predictor-corrector algorithm starting from an initial point x_0 . First, (5.23) is represented as,

$$\phi(z) = \begin{bmatrix} f(z) \\ g(z) \\ h(z) \end{bmatrix} \quad (5.25)$$

where $z = \begin{bmatrix} x & v & \lambda \end{bmatrix}'$. Starting from an initial z_0 which satisfies the condition $\phi(z_0) = 0$, the algorithm solves for z_i by computationally solving the following problem at each step i ,

$$\phi(z_i) = 0 \quad (5.26a)$$

$$(z_i - z_{i-1})' \nu = \epsilon \quad (5.26b)$$

where ν and ϵ are constants. A fixed value for ϵ is chosen which determines the accuracy of the

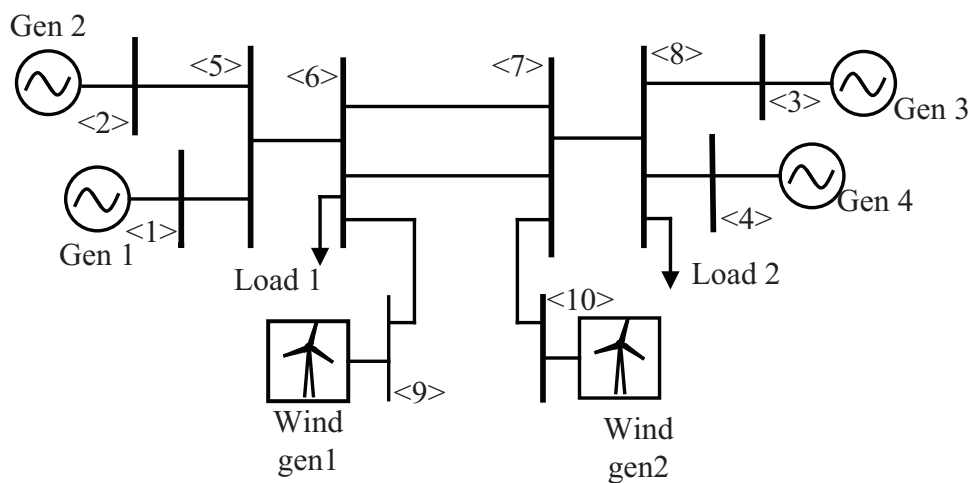


Figure 5.5: 10-bus power system with 2 WPP

numerical approximation while ν is a vector tangential to the solution boundary at z_{i-1} . Since this method tracks the solution boundary iteratively choice of the initial point is important. In

the first step we keep γ_2 fixed and find an initial point on the solution boundary. Essentially we solve (5.23) in a Newton-Raphson method with different initial points for γ_1 . When $\gamma_2 = 2$, we find initial points with $\gamma_1 = 2.4534$ and 5.5476 . When $\gamma_2 = 3$, the initial points have $\gamma_1 = 2.0789$ and 4.0389 . As seen in figure 5.3b, all of these points are located on the outer elliptical solution boundary. Correspondingly in the second step when we solve (5.26) in an iterative form starting from these points they only track the outer boundary as shown in figure 5.4. Thus with this method it is difficult to identify all the power flow solution boundaries unless one has a sound knowledge of the solution space for a given set of parameters. For a high dimensional parameter space these boundaries are even more complex and correspondingly its difficult to guarantee *all* solution boundaries which our alternate numerical homotopy based method can identify. Next we show the power flow solution boundary computation of a 10 bus solution with 2 wind injections.

5.6.2 10-bus system

We use a 10-bus, 4-synchronous machine power system as shown in figure 5.5, for the simulation where we investigate for the power flow solution boundary for varying wind power penetrations. Two wind power plants are connected at bus 9 and bus 10 whose penetration levels are represented as γ_{w9} and γ_{w10} respectively. The parameters of the simulation are given in Appendix A.3. We vary the active power output of each of the WPP between 0.1 and 0.7 p.u. on a 100 MVA base and correspondingly formulate our equilibrium analysis problem of solving (5.14)-(5.19) for different points on the parameter space of γ_{w9} and γ_{w10} . We solve the problem at a generic complex parameter point using the homotopy based algorithm of section 5.3, implemented in *Mathematica* and *Bertini* [6]. The problem has 25 unknown equations which requires 2^{25} paths to be tracked by continuation in the start problem to ensure all the isolated roots. It turns out that the start solution has got only 2^9 isolated roots which saves the computational effort of finding the roots for the actual parameter values in subsequent steps. figure 5.6 shows the power system solution boundary where the number of real solution changes. It can be observed that

the geometry of the solution boundary for the 10-bus case with varying wind penetration levels is strikingly different as compared to the 3-bus case. Also the number of isolated boundaries are more than that of the 3-bus case. All these observations suggest that identifying all these boundaries by an initial guess and local approximation is totally intractable. Correspondingly in a multiple wind injection scenario this analysis tool gives the operator a choice to choose an operating point which is robust and far away from the loadability boundary of the power system

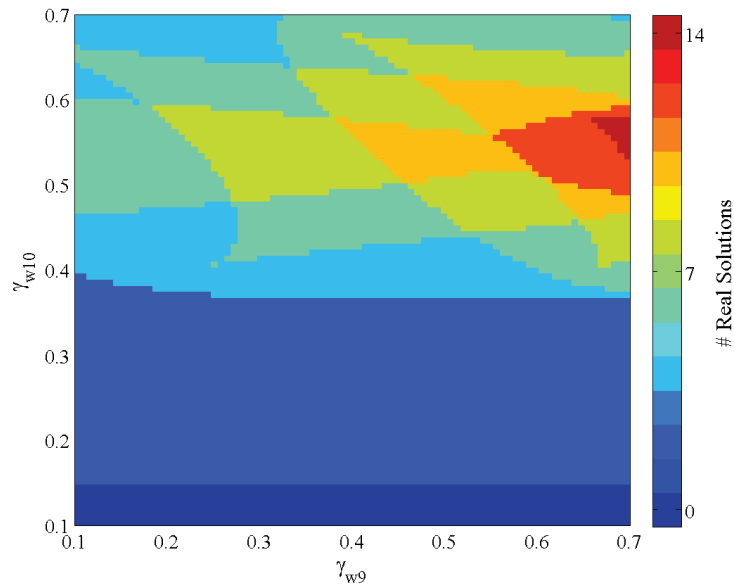


Figure 5.6: Number of real solutions of the power flow in the 10-bus power system

5.7 Conclusions

In this work we have shown that the parameters of the different dynamic elements of a complex power system may lead to multiple feasible equilibria depending on their values. In contrast to traditional load flow solution, we used a novel homotopy based continuation method to evaluate all the equilibria in an efficient manner. The simulation results show for certain combination of

parameter values of different elements, undesired or even unstable eigenvalues may occur. The knowledge of all feasible solutions of power flow are thus indispensable for dispatch and control in future power system operations and controller design. Further we have applied the algorithm for detecting *all* the power flow solution boundaries, also known as loadability boundaries of the power system. Identification of the boundaries enable the power system operator to choose the power system operating points which are robust and within transient voltage stability limit.

Chapter 6

Conclusions and Future Works

The capacity of wind energy installations is growing rapidly worldwide as an important source of renewable energy. As a consequence, in near future the wind generators which are interconnected with the grid asynchronously via DFIG will largely replace the conventional synchronous generators which currently constitute the bulk of the power supply. This shift in the mode of generation from synchronous to asynchronous form will have a major impact on various operational aspects of the power system. Thus in this dissertation, we have tried to develop novel analytical methods to assess these impacts of high wind penetration particularly on the equilibria and the inter-area oscillations of the power system. We have validated our analytical results with simulation on different standard IEEE models like the 2-area, 8-bus, 4-machine Kundur system, the 7-bus, 5-machine Brazilian system, the 5-area 68-bus 16-machine power system etc. We designed controllers on the wind farm and the associated energy storage to damp the inter-area oscillations ill-affected by the wind penetration. We also devised a novel parameter homotopy based method to find all equilibria of a wind integrated power system and applied that in identifying small-signal voltage stability limit of the power system.

In Chapter 2 of this work, we derived the spectral response of power flow in a wind integrated radial power system with a continuum model approximation. The spectral response as illustrated in theory and in simulation, shows that the spatial location of a wind farm has a major impact

on the inter-area oscillations. Correspondingly some wind farm sitting locations can have a worse impact on the damping and frequency of the inter-area oscillatory spectrum. To provide additional damping in Chapter 3, we proposed a coordinated control scheme to modulate the wind farm power output and power flow of the BES. We also looked at a distributed implementation of the controller in different turbines of the wind plant.

However due to limitations of the approximated continuum models we looked at more conventional models of the power system in Chapter 4. Here we investigated the time-scale separation of coherent power systems in presence of typically high wind penetration. We showed by theory and by adequate case studies as to how the slow time-scales associated with the power system dynamics depend on the level of wind penetration in a single generation area. The results indicate that time-scale separation not only depends on the level of wind injection but also heavily depends on the system topology and location of wind plant with respect to major loads and other synchronous generators. These results confirm our notion that the location of the wind farm is an important factor in the impact of the wind as derived in Chapter 2. We show via a case study that wind might cause inter-area oscillations to be slower, making the system unstable by primarily affecting the voltage on the buses.

In Chapter 5 we use a numerical homotopy based continuation method to identify *all* equilibria of a wind-integrated power system. Traditional continuation based methods depend on initial guess and local approximations of the power flow solutions. Particularly when multiple solutions exist for the power flow equations, these iterative methods can only ensure to find one solution. Instead our numerical homotopy algorithm is independent of initial guess or local approximation and efficiently solves for *all* real roots of the power flow equations. We have also showed a practical application of our approach in identifying power flow solution boundaries where jacobian of power flow solution is singular. All previously developed methods depend on initial guess and can never guarantee to find all solution boundaries, which are essential to maintain transient voltage stability. By our method, we can simply look at the change in the number of real power flow solutions over a parameter space and guarantee to identify the

power flow solution boundaries. The knowledge of power flow solution boundary is crucial for power system operators to choose robust operating point of the power system well within the the stability limit.

The work proposed in this manuscript leads to a number of future research plans for developing appropriate analytical tools for in-depth analysis of wind integrated model and to build control methods for ensuring power system stability and performance.

1. In Chapter 3 of this dissertation, we have designed co-dependent controllers on wind and battery energy system to damp inter-area oscillations in power systems. There are some recent works [4] which attempted to control Battery energy system simultaneously with exciter of a generator to maintain terminal voltage regulation and transient stabilization. This type of control design will be essential to connect large wind generator to the grid and can be done as an extension of the work done in Chapter 3.
2. A more comprehensive analysis should be conducted to identify the impact of high wind penetration on the eigenvectors of the linearized power system. In Chapter 4 of this dissertation we looked at the effect of wind penetration on the eigenvalues for different penetration levels. However the eigenvectors of the linearized system determine the residues of the inter and intra-area modes and thus critically influence the time response of the system. With different wind penetration levels, the way these eigenvectors change will be worth investigating. Another interesting topic will be to look at the impact of the factors like topology and the proximity of wind to major loads on the eigenvectors.
3. In Chapter 5 we applied the NPHC method to obtain power system solution boundaries for the wind-integrated power system which is actually the transient voltage stability limit. However we can additionally use the feature of finding all real solutions to identify power flow solution boundaries which maintains simultaneously both transient voltage stability and rotor angle stability. Also one can look to exploit the sparsity of interconnections in power systems to define more tighter bound of maximum number of complex solutions.

REFERENCES

- [1] World wind market blooming like never before: Wind capacity over 392 gigawatt. <http://www.wwindea.org/hyr2015/>. Accessed: 09-11-2015.
- [2] V. Ajjarapu and C. Christy. The continuation power flow: a tool for steady state voltage stability analysis. *IEEE Transactions on Power Systems*, 7(1):416--423, 1992.
- [3] J. Baillieul and C.I. Byrne. Geometric Critical Point Analysis of Lossless Power System Models. *IEEE Trans. Circuits Syst.*, 29(11), 1982.
- [4] Stefanos Barosy and Marija D Ilic. On transient stability and voltage regulation through mimo feedback linearizing control of generator and energy storage. In *American Control Conference (ACC), 2015*, pages 4320--4326. IEEE, 2015.
- [5] Daniel J Bates, Daniel A Brake, and Matthew E Niemerg. Paramotopy: Parameter homotopies in parallel, 2012. Available at www.paramotopy.com.
- [6] Daniel J Bates, Jonathan D Hauenstein, Andrew J Sommese, and Charles W Wampler. Bertini: Software for numerical algebraic geometry, 2006.
- [7] David N Bernshtein. The number of roots of a system of equations. *Functional Analysis and its Applications*, 9(3):183--185, 1975.
- [8] F. A. Bhuiyan and A. Yazdani. Reliability assessment of a wind-power system with integrated energy storage. *IET Renewable Power Generation*, 4(3):211--220, May 2010.
- [9] Eilyan Y Bitar, Ram Rajagopal, Pramod P Khargonekar, Kameshwar Poolla, and Pravin Varaiya. Optimal contracts for wind power producers in electricity markets. *IEEE Trans. on Power Sys.*, 27(3):1225--1235, 2012.
- [10] P. Bousseau, F. Fesquet, R. Belhomme, S. Nguefeu, and T.-C. Thai. Solutions for the grid integration of wind farms - A survey. *Wind Energy*, 9(1):13 -- 25, 2006.
- [11] S. Chandra, D.F. Gayme, and A. Chakrabortty. Coordinating wind farms and battery management systems for inter-area oscillation damping: A frequency-domain approach. *IEEE Trans. on Power Sys.*, 29(3):1454--1462, 2014.
- [12] S. Chandra, D. Mehta, and A. Chakrabortty. Exploring the impact of wind penetration on power system equilibrium using a numerical continuation approach. In *American Control Conference (ACC), 2015*, Chicago, Il, July.
- [13] S. Chandra, M.D. Weiss, A. Chakrabortty, and D.F. Gayme. Impact analysis of wind power injection on time-scale separation of power system oscillations. In *Proc. of the Power and Energy Soc. Gen. Meeting*, 2014.
- [14] Souvik Chandra, Dennice F Gayme, and Aranya Chakrabortty. Using battery management systems to augment inter-area oscillation control in wind-integrated power systems. In *American Control Conference (ACC), 2013*, pages 5809--5814. IEEE, 2013.

- [15] T. Chen and D. Mehta. Parallel degree computation for solution space of binomial systems with an application to the master space of $\mathcal{N} = 1$ gauge theories. *arxiv preprint arxiv.org/abs/1501.02237*, 2015.
- [16] Zhong Chen, Ming Ding, and Jianhui Su. Modeling and control for large capacity battery energy storage system. In *Electric Utility Deregulation and Restructuring and Power Technologies (DRPT), 2011 4th International Conference on*, pages 1429--1436. IEEE, 2011.
- [17] J. Chow and P. Kokotovic. Time scale modeling of sparse dynamic networks. *IEEE Trans. on Automatic Control*, 30(8), 1985.
- [18] J. H. Chow. *Power System Coherency and Model Reduction*, chapter Slow Coherency and Aggregation, pages 39--72. Springer New York, Jan. 2013.
- [19] C. M. Colson and M. H. Nehrir. Load-following for wind turbines with permanent magnet synchronous generators. In *North American Power Symposium*, Arlington, TX, 2010.
- [20] R. L. Cresap and J. F. Hauer. Emergence of a new swing mode in the western power loop. *IEEE Trans. on Power Apparatus and Sys.*, PAS-100(4):2037--2045, 1981.
- [21] R. Datta and V. T. Ranganathan. Variable-speed wind power generation using doubly fed wound rotor induction machine-a comparison with alternative schemes. *IEEE Trans. on Energy Conversion*,, 17(3):414--421, 2002.
- [22] Rajib Datta and VT Ranganathan. Decoupled control of active and reactive power for a grid-connected doubly-fed wound rotor induction machine without position sensors. In *Industry Applications Conference, 1999. Thirty-Fourth IAS Annual Meeting. Conference Record of the 1999 IEEE*, volume 4, pages 2623--2630. IEEE, 1999.
- [23] Furkan Dincer. The analysis on photovoltaic electricity generation status, potential and policies of the leading countries in solar energy. *Renewable and Sustainable Energy Reviews*, 15(1):713--720, 2011.
- [24] Baofu Gao, GK Morison, and Prabhashankar Kundur. Voltage stability evaluation using modal analysis. *Power Systems, IEEE Transactions on*, 7(4):1529--1542, 1992.
- [25] Durga Gautam, Lalit Goel, Raja Ayyanar, Vijay Vittal, and Terry Harbour. Control strategy to mitigate the impact of reduced inertia due to doubly fed induction generators on large power systems. *Power Systems, IEEE Transactions on*, 26(1):214--224, 2011.
- [26] Durga Gautam, Vijay Vittal, and Terry Harbour. Impact of increased penetration of dfig-based wind turbine generators on transient and small signal stability of power systems. *Power Systems, IEEE Transactions on*, 24(3):1426--1434, 2009.
- [27] D. F. Gayme and A. Chakraborty. Impact of wind farm placement on inter-area oscillations in large power systems. In *Proc. of the American Control Conf.*, Montreal, PQ, 2012.

- [28] D. F. Gayme and A. Chakraborty. Shaping power system inter-area oscillations through control loops of grid integrated wind farms. In *Proc. of the IEEE Conf. on Decision and Control*, 2012.
- [29] A. J. Germond and R. Podmore. Dynamic aggregation of generating unit models. *IEEE Trans. on Power Apparatus and Sys.*, (4):1060--1069, 1978.
- [30] B. Greene, D. Kagan, A. Masoumi, D. Mehta, E. J. Weinberg, and X. Xiao. Tumbling through a landscape: Evidence of instabilities in high-dimensional moduli spaces. *Phys.Rev.*, D88(2):026005, 2013.
- [31] S.X. Guo and F.M.A. Salam. Determining the Solutions of the Load Flow of Power Systems: Theoretical Results and Computer Implementation. In *IEEE 29th Ann. Conf. Decis. Contr. (CDC)*, pages 1561--1566, Dec. 1990.
- [32] J. D. Hauenstein, Y.-H. He, and D. Mehta. Numerical elimination and moduli space of vacua. *Journal of High Energy Physics*, 1309:083, 2013.
- [33] J. D. Hauenstein, Rijun Huang, Dhagash Mehta, and Yang Zhang. Global Structure of Curves from Generalized Unitarity Cut of Three-loop Diagrams. *arxiv preprint arxiv.org/abs/1408.3355*, 2014.
- [34] Y.-H. He, D. Mehta, M. Niemerg, M. Rummel, and A. Valeanu. Exploring the Potential Energy Landscape Over a Large Parameter-Space. *Journal of High Energy Physics*, 1307:050, 2013.
- [35] Ian Hiskens, Robert J Davy, et al. Exploring the power flow solution space boundary. *Power Systems, IEEE Transactions on*, 16(3):389--395, 2001.
- [36] C. Huges, D. Mehta, and Jon-Ivar Skullerud. Enumerating Gribov copies on the lattice. *Annals Phys.*, 331:188--215, 2013.
- [37] A Jepsen and A Spence. Folds in solutions of two parameter systems and their calculation. part i. *SIAM journal on numerical analysis*, 22(2):347--368, 1985.
- [38] I. Kamwa, A. Héliche, and M. de Montigny. Assessment of AGC and load-following definitions for wind integration studies in Québec. In *Proc. of the 8th Int'l Workshop on Large-Scale Integration of Wind Power into Power Sys.*, Oct. 2009. paper no. 129.
- [39] Daniel Karlsson and David J Hill. Modelling and identification of nonlinear dynamic loads in power systems. *IEEE Trans. on Power Syst.*, 9(1):157--166, 1994.
- [40] Michael E Karystianos, Nicholas G Maratos, and Costas D Vournas. Maximizing power-system loadability in the presence of multiple binding complementarity constraints. *Circuits and Systems I: Regular Papers, IEEE Transactions on*, 54(8):1775--1787, 2007.
- [41] M. Kastner and D. Mehta. Phase Transitions Detached from Stationary Points of the Energy Landscape. *Phys.Rev.Lett.*, 107:160602, 2011.

- [42] Askold G Khovanskii. Newton polyhedra and the genus of complete intersections. *Functional Analysis and its applications*, 12(1):38--46, 1978.
- [43] Prabha Kundur. *Power system stability and control*, volume 7. McGraw-hill New York, 1994.
- [44] Prabha Kundur, John Paserba, Venkat Ajjarapu, Göran Andersson, Anjan Bose, Claudio Canizares, Nikos Hatziargyriou, David Hill, Alex Stankovic, Carson Taylor, et al. Definition and classification of power system stability iee/cigre joint task force on stability terms and definitions. *Power Systems, IEEE Transactions on*, 19(3):1387--1401, 2004.
- [45] Anatoly Georievich Kushnirenko. A newton polyhedron and the number of solutions of a system of k equations in k unknowns. *Usp. Math. Nauk*, 30:266--267, 1975.
- [46] Tien Yien Li. Solving polynomial systems by the homotopy continuation method. *Handbook of numerical analysis*, 11:209--304, 2003.
- [47] TY Li, Tim Sauer, and JA Yorke. The cheater's homotopy: an efficient procedure for solving systems of polynomial equations. *SIAM Journal on Numerical Analysis*, 26(5):1241--1251, 1989.
- [48] Chih-Wen Liu, Chen-Sung Chang, Joe-Air Jiang, and Guey-Haw Yeh. Toward a cpflow-based algorithm to compute all the type-1 load-flow solutions in electric power systems. *Circuits and Systems I: Regular Papers, IEEE Transactions on*, 52(3):625--630, 2005.
- [49] Yilu Liu. A us-wide power systems frequency monitoring network. In *Power Systems Conference and Exposition, 2006. PSCE'06. 2006 IEEE PES*, pages 159--166. IEEE, 2006.
- [50] C.-F. Lu, C.-C. Liu, and C.-J. Wu. Dynamic modelling of battery energy storage system and application to power system stability. *IEE Proc. Generat. Transm. Distrib.*, 142(4):429--435, Jul. 1995.
- [51] M. Milligan *et al.* Operating reserves and wind power integration: An international comparison. In *Proc. of the 9th Int'l Workshop on Large-Scale Integration of Wind Power into Power Sys.*, Québec, Canada, 2010.
- [52] Weimin Ma and James S Thorp. An efficient algorithm to locate all the load flow solutions. *Power Systems, IEEE Transactions on*, 8(3):1077--1083, 1993.
- [53] M. Maniatis and D. Mehta. Minimizing Higgs Potentials via Numerical Polynomial Homotopy Continuation. *Eur.Phys.J.Plus*, 127:91, 2012.
- [54] M. Maniatis and D. Mehta. On exact minimization of Higgs potentials. *Eur.Phys.J.Plus*, 129:109, 2014.
- [55] D. Martinez-Pedrerera, D. Mehta, M. Rummel, and A. Westphal. Finding all flux vacua in an explicit example. *Journal of High Energy Physics*, 1306:110, 2013.

- [56] D. Mehta. Lattice vs. Continuum: Landau Gauge Fixing and 't Hooft-Polyakov Monopoles. *Ph.D. Thesis, The Uni. of Adelaide, Australasian Digital Theses Program*, 2009.
- [57] D. Mehta. Finding All the Stationary Points of a Potential Energy Landscape via Numerical Polynomial Homotopy Continuation Method. *Phys.Rev.*, E84:025702, 2011.
- [58] D. Mehta. Numerical Polynomial Homotopy Continuation Method and String Vacua. *Adv.High Energy Phys.*, 2011:263937, 2011.
- [59] D. Mehta, N. S. Daleo, J. D Hauenstein, and C. Seaton. Gauge-fixing on the Lattice via Orbifolding. *Phys.Rev.*, D90(5):054504, 2014.
- [60] D. Mehta, J. D. Hauenstein, and M. Kastner. Energy-landscape analysis of the two-dimensional nearest-neighbor ϕ^4 model. *Phys. Rev. E*, 85:061103, Jun 2012.
- [61] D. Mehta, J. D. Hauenstein, Matthew Niemerg, Nicholas J. Simm, and Daniel A. Stariolo. Energy Landscape of the Finite-Size Mean-field 2-Spin Spherical Model and Topology Trivialization. 2014.
- [62] D. Mehta, Y.-H. He, and J. D. Hauenstein. Numerical Algebraic Geometry: A New Perspective on String and Gauge Theories. *Journal of High Energy Physics*, 1207:018, 2012.
- [63] D. Mehta, C. Huges, M. Schröck, and D. J. Wales. Potential Energy Landscapes for the 2D XY Model: Minima, Transition States and Pathways. *J. Chem. Phys.*, 139:194503, 2013.
- [64] D. Mehta, H. Nguyen, and K. Turitsyn. Numerical Polynomial Homotopy Continuation Method to Locate All The Power Flow Solutions. *arxiv preprint arxiv.org/abs/1408.2732*, 2014.
- [65] D. Mehta and M. Schröck. Enumerating copies in the first gribov region on the lattice in up to four dimensions. *arxiv preprint arxiv.org/abs/1403.0555*, 2014.
- [66] D. Mehta, Daniel A. Stariolo, and Michael Kastner. Energy landscape of the finite-size spherical three-spin glass model. *Phys.Rev.*, E87(5):052143, 2013.
- [67] D. Mehta, Andre Sternbeck, Lorenz von Smekal, and Anthony G Williams. Lattice Landau Gauge and Algebraic Geometry. *PoS, QCD-TNT09:025*, 2009.
- [68] Dhagash Mehta, Noah S Daleo, Florian Dörfler, and Jonathan D Hauenstein. Algebraic geometrization of the kuramoto model: Equilibria and stability analysis. *Chaos: An Interdisciplinary Journal of Nonlinear Science*, 25(5):053103, 2015.
- [69] Sean Meyn, Matias Negrete-Pincetic, Gui Wang, Anupama Kowli, and Ehsan Shafieepoorfard. The value of volatile resources in electricity markets. In *Decision and Control (CDC), 2010 49th IEEE Conference on*, pages 1029--1036. IEEE, 2010.
- [70] Z. Miao, L. Fan, and D. Osborn. Control of DFIG based wind generation to improve inter-area oscillation damping. *IEEE Trans. on Energy Conv.*, 24(2):415--422, June 2009.

- [71] D.K. Molzahn, C. Jozs, I.A. Hiskens, and P. Panciatici. Solution of Optimal Power Flow Problems using Moment Relaxations Augmented with Objective Function Penalization. *IEEE 54th Ann. Conf. Decis. Contr. (CDC)*, Dec. 2015.
- [72] Mehta D. Molzahn, D. and M. Niemerg. Toward Topologically Based Upper Bounds on the Number of Power Flow Solutions: Numerical Experiments.
- [73] Alexander P. Morgan and Andrew J. Sommese. Computing all solutions to polynomial systems using homotopy continuation. *Applied Mathematics and Computation*, 24(2):115--138, 1987.
- [74] Alexander P Morgan and Andrew J Sommese. Coefficient-parameter polynomial continuation. *Applied Mathematics and Computation*, 29(2):123--160, 1989.
- [75] National Renewable Energy Laboratory. 20% wind energy by 2030: Increasing wind energy's contribution to U.S. electricity supply. Technical Report DOE/GO-102008-2567, US Dept. of Energy, July 2008.
- [76] Rachele Nerattini, M. Kastner, Dhagash Mehta, and Lapo Casetti. Exploring the energy landscape of XY models. *Phys.Rev.*, E87(3):032140, 2013.
- [77] M.V.A. Nunes, J.A. Peças Lopes, H.H. Zürn, U.H. Bezerra, and R.G. Almeida. Influence of the variable-speed wind generators in transient stability margin of the conventional generators integrated in electrical grids. *IEEE Trans. on Energy Conversion*, 19(4):692--701, 2004.
- [78] U.S. Department of Energy. Strengthening americas energy security with offshore wind. Technical report, April 2012.
- [79] L. Y. Pao and K. E. Johnson. Control of wind turbines. *IEEE Control Sys. Magazine*, 31(2):44--62, Apr. 2011.
- [80] Magnus Perninge and Lennart Söder. On the validity of local approximations of the power system loadability surface. *Power Systems, IEEE Transactions on*, 26(4):2143--2153, 2011.
- [81] E.G. Potamianakis and C.D. Vournas. Short-term voltage instability: Effects on synchronous and induction machines. *IEEE Transactions on Power Systems*, 21(2):791--798, 2006.
- [82] AW Price, AW Hargrave, BJ Hurysz, JH Chow, and PM Hirsch. Large-scale system testing of a power system dynamic equivalencing program. *IEEE Trans. on Power Sys.*, 13(3):768--774, 1998.
- [83] Héctor A Pulgar-Painemal and Peter W Sauer. Power system modal analysis considering doubly-fed induction generators. In *Bulk Power System Dynamics and Control (iREP)-VIII (iREP), 2010 iREP Symposium*, pages 1--7. IEEE, 2010.
- [84] G. N. Ramaswamy, C. Evrard, George C. Verghese, O. Fillâtre, and B. C. Lesieutre. Extensions, simplifications, and tests of synchronic modal equivalencing (SME). *IEEE Trans. on Power Sys.*, 12(2):896--905, 1997.

- [85] Werner C Rheinboldt. Computation of critical boundaries on equilibrium manifolds. *SIAM Journal on Numerical Analysis*, 19(3):653--669, 1982.
- [86] FMA Salam, L Ni, S Guo, and X Sun. Parallel processing for the load flow of power systems: the approach and applications. In *Decision and Control, 1989., Proceedings of the 28th IEEE Conference on*, pages 2173--2178. IEEE, 1989.
- [87] B Sanderse, van der SP Pijl, and B Koren. Review of computational fluid dynamics for wind turbine wake aerodynamics. *Wind Energy*, 14(7):799--819, 2011.
- [88] Abhinav Kumar Singh and Bikash C. Pal. *IEEE PES Task Force on Benchmark Systems for Stability Controls Report on the 68-Bus, 16-Machine, 5-Area System*. 2013.
- [89] Mohit Singh and Surya Santoso. *Dynamic models for wind turbines and wind power plants*. National Renewable Energy Laboratory, 2011.
- [90] R. Sioshansi and W. Short. Evaluating the impacts of real-time pricing on the usage of wind generation. *IEEE Trans. on Power Sys.*, 24(2):516--524, May 2009.
- [91] J. G. Slootweg. The impact of large scale wind power generation on power system oscillations. *Electric Power Sys. Research*, 67(1):9--20, 2003.
- [92] C. Sloth, T. Esbensen, and J. Stoustrup. Active and passive fault-tolerant LPV control of wind turbines. In *Proc. of the American Control Conf.*, Baltimore, MD, 2010.
- [93] Andrew John Sommese and Charles Weldon Wampler. *The Numerical solution of systems of polynomials arising in engineering and science*, volume 99. World Scientific, 2005.
- [94] Aleksandar M Stankovic and Andrija T Saric. Transient power system analysis with measurement-based gray box and hybrid dynamic equivalents. *IEEE Trans. on Power Sys.*, 19(1):455--462, 2004.
- [95] G. Tsourakis, B. M. Nomikos, and C. D. Vournas. Contribution of doubly fed wind generators to oscillation damping. *IEEE Trans. on Energy Conversion*, 24(3):783--791, 2009.
- [96] C.E. Ugalde-Loo, J.B. Ekanayake, and N. Jenkins. State-space modeling of wind turbine generators for power system studies. *IEEE Trans. on Industry Applications*, 49(1):223--232, 2013.
- [97] Nayeem Rahmat Ullah and Torbjrn Thiringer. Variable speed wind turbines for power system stability enhancement. *IEEE Trans. on Energy Conversion*, 22(1):52--60, 2007.
- [98] Vijay Vittal. The impact of renewable resources on the performance and reliability of the electricity grid. *The Bridge, National Academy of Engineering*, 40(1):5--12, 2010.
- [99] JOHN Zaborszky, Keh Wen Whang, GARNG M Huang, Luo Jen Chiang, and Shin Yeu Lin. A clustered dynamic model for a class of linear autonomous systems unusing simple enumerative sorting. *IEEE Trans. on Circuits and Sys.*, 29(11):747--758, 1982.

APPENDIX

Appendix A

Simulation Parameters

A.1 Model Parameters for Two-area Kundur System

Synchronous machines are modeled by classical 2nd order models with the following parameters on a 100-MVA base:

Generator 1: $m_1 = 3.28$ p.u., $x'_{d1} = 0.06$ p.u., $P_{e1} = 3.78$ p.u.

Generator 2: $m_2 = 5.32$ p.u., $x'_{d2} = 0.03$ p.u., $P_{e2} = 1.88$ p.u.

Generator 3: $m_3 = 5.70$ p.u., $x'_{d3} = 0.02$ p.u., $P_{e3} = 1.05$ p.u.

Generator 4: $m_4 = 4.75$ p.u., $x'_{d4} = 0.08$ p.u., $P_{e4} = 4.21$ p.u.

Line parameters on 100-MVA base: $Z_{15} = j4e-3$, $Z_{25} = j4e-3$, $Z_{38} = j4e-3$, $Z_{48} = j4e-3$, $Z_{56} = j6e-3$, $Z_{67} = j0.13$, $Z_{78} = j6e-3$.

Load parameters: Two loads, 500 MW and 40 MVAR each.

A.2 Wind Plant Parameters

100 wind generators, each consisting of a DFIG, 1.0 MW, 575 V, 60 Hz, are used. Every DFIG has the following parameters: $J_r = 3.08 \times 10^6$ kgm², $J_g = 75$ kgm², $B_r = 3.37 \times 10^3$ Nm/(rads/s), $B_g = 3.034$ Nm/(rads/s), $B_{dt} = 108$ kNm/(rads/s), $K_{dt} = 6.75 \times 10^8$ Nm/rad, $N_g = 66$, $A_s = 2463$ m², $\rho = 1.225$ kg/m³, $v_{r0} = 9$ m/s, $w_{r0} = 226$ rad/s, $R_s = 0.0111$ p.u.,

$R_r = 0.0108$ p.u., $L_{ls} = 0.1487$ p.u., $L_{lr} = 0.1366$ p.u., $L_m = 4.6978$ p.u. and $p = 4$.

A.3 Model Parameters for 10-bus 2-wind Generator Power System

Synchronous machines power ratings in p.u. 100-MVA base: Generator 1: 35.91, Generator 2: 17.85, Generator 3: 10, Generator 4: 40.

Line parameters in p.u. on 100-MVA base: $Z_{15} = j4e - 3$, $Z_{25} = j4e - 3$, $Z_{38} = j4e - 3$, $Z_{48} = j4e - 3$, $Z_{56} = j6e - 3$, $Z_{67} = j0.13$, $Z_{78} = j6e - 3$.

Load parameters in p.u. on 100-MVA base: load at bus 6, $42 + j13$, load at bus 8, $98 + j34$.